



## 저작자표시-비영리-변경금지 2.0 대한민국

이용자는 아래의 조건을 따르는 경우에 한하여 자유롭게

- 이 저작물을 복제, 배포, 전송, 전시, 공연 및 방송할 수 있습니다.

다음과 같은 조건을 따라야 합니다:



저작자표시. 귀하는 원저작자를 표시하여야 합니다.



비영리. 귀하는 이 저작물을 영리 목적으로 이용할 수 없습니다.



변경금지. 귀하는 이 저작물을 개작, 변형 또는 가공할 수 없습니다.

- 귀하는, 이 저작물의 재이용이나 배포의 경우, 이 저작물에 적용된 이용허락조건을 명확하게 나타내어야 합니다.
- 저작권자로부터 별도의 허가를 받으면 이러한 조건들은 적용되지 않습니다.

저작권법에 따른 이용자의 권리는 위의 내용에 의하여 영향을 받지 않습니다.

이것은 [이용허락규약\(Legal Code\)](#)을 이해하기 쉽게 요약한 것입니다.

[Disclaimer](#)

공학박사 학위논문

**High-Performance Solar and Fuel Cells  
by Design and Fabrication of  
Multilevel Multiscale Structures**

**고효율 태양전지 및 연료전지 시스템 구현을  
위한 멀티스케일 다층 구조물 설계 및 제작**

2018 년 2 월

서울대학교 대학원

기계항공공학부

장 세 근

# High-performance Solar and Fuel Cells by Design and Fabrication of Multilevel Multiscale Structures

고효율 태양전지 및 연료전지 시스템 구현을 위한  
멀티스케일 다층 구조물 설계 및 제작

지도교수 최 만 수

이 논문을 공학박사 학위논문으로 제출함

2017 년 12 월

서울대학교 대학원

기계항공공학부

장 세 근

장세근의 공학박사 학위논문을 인준함

2017 년 12 월

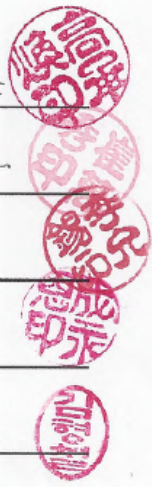
위 원 장 : 고 승 훈

부위원장 : 최 만 수

위 원 : 이 윤 석

위 원 : 서 영 은

위 원 : 김 형 치



# **High-Performance Solar and Fuel Cells by Design and Fabrication of Multilevel Multiscale Structures**

Segeun Jang

Department of Mechanical and Aerospace Engineering

The Graduate School

Seoul National University

## **Abstract**

In this thesis, we describe multiscale and multilevel structures with hierarchical patterns via controlled oxygen-inhibition effect of UV-curable materials and creeping behavior of viscoelastic polymer. With the multiscale multilevel structures, we could achieved superpositioned optical properties in mesoscopic dye-sensitized solar cells (DSSCs) and improve device performance of polymer electrolyte membrane fuel cells (PEMFCs) and direct methanol fuel cells (DMFCs).

First, we demonstrate a novel strategy for efficient photon harvesting based on the multilevel multiscale structures (integrated in z-axis direction) prepared by using multiplex lithography for constructing LEGO®-like architectures. In multiplex lithography, stacking of polyurethane acrylate (PUA) membrane with nano- or micro-apertures and additional nano-patterning was enabled by oxygen inhibition effect during photopolymerization of PUA. Based on the different curing degree of PUA membrane between bottom and top surface, partially cured bottom surface of the membrane was used for adhesion layer while relatively less cured top surface was employed for achieving additional nano patterning. Then,

multilevel multiscale PDMS molds were replicated from the multi-staked membrane and its architecture was imprinted on mesoporous  $\text{TiO}_2$  film by soft molding technique. By various spectral analyses and simulations, advanced light harvesting properties by superposition of optical responses from constituent nano- and micro-patterns were verified. We confirmed the effectiveness of our strategy by applications in dye-sensitized solar cells as a model system, wherein over 17.5% increase in efficiency (by multilevel 400 nm line / 20  $\mu\text{m}$  dot structures) was observed. Also, external quantum efficiencies clearly exhibited that the improved light harvesting was originated from the combined effects of diffraction grating and random scattering induced by both nano- and micro-architectures, respectively.

Next, we suggest a facile and simple multiscale patterning method called creep-assisted sequential imprinting and its application to PEMFC. Based on the creep behavior of a viscoelastic polymer (e.g. Nafion<sup>®</sup>), we firstly carried out nano-patterning by utilizing thermal imprint lithography above the glass transition temperature ( $T_g$ ) of the polymer film, and then followed by creep-assisted imprinting with micro-patterns based on the mechanical deformation of the polymer film under the relatively long-term exposure to mechanical stress at temperatures below the  $T_g$  of the polymer. The fabricated multiscale arrays exhibited excellent pattern uniformity over large areas (> 3.5 cm x 3.5 cm) and nano-patterns well remained after the second stamping procedure thanks to the creep behavior of Nafion<sup>®</sup>. Even on the side surface of micro-sized hole-patterns, furthermore, the nano-hole patterns clearly remained. To demonstrate the usage of multiscale architectures, the multiscale Nafion<sup>®</sup> membranes were incorporated into polymer electrolyte membrane fuel cell and this device showed over 10 % higher performance than conventional one. The enhancement was attributed to mainly two factors; 1. The decrease of mass transport resistance due to unique cone-shape morphology by creep-recovery effects, which generate

the Laplace pressure difference between upper-side and lower-side of droplet and this enables removal of droplet from the catalyst layer easily, 2. The increase of interfacial surface area between Nafion<sup>®</sup> membrane and electrocatalyst layer by using multiscale patterned membrane with large surface roughness, which brought increase of electrochemical surface area and higher Pt utilization.

Finally, for achieving high performance DMFC, we present a novel approach to engineer an interface between electrolyte membrane and catalyst layer. In DMFCs, the performance loss mainly resulted from two factors; 1. Slow kinetics of methanol oxidation at the anode, 2. Formation of a mixed potential at the cathode due to methanol crossover through an electrolyte membrane. To resolve both problems, we introduce a multiscale patterned membrane and a guided metal cracked layer between an anode catalyst layer and the membrane by the creep-assisted sequential imprinting and simple stretching technique. The membrane-electrode-assembly with a multiscale patterned membrane showed improved performance owing to enhanced mass transport by the thinned electrode, effective utilization of the active sites, and increased Pt utilization. Further, the electrochemically inactive thin gold layer acted as a physical barrier for methanol crossover and the guided cracks provided multiple proton pathways. From these synergetic effects, our interface engineering utility resulted in an enhancement of the device performance by 42.3% compared with that of the reference.

**Keywords: Multiscale patterning; Light harvesting; Creep behavior; Crack; Methanol crossover; Fuel cells**

**Student Number: 2013-22499**

# Contents

<b>Abstract .....</b>	<b>i</b>
<b>List of tables .....</b>	<b>vi</b>
<b>List of figures .....</b>	<b>vii</b>
<b>Nomenclature .....</b>	<b>xiv</b>
<b>Chapter 1. Introduction .....</b>	<b>1</b>
<b>Chapter 2. Oxygen-assisted multiplex lithography and its application to solar cells</b>	
2-1. Introduction .....	10
2-2. Experimental .....	14
2-3. Results and Discussion .....	18
2-3-1. Fabrication of polymeric molds with multiscale multilevel structures by controlling oxygen-inhibition effect .....	18
2-3-2. Multiscale multilevel designed mesoporous TiO <sub>2</sub> film .....	23
2-3-3. Super-positioned optical property of multiscale multilevel TiO <sub>2</sub> electrodes.....	28
2-3-4. Enhanced performance of multiscale architected dye-sensitized solar cell .....	33
2-4. Summary .....	43
<b>Chapter 3. Creep-assisted sequential imprinting method and its application to polymer electrolyte fuel cells</b>	
3-1. Introduction .....	45

3-2. Experimental .....	48
3-3. Results and Discussion .....	51
3-3-1. Creep-assisted sequential imprinting method for constructing multiscale multilevel structures .....	51
3-3-2. Enhanced performance of polymer electrolyte fuel cell with Multiscale multilevel designed membrane .....	60
3-4. Summary .....	70
 <b>Chapter 4. Interface engineering for high-performance direct methanol fuel Cells</b>	
4-1. Introduction .....	71
4-2. Experimental .....	74
4-3. Results and Discussion .....	80
4-3-1. Fabrication of multiscale patterned membranes .....	80
4-3-2. Enhanced cell performance of direct methanol fuel cells with multiscale patterned membranes .....	85
4-3-3. Further enhanced cell performance with guided metal cracked barriers .....	96
4-4. Summary .....	108
<b>References.....</b>	<b>109</b>
<b>국문 초록 .....</b>	<b>122</b>



# List of tables

- Table 2-1.** Loaded dye amounts on flat and patterned mp-TiO<sub>2</sub> photoelectrodes
- Table 2-2.** Detailed *J-V* characteristics of the DSSCs employing flat or patterned mp-TiO<sub>2</sub> photoelectrodes.
- Table 2-3.** *J-V* characteristics of the DSSCs employing 800 nm dot, 800 nm line, 800 nm dot / 20  $\mu$ m dot, or 800 nm line / 20  $\mu$ m dot patterned mp-TiO<sub>2</sub> photoelectrodes.
- Table 4-1.** Open circuit voltage, current density at 0.4 V, and maximum power density of prepared MEAs at two different methanol concentrations (1.5 M and 3.0 M)

# List of Figures

- Figure 1-1.** Brief introduction of the effects of multiscale structures which consists of nano- and micro- structures and its applications for improved optical properties of solar cells and high performance fuel cells
- Figure 2-1** Schematic illustration describing the procedure for preparation of multilevel multiscale PDMS molds by multiplex lithography and replication.
- Figure 2-2.** SEM images of multilevel multiscale PDMS molds. (a,b) 400 nm dot / 20  $\mu$ m dot patterned PDMS at (a) low and (b) high magnifications. (c,d) 400 nm line / 20  $\mu$ m dot patterned PDMS at (c) low and (d) high magnifications.
- Figure 2-3.** SEM images of (a,b) 400 nm dot, (c,d) 400 nm line, (e,f) 20  $\mu$ m dot patterned PDMS molds. The images were obtained by using either (a,c,e) secondary electron (SE2) detector or (b,d,f) in-lens detector.
- Figure 2-4.** Schematic illustration describing the methods for preparation of patterned mp-TiO<sub>2</sub> film by soft molding technique.
- Figure 2-5.** Top-view and cross-sectional SEM images of (a) flat, (b) 400 nm dot, (c) 400 nm line, (d) 20  $\mu$ m dot, (e) 400 nm dot / 20  $\mu$ m dot, and (f) 400 nm line / 20  $\mu$ m dot patterned mp-TiO<sub>2</sub>.

**Figure 2-6.** (a) Digital photographs of flat (noted as Reference) and patterned (detailed architectures noted at each image) mp-TiO<sub>2</sub>. (b) Reflectance spectra of flat and patterned mp-TiO<sub>2</sub>.

**Figure 2-7.** Calculated light reflection enhancement of patterned mp-TiO<sub>2</sub> compared to flat mp-TiO<sub>2</sub> from FDTD simulation.

**Figure 2-8.** (a) Digital photographs of flat and patterned mp-TiO<sub>2</sub> with dye-sensitization. (b) Absorbance spectra of flat and patterned mp-TiO<sub>2</sub> with dye-sensitization.

**Figure 2-9.** (a,b) *J-V* characteristics and (c,d) IPCE spectra of DSSCs employing mp-TiO<sub>2</sub> with (a,c) flat, 400 nm dot, 20  $\mu$ m dot, and 400 nm dot / 20  $\mu$ m dot patterns and (b,d) flat, 400 nm line, 20  $\mu$ m dot, and 400 nm line / 20  $\mu$ m dot patterned structures.

**Figure 2-10.** Top-view SEM images of (a) 800 nm dot, (b) 800 nm line, (c) 800 nm dot / 20  $\mu$ m dot, and (d) 800 nm line / 20  $\mu$ m dot patterned mp-TiO<sub>2</sub> films. The insets show enlarged images taken at higher magnifications.

**Figure 2-11.** *J-V* characteristics of DSSCs employing (a) 800 nm dot and 800 nm dot / 20  $\mu$ m dot patterned photoelectrodes and (b) 800 nm line and 800 nm line / 20  $\mu$ m dot patterned mp-TiO<sub>2</sub> films. Results of flat (noted as Reference) and 20  $\mu$ m dot patterned samples are displayed for comparisons.

**Figure 3-1.** Schematic illustration for fabrication process of multiscale Nafion membrane with sequential imprinting. (a) Imprinting nano-patterns on bare Nafion membrane under the above glass temperature condition ( $T_g$ ). (b) Sequential-imprinting micro-patterns on nano-patterned Nafion membrane under the below glass temperature condition

( $T_g$ ). (c) Replicating the multiscale-patterns with PUA from the multiscale Nafion membrane. (d-f) The corresponding digital camera images for nano-patterned Nafion membrane (d), multiscale Nafion membrane (e), and replicated multiscale PUA mold (f).

**Figure 3-2.** (a) The SEM image for nano-patterned Nafion membrane. (b-d) The SEM images for the obtained structures after sequential-imprinting with the stamping temperature variation of second imprinting process. (b)  $\sim 80\text{ }^{\circ}\text{C}$ , (c)  $\sim 100\text{ }^{\circ}\text{C}$ , and (d)  $\sim 120\text{ }^{\circ}\text{C}$ . (e) The SEM image for replicated multiscale PUA mold. (f) The cross-sectional SEM image for the catalyst layer on multiscale Nafion membrane.

**Figure 3-3.** Fabricated multiscale Nafion membrane and PUA 311 mold with combination of the micro pillar-patterns and the nano line-patterns.

**Figure 3-4.** Fabricated multiscale Nafion membrane and PUA 311 mold with combination of the micro line-patterns and the nano dot-patterns

**Figure 3-5.** Fabricated multiscale Nafion membrane and PUA 311 mold with combination of the micro line-patterns and the nano line-patterns

**Figure 3-6.** Schematic illustrations for creep response of Nafion membrane (a), instantaneous creep recovery effect during the stamping process (b) and the corresponding simulation results (c)

**Figure 3-7.** Polarization curves of conventional membrane electrode assembly (MEA) and the MEA with the multiscale Nafion

membrane under the conditions of H<sub>2</sub>/Air (a) H<sub>2</sub>/O<sub>2</sub> (b) under ambient pressure and H<sub>2</sub>/Air under pressure of 150 kPa (c). (d) The oxygen gain obtained under ambient pressure.

**Figure 3-8.** Single-cell performance of the MEAs with various pattern dimensions in the conditions of H<sub>2</sub>/Air under ambient pressure

**Figure 3-9.** (a) Equivalent circuit of the PEMFC single cell ( $L_W$  = inductance of the electric wire,  $R_{membrane}$  = internal membrane resistance,  $R_{cathode (anode)}$  = charge transfer resistance of the cathode (anode),  $CPE_{cathode (anode)}$  = constant phase element of the cathode (anode) and  $Z_W$  = Warburg impedance). (b) Electrochemical impedance spectroscopy (EIS) of a conventional MEA and MEA with the multiscale Nafion membrane at 0.5 V. (c) Schematic illustration for the force balancing of a water droplet at a cone-shaped void space in a catalyst layer.

**Figure 3-10.** The contact angle of a DI water droplet on the cathode catalyst layer

**Figure 3-11.** (a) Cyclic voltammogram (CV) of the cathode catalyst layers of a conventional MEA and MEA with the multiscale Nafion membrane. (b) Increased surface area ratio compared to flat surface with various patterned surfaces.

**Figure 4-1.** Schematic for the fabrication of the multiscale prism-patterned membrane by thermal imprinting.

**Figure 4-2.** SEM images of the surface of the multiscale prism-patterned mold.

- Figure 4-3.** SEM images of the surfaces of the (a) flat reference, (b) prism-patterned (P-10), and (c) multiscale prism-patterned (MP-10) membranes; FIB-assisted cross-sectional SEM images of the anode catalyst layers of the prepared CCMs with a (d) flat surface, (e) prism pattern (P-10), and (f) multiscale prism pattern (MP-10).
- Figure 4-4.** AFM images of the surface of the prism-patterned (P-10) and multiscale prism-patterned (MP-10) membranes.
- Figure 4-5.** Relative membrane-electrode interface area of the flat reference, prism-patterned (P-10) and multiscale-patterned (MP-10) membrane.
- Figure 4-6.** (a–b) Single cell polarization curves and (c–d) EIS spectra of the reference MEA, MEAs with patterned membranes (P-10 and MP-10), and MEAs with patterned membranes containing a Au layer with guided cracks (P-10-Au and MP-10-Au).
- Figure 4-7.** (a) Anode polarization curves and (b) anode EIS spectra of the reference MEA and MEAs with prism- (P-10) and multiscale prism-patterned (MP-10) membranes.
- Figure 4-8.** Single cell polarization curves under hydrogen-oxygen operation of all the MEAs including MEAs with patterned-membranes (P-10 and MP-10) and MEAs with patterned-membranes containing a Au layer with guided cracks (P-10-Au and MP-10-Au)..
- Figure 4-9.** Cyclic voltammograms of the anode catalyst layers of the reference MEA and MEAs with prism- (P-10) and multiscale prism-patterned (MP-10) membranes.

**Figure 4-10.** (a) Schematic for generating guided Au cracks by simple mechanical stretching (strain of  $\sim 0.25$ ) and (b) SEM images of the surfaces of prism-patterned (P-10-Au) and multiscale prism-patterned (MP-10-Au) membranes with guided Au cracks.

**Figure 4-11.** Limiting current density measurements for the reference MEA, MEAs with patterned membranes (P-10 and MP-10), and MEAs with patterned membranes and a guided Au cracked layer (P-10-Au and MP-10-Au).

**Figure 4-12.** Cyclic voltammogram (CV) of the anode catalyst layers of all the MEAs including MEAs with patterned-membranes (P-10 and MP-10) and MEAs with patterned-membranes containing a Au layer with guided cracks (P-10-Au and MP-10-Au).

**Figure 4-13.** Schematic illustration of the effects of the enlarged interfacial area and the guided Au cracked barrier.

**Figure 4-14.** Single cell polarization curves under the 1.5 M methanol-oxygen (or air) operation of reference MEA and multiscale patterned MEA with Au layer with guided cracks (MP-10-Au). The flow rate of oxygen and air were identical ( $200 \text{ ml min}^{-1}$ ).

**Figure 4-15.** (a) Single cell polarization curves and (c) EIS spectra of the MEAs including reference MEA, MEA with intact Au layer (Intact Au), MEA with randomly cracked Au layer (Random Au) and MEAs with patterned membranes containing a Au layer with guided cracks (P-10-Au and MP-10-Au).

**Figure 4-16.** SEM images of the surfaces of the intact Au layer and randomly cracked Au layer on flat membrane.



# Nomenclature

$\lambda$	Wavelength
$n$	The real parts of the refractive index
$k$	The imaginary parts of the refractive index
$\Delta P_L$	Laplace pressure
$\gamma$	Surface tension
$R$	Radius of curvature
$T_g$	Glass temperature
$E_0$	Standard potential
$F$	Faraday's constant
$a$	Chemical activity

# Chapter 1. Introduction

---

Multiscale hierarchical structures, the combined structures of micro- and nano-scale repeated pattern, have received great attention due to their unique functions and structural advantages from individual micro- and nano-scale morphology simultaneously<sup>1-5</sup>. Generally, microstructures provide enhanced mechanical properties (e.g., stability, strength, and flexibility)<sup>6</sup> and geometrical effects such as controlled optical pathlength<sup>7-8</sup> and gas/liquid flow<sup>9</sup>. Whereas nanostructures exhibit unique functionalities including plasmonic effects<sup>10</sup>, quantum size effects<sup>11</sup>, anti-reflection characteristics<sup>12</sup> and structural color<sup>6</sup> as well as excellent catalytic<sup>13</sup> and ion/electron transport properties<sup>14</sup> due to the large surface to volume ratio characteristic. Examples are abundantly found in natures including self-cleaning function of lotus leaves with super-hydrophobicity<sup>6</sup>, directional adhesion property of gecko feet<sup>15</sup>, anti-reflection effect of moth-eye<sup>12</sup>, and structural color of morph butterfly wings<sup>16</sup>, and some mechanically reinforced multiscale structures such as exoskeleton of the sheep crab<sup>5</sup> and flexible dermal armor of the arapaima fish<sup>17</sup>. Based on these intriguing properties of multiscale structures that provide multifunctional properties to the raw material without any chemical treatment, recently, there have been many approaches to apply these multifunctional properties into electronics<sup>18-19</sup> and energy systems<sup>20-21</sup> using various processes. With

conventional multiscale-patterning processes, however, introducing the nano-scale patterns both on the top and bottom side of micro-patterns and multi-level structuring are hard to achieve<sup>22-24</sup>.

Solar cells has been considered as one of the most promising candidates to replace fossil fuels, which suffer from limited quantities and environmental issues<sup>25</sup>. Especially, low-cost photovoltaics based on nanostructured oxide semiconductors and inorganic/organic light absorbers (e.g. mesoscopic sensitized solar cells and perovskite solar cells) are gaining great interests as promising alternatives to conventional silicon solar cells due to their low manufacturing costs, relatively high energy conversion efficiencies and the steep performance increase<sup>26-28</sup>. In these types of solar cells, charge collection and light harvesting properties of the nano-oxide (typically  $\text{TiO}_2$ ) films are among the most important factors that determine the overall energy conversion efficiency<sup>29</sup>. Until now, various attempts have been made on improvement of light harvesting in mesoscopic dye-sensitized solar cells (DSSCs) by employing patterned structures on the mp- $\text{TiO}_2$  electrodes<sup>30-32</sup>. However, these patterning techniques have intrinsic limitation that the insertion of periodic architectures is confined to the single-level 2-dimensional structures.

Similarly, much attention has been paid to fuel cells as promising efficient and non-polluting power sources because they offer higher energy densities and energy efficiencies compared to other current/conventional

systems<sup>33-35</sup>. Fuel cells are electrochemical energy conversion systems that transform the chemical energy of a fuel (e.g. hydrogen, methanol, etc.) and an oxidant (air or oxygen). Among the fuel cell systems, Polymer electrolyte membrane fuel cells (PEMFC) and direct methanol fuel cells (DMFC) have extensively studied for automotive applications<sup>36</sup> and portable power-sources<sup>35</sup>. Nonetheless, to commercialize PEMFC and DMFC, some obstacles, such as water management in PEMFC, methanol crossover problems in DMFC and high-cost of Pt catalyst in both systems, need to be overcome<sup>34-35</sup>. To resolve the issue of methanol crossover, many approaches have been adopted, such as developing organic/inorganic composite membranes<sup>37-38</sup> and embedding a methanol barrier layer into the membrane surface<sup>39-40</sup>. To resolve other issues, namely Pt utilization and water management, many studies have examined the incorporation of a patterned membrane into fuel cell devices using a simple one-dimensional micro-/nano pattern. An enlarged interfacial area between the anode and the electrolyte membrane using nano-patterned membrane resulted in higher Pt utilization of fuel cells<sup>41-42</sup>. Also, micro-patterned membrane showed enhanced water transport property by introducing macro-void between electrode and gas diffusion layer (GDL)<sup>34, 43</sup>. However, using these simple one-dimensional patterning techniques, obtaining both effects of nanostructures and microstructures is not easy. Also, in DMFC, achieving low methanol crossover and high proton conductivity simultaneously has

been challenging by simple composite membrane due to methanol permeation resulting from the electro-osmotic drag caused by hydrated protons and diffusion.

To address the remained issues and overcome the limitations, we have developed two novel and facile methods to achieve multilevel multiscale structures; 1. Oxygen-assisted multiplex lithography<sup>42</sup>, which employs partially cured polymeric membrane as a basic brick to be implemented in a vertical stacking and bonding procedure, 2. Creep-assisted sequential imprinting technique, which consists of the first step of thermal imprinting with nano patterns and the following step of imprinting with micro patterns utilizing the creeping behavior of viscoelastic polymer. With the multilevel multiscale structures, we could achieve enhanced optical properties in DSSCs and improved device performance of PEMFC and DMFC. In DSSCs, we performed investigations on photonic application of multilevel multiscale patterned nano-oxide photoelectrodes for efficient light harvesting. The z-axis integration of nano- and micro-patterns resulted in superpositioned optical responses from nano- and micro-scale structures, enabling synergistic photon trapping within the photoelectrode by simultaneous diffraction grating and light scattering. In addition, in PEMFC, the multilevel multiscale patterned membranes, where the nanopatterns covered the whole surface even on the side surface of microstructures, have brought significantly improved device performance. The enhancement was

attributed to the decrease of mass transport resistance due to unique morphology of micro-patterns by creep-recovery effects and the increase of interfacial surface area between membrane and electrocatalyst layer. Furthermore, in DMFC, the multiscale patterned membrane resulted in enhanced performance by improving mass transport, active site utilization, and Pt utilization. Also, additionally incorporated a guided gold cracked layer effectively reduced the methanol crossover rate while maintaining the proton transport ability owing to the existence of multiple cracks.

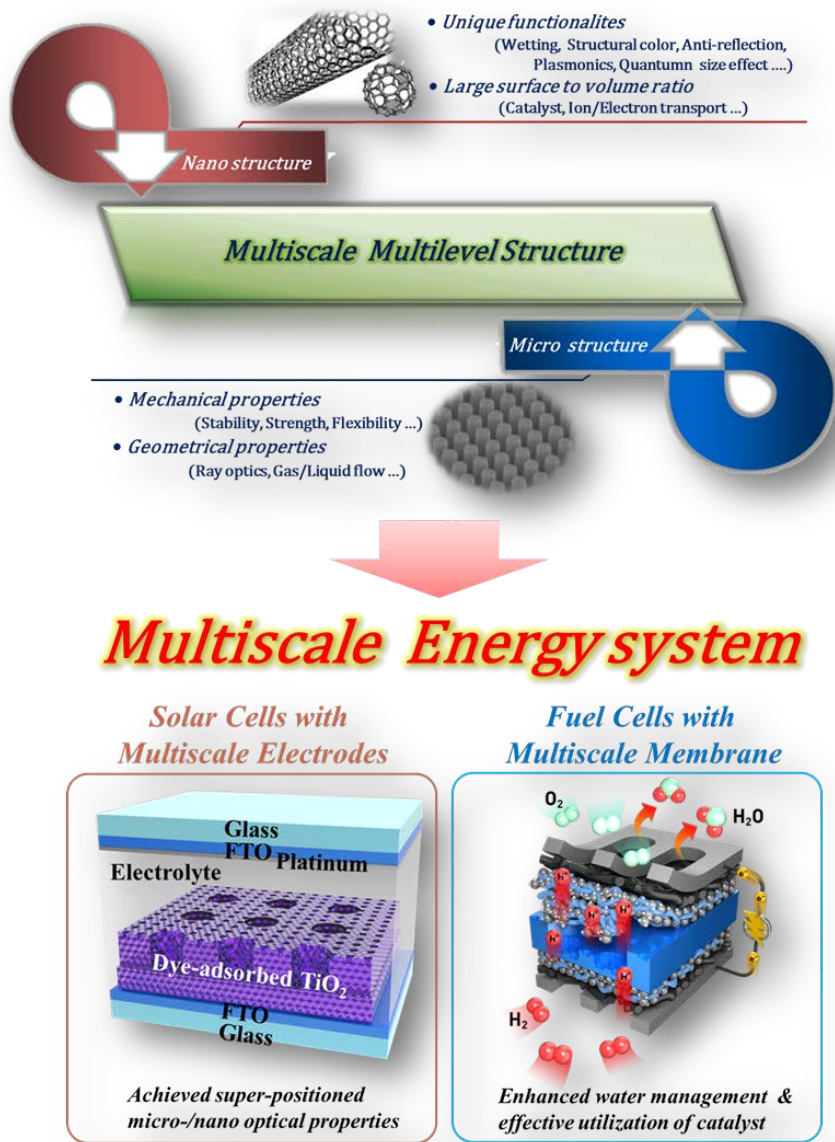


**Figure 1-1.** Brief introduction of the effects of multiscale structures which consist of nano-/micro-structures and its applications for improved optical properties of solar cells and high performance fuel cells

In *Chapter 2*, we demonstrate a strategy for efficient photon harvesting based on the multilevel multiscale structures prepared by using multiplex lithography for constructing LEGO<sup>®</sup>-like architectures. Multilayer assembly of polyurethane acrylate (PUA) films with nano- or micro-apertures (or patterns) was enabled by oxygen-assisted partial curing of PUA resin. Based on the different amount of uncured degree of PUA films between the bottom and top surface, partially cured bottom surface of PUA film was used for adhesion to micro- or nano- patterned PUA membrane while proper nanostructures were imprinted on the relatively less cured top surface of the PUA. After, PDMS molds with multilevel structures comprising nano- and micro-structures projected on the whole surface were replicated. Then, mesoporous (mp)-TiO<sub>2</sub> films with multilevel nano- and micro-patterns were prepared by using one-step elastomer stamping method. Various optical measurements and simulations were performed in order to confirm the optical characteristics of our multilevel multiscale structures, and superpositioned optical interferences induced by periodic nano-patterns and micro-patterns were observed. We verified the effectiveness of our approach by utilizing patterned mp-TiO<sub>2</sub> film in DSSCs. Under standard 1 sun illumination, over 17.5 % enhancement in energy conversion efficiency was achieved by overlapped optical enhancements aroused from nano- and micro-patterns.



In *Chapter 3*, we suggest a facile and simple multiscale patterning method called creep-assisted sequential imprinting and its application to PEMFC. The creep behavior is the phenomenon of a solid material to be deformed permanently even below the glass temperature under the long-term exposure to mechanical stresses. By using this creep behavior, we sequentially imprinted nano- and micro-scale patterned-mold onto a viscoelastic polymer film: the first step of thermal imprinting with nano patterns and the following step of creep-assisted imprinting with micro patterns and finally, replicating step through casting and UV curing of PUA on the patterned film was performed. The completed multiscale mold shows the nano-patterns well remained after the second stamping procedure thanks to the creep behavior of Nafion. Interestingly, even on the side surface of micro-sized hole-patterns, the nano-patterns clearly remained. For verifying the practical usage of multiscale structures, multiscale patterned membrane was incorporated into PEMFC. With micro-patterns in multiscale patterned membrane, regular empty space was formed in catalyst layer and showed positive effect on mass transfer in cathode side. In addition, the enlarged interfacial surface between catalyst layer and patterned membrane resulted in high Pt utilization. The combined effects of improved mass transport and increase of Pt utilization brought improved device performance of PEMFC.

In *Chapter 4*, we propose interface engineering method to introduce a multiscale patterned membrane and a guided metal cracked layer in

DMFC by the creep-assisted sequential imprinting and simple stretching technique. Using the creep-assisted sequential imprinting method, we easily fabricated a multiscale hierarchical-structured membrane with a high surface area. The device with the multiscale patterned membrane showed improved performance compared with that of the reference because mass transport was enhanced by the thinned electrode and the effective utilization of catalytic active sites. Moreover, the electrochemically inactive thin gold layer was expected to act as a physical barrier for methanol crossover and the guided cracks provided multiple proton pathways. By combining synergetic effects of higher Pt utilization, enhanced mass transport and reduced methanol crossover, the device performance of DMFC was significantly enhanced by 42.3% compared with that of the reference.

## **Chapter 2. Oxygen-assisted multiplex lithography and its application to solar cells**

---

Published in Advanced Functional Materials, 2016, 26, 6584

### **2-1. Introduction**

Among various sustainable energy sources, solar energy has been considered as one of the most promising candidates to replace fossil fuels, which suffer from limited quantities and environmental issues<sup>25</sup>. Though being challenged by demands on high energy density, recent advances on the development of highly efficient photovoltaics are raising the expectations for large scale practical utilization of solar energy<sup>44</sup>. Especially, low-cost photovoltaics based on nanostructured oxide semiconductors and inorganic/organic light absorbers (e.g. mesoscopic sensitized solar cells and perovskite solar cells) are gaining great interests due to the steep rise in performance<sup>26-28, 45-53</sup>. In these types of solar cells, charge collection and light harvesting properties of the nano-oxide (typically TiO<sub>2</sub>) films are among the most important factors that determine the overall energy conversion efficiency<sup>29</sup>. Significant progress in charge collection was achieved by structural engineering of oxides, however, trade-off between minimizing the traveling distance of excitons and maximizing the surface area for efficient utilization of incident photons caused limitations to further

advances<sup>54-61</sup>. In contrast, significant improvements were made by tailoring the optical characteristics of nano-oxide films<sup>62-63</sup>. Various types of approaches such as elongation of light pathways within the oxide film (light trapping) by incorporation of light scattering materials<sup>64-67</sup> or photonic crystals<sup>68-73</sup> have been reported, and insertion of metallic nano-architectures for surface plasmon resonance has delivered significant enhancements<sup>74-78</sup>.

On the basis of understanding on the optical properties of periodic nanostructures, Kim et al. reported nano-line patterned mesoporous TiO<sub>2</sub> (mp-TiO<sub>2</sub>) film fabricated by imprinting the nano-lines on mp-TiO<sub>2</sub> by using a polydimethylsiloxane (PDMS) mold. Diffraction gratings induced by the patterns within the photoelectrode substantially enhanced light harvesting properties, which led to significantly increased efficiency in dye-sensitized solar cells (DSSCs)<sup>79</sup>. Micro-patterned mp-TiO<sub>2</sub> photoanodes for DSSCs were reported shortly after, and prolonged light pathways due to the reflections at TiO<sub>2</sub>/electrolyte interfaces with ~25  $\mu$ m-sized patterns were verified by experimental results and optical simulations<sup>80</sup>. Until now, various attempts have been made on improvement of light harvesting in mesoscopic solar cells by employing patterned structures on the mp-TiO<sub>2</sub> electrodes<sup>30-31, 81-84</sup>. However, these patterning techniques have intrinsic limitation that the insertion of periodic architectures is confined to the single-level 2-dimensional structures. Lately, Na et al. performed stacking of thin mp-TiO<sub>2</sub> layers with nano-line patterns in different directions (i.e.

alignments of multilayer nano-lines with 45° or 90° tilting), and verified the effectiveness of their strategy by achieving enhancements in light harvesting, which resulted from diffraction grating-induced multiple reflections<sup>32</sup>. Though this elaborate technique to overcome the limitation is highly appreciable, multi-layering procedure of mesoporous oxide film comprises numerous and complicated steps which hinder practical utilization of this method.

Herein, we demonstrate a strategy for efficient photon harvesting based on the multilevel multiscale structures prepared by using multiplex lithography for constructing LEGO®-like architectures<sup>42</sup>. Multilayer assembly of polyurethane acrylate (PUA) films with nano- or micro-apertures (or patterns) was enabled by UV-curable properties of PUA<sup>85</sup>, and PDMS films with multiscale patterns comprising nano- and micro-structures projected on the whole surface were replicated. Then, mp-TiO<sub>2</sub> films with multilevel nano- and micro-patterns were prepared by using one-step elastomer stamping method, which is a feasible and reliable procedure<sup>86</sup>. Various optical measurements and simulations were performed in order to confirm the optical characteristics of our multilevel multiscale structures, and superpositioned optical interferences induced by periodic nano-patterns<sup>87-89</sup> and micro-patterns<sup>90-91</sup> were observed. We verified the effectiveness of our approach by utilizing patterned mp-TiO<sub>2</sub> film in DSSCs, which served as a model system. Under standard 1 sun illumination, over

17.5 % enhancement in energy conversion efficiency primarily caused by increased photocurrent density was achieved. Also, by comparing the incident photon-to-current efficiency (IPCE) with optical measurement results, we could confirm that the improved light harvesting in the optoelectronic device has been originated from the manifestation of overlapped optical enhancements aroused from nano- and micro-patterns.

## 2-2. Experimental

### *Fabrication of Multilevel Multiscale Patterned PDMS Molds by Multiplex Lithography*

A small amount of hydrophilic polymer resin (PUA311; Minuta Tech.) was dispensed onto a 20  $\mu\text{m}$  pillar PDMS mold, and a flat PDMS blanket was placed on the top, uniformly covering the patterned PDMS mold by conformal contact. Then this sandwich-like assembly was exposed to UV light ( $\lambda = 250 - 400 \text{ nm}$ ) for a short time ( $< 2 \text{ min}$ ) under an applied pressure ( $\sim 500 \text{ g/cm}^2$ ) for partial curing of PUA. After obtaining the free-standing PUA membrane with 20  $\mu\text{m}$  aperture, uncured part of this membrane at the bottom surface was used for adhesion to a 400 nm hole or 400 nm line patterned PUA membrane. Also, 400 nm dot or 400 nm line patterns were imprinted on the unpolymerized top surface of the PUA, by irradiating UV light ( $> 5 \text{ min}$ ,  $\lambda = 250\text{-}400 \text{ nm}$ ) with hydraulic pressure ( $10 \text{ kg/cm}^2$ ) in a vacuum chamber ( $5 \times 10^{-2} \text{ Torr}$ ). After removal of the PDMS mold, a PUA with multiscale and multilevel (-) patterned structure was formed. This PUA substrate was used for the replication of PDMS film with multilevel multiscale (+) patterns. A mixture of base and curing agents (10:1 w/w) of PDMS (Sylgard 184, Dow Corning) was dispensed into PUA substrate and cured at  $70^\circ\text{C}$  for 1.5 h, and the multilevel multiscale PDMS mold was obtained by peeling off the PDMS from the PUA.

***Preparation of Multiscale and Multilevel Multiscale Patterned mp-TiO<sub>2</sub> Photoelectrodes and DSSCs.***

A compact TiO<sub>2</sub> blocking layer was deposited onto the FTO glasses (TEC-8, Pilkington) by dipping the glasses in a 40 mM TiCl<sub>4</sub> aqueous solution at 70 °C for 30 min. Then, commercial colloidal TiO<sub>2</sub> paste (DSL 18NR-T, Dyesol) with neutral pH was cast onto the FTO substrate by doctor-blading method. Then, multilevel multiscale PDMS mold was placed onto the TiO<sub>2</sub> film and was gently pressed, followed by drying process at 70 °C for 20 min. The PDMS mold was then detached from the TiO<sub>2</sub> film, and the TiO<sub>2</sub> nanoparticle paste on the FTO was annealed at 500 °C in air for 30 min. After TiCl<sub>4</sub> post-treatment for increased dye-loading and charge injection<sup>92</sup>, sintered TiO<sub>2</sub> nanoparticles were dye-sensitized by dipping the film in the ethanolic solution of 0.5 mM N719 dye (Ruthenizer 535-bis TBA, Solaronix) at 30 °C for 48 h. Platinized FTO electrode prepared by thermal decomposition was used as counter electrode for DSSCs, and a 50 μm thick thermoplastic sealant (Surlyn, DuPont) was used for cell assembly<sup>93</sup>. Then, I<sub>3</sub><sup>-</sup>/I<sup>-</sup> redox electrolyte composed of 0.6 M 1-butyl-3-methylimidazolium iodide, 30 mM I<sub>2</sub>, 0.1 M guanidinium thiocyanate, and 0.5 M 4-tert-butylpyridine in a mixture of acetonitrile and valeronitrile (volumetric ratio = 85:15) was injected into the cell through the pre-drilled holes.



### ***Physical and Electrochemical Measurements***

SEM images were obtained by using Carl Zeiss MERLIN compact, and optical measurements were performed with Perkin-Elmer Lambda 45 spectrophotometer. Evaluations of photovoltaic performances were done by using a solar simulator (XIL model 05A50KS source measure units, SERIC Ltd.) which was calibrated to a 1 sun condition (AM 1.5G with an incident light intensity of 100 mW/cm<sup>2</sup>) based on a standard Si solar cell certified by National Institute of Advanced Industrial Science and Technology (AIST, Japan). A potentiostat (Solartron 1480) was used for measurements of J-V characteristics, and IPCE spectra were obtained with QEX7 manufactured by PV Measurements.

### ***Optical Simulations***

Full-wave electromagnetic simulation was performed by using Lumerical FDTD simulation software ([www.lumerical.com](http://www.lumerical.com)). The simulation structure was based on the experimental observations on the actual single-level and multilevel patterned mp-TiO<sub>2</sub> electrodes based on SEM analyses (**Figure 2-7**). The real parts (n) of the refractive indices of the mp-TiO<sub>2</sub> and glass substrate layers were chosen to be 2.258 and 1.34, respectively, while the imaginary parts (k) of the refractive indices were both set to zero by assuming lossless layers. The plane wave source with a wavelength ranging from 350 nm to 700 nm was placed inside the glass

substrate and impinged along the z-direction (vertical direction to the device structure). The periodic boundary conditions for x-axis, y-axis, and the perfectly matched layer for z-axis were imposed on the unit-cell structure. Then, the spectral reflectances of the single- and multilevel patterned electrodes were compared with that of the flat electrode.

## **2-3. Results and Discussion**

### **2-3-1. Fabrication of polymeric molds with multiscale multilevel structures by controlling oxygen-inhibition**

Preparation of multilevel multiscale PDMS mold was performed according to the procedures described in **Figure 2-1**. First, fabrication of flexible and free-standing PUA membrane with 20  $\mu\text{m}$  apertures was performed. After the deposition of polymer resin (PUA311, Minuta Tech.) onto a PDMS mold with 20  $\mu\text{m}$  pillar-patterns, a flat PDMS blanket was placed on the top, and the sandwiched assembly was exposed to a short UV irradiation for partial curing of the PUA (**Figure 2-1a**). Since the permeable PDMS can let oxygen penetrate through the PDMS layer<sup>94</sup>, uncured thin layers were formed at top and bottom surfaces of the PUA membrane due to oxygen inhibition effect<sup>95</sup>. Also, because of the low affinity between the hydrophilic PUA and hydrophobic PDMS surface, the uncured resin droplets on the PDMS pillars escape to the top surface of PUA film during the removal of PDMS blanket and form a viscoelastic coating on the PUA (**Figure 2-1b and 1c**)<sup>42, 96</sup>. This enables additional imprinting on the top surface with nanopatterned PDMS mold and additional integration of PUA membrane at the bottom. Based on these properties of the PUA membrane, LEGO<sup>®</sup>-like monolithic integration was performed at the bottom of the membrane by putting the membrane onto a film with 400 nm hole or 400

nm line patterns. Simultaneously, imprinting on the top of the membrane was carried out by pressing with 400 nm dot or 400 nm line patterned PDMS mold (**Figure 2-1d**). Then the PDMS film with multilevel multiscale architecture was prepared by performing replication by casting and curing of PDMS pre-polymer onto the integrated multiscale PUA substrate (**Figure 2-1e and 1f**).

**Figure 2-2** shows the scanning electron microscope (SEM) images of multilevel 400 nm dot / 20  $\mu$ m dot (**Figure 2-2a and 2b**) and 400 nm line / 20  $\mu$ m dot (**Figure 2-2c and 2d**) patterned PDMS films, and it is clearly observable that the multilevel multiscale molds have been successfully prepared with high pattern fidelity. Periodic nano-dots or nano-lines were not only present on top of the micro-pillars but also on the floor, enabling both nano- and micro-patterns to be imprinted on the whole surface by complete overlap of nano- and micro-patterns in z-axis direction. In order to investigate the characteristics of multilevel multiscale periodic structure, single-level 400 nm dot, 400 nm line, and 20  $\mu$ m dot patterned PDMS molds were also prepared for proper comparisons between single- and multilevel architectures. The SEM images of single-layer patterned PDMS molds are displayed in **Figure 2-3**.

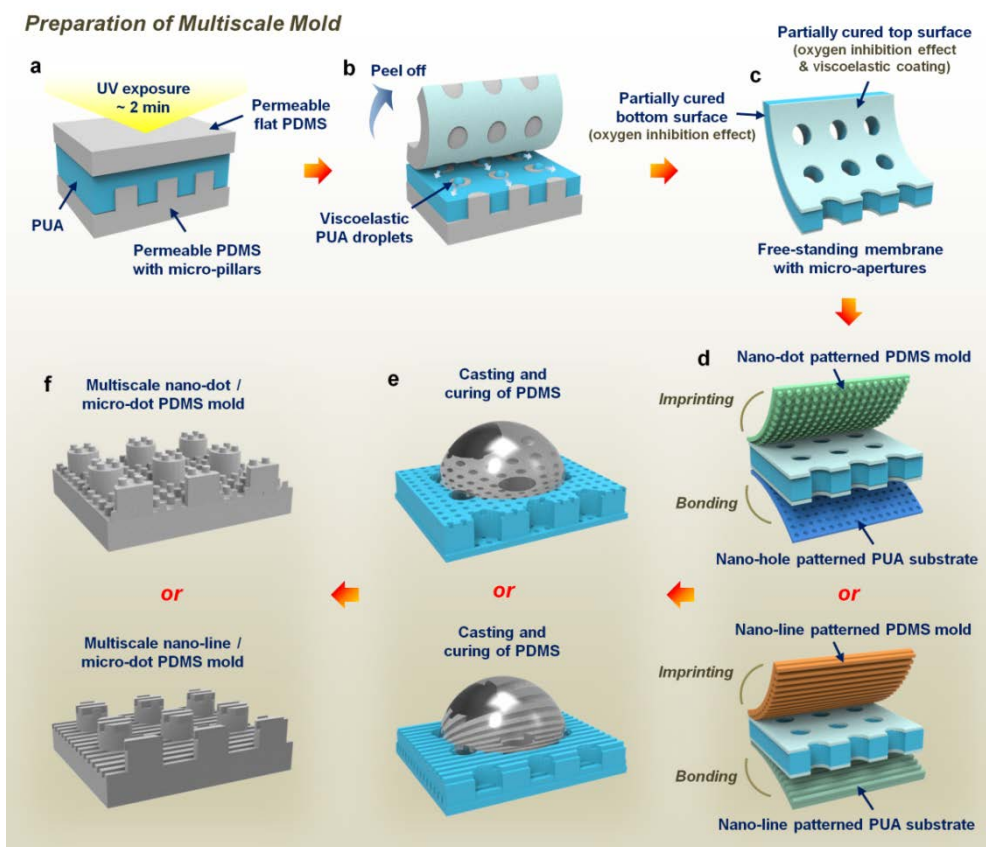


**Figure 2-1.** Schematic illustration describing the procedure for preparation of multilevel multiscale PDMS molds by multiplex lithography and replication.

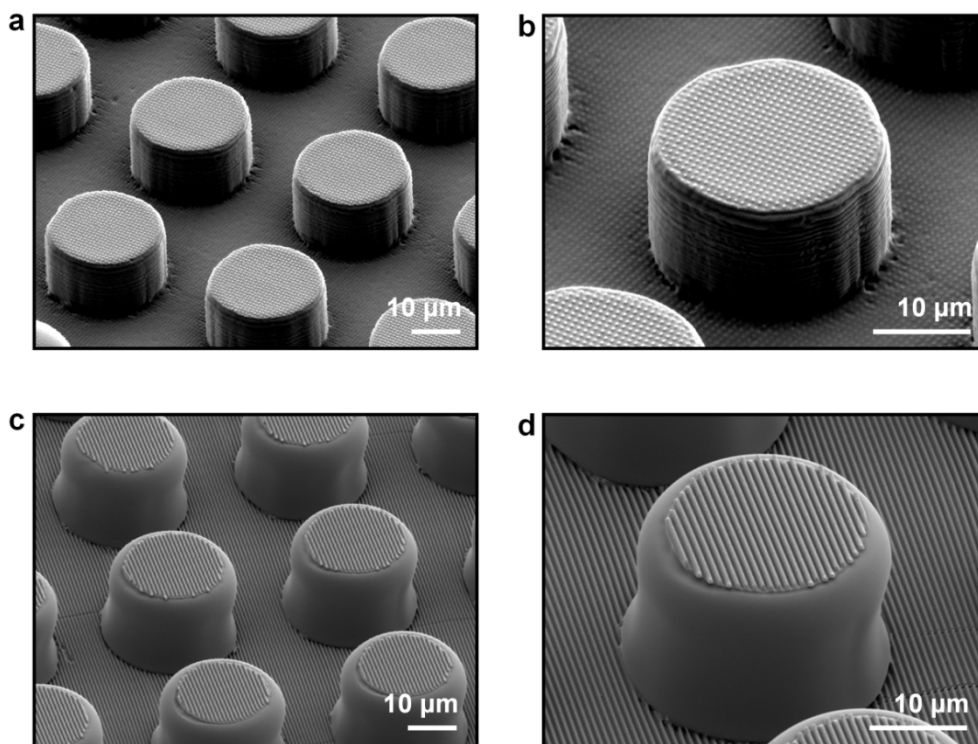


**Figure 2-2.** SEM images of multilevel multiscale PDMS molds. (a,b) 400 nm dot / 20 μm dot patterned PDMS at (a) low and (b) high magnifications. (c,d) 400 nm line / 20 μm dot patterned PDMS at (c) low and (d) high magnifications.

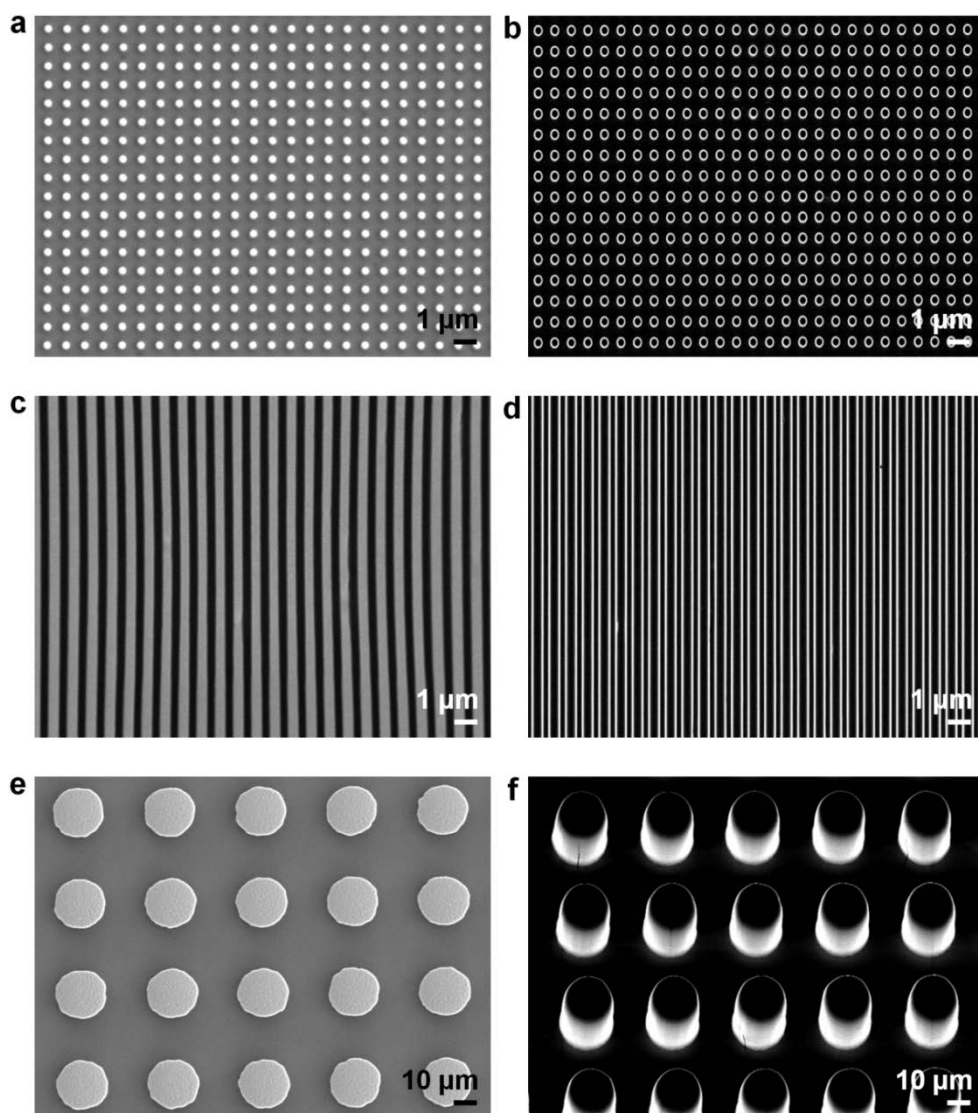


**Figure 2-3.** SEM images of (a,b) 400 nm dot, (c,d) 400 nm line, (e,f) 20 μm dot patterned PDMS molds. The images were obtained by using either (a,c,e) secondary electron (SE2) detector or (b,d,f) in-lens detector.

### 2-3-2. Multiscale multilevel designed mesoporous TiO<sub>2</sub> film

The multilevel multiscale patterned mp-TiO<sub>2</sub> electrodes were prepared by the soft-molding method described in **Figure 2-4**. First, commercial viscous TiO<sub>2</sub> paste (DSL 18NR-T, Dyesol) was casted onto fluorine-doped tin oxide (FTO) glass substrate by doctor-blade method (**Figure 2-4a**). Then, the multiscale PDMS mold with 400 nm dot / 20  $\mu$ m dot or 400 nm line / 20  $\mu$ m dot structures was placed onto the TiO<sub>2</sub> film with a gentle pressure, followed by thermal annealing at 70 °C for 20 min to remove the residual solvent (**Figure 2-4b**). After detaching the PDMS mold, heat treatment was performed at 500 °C for 30 min for sintering of TiO<sub>2</sub> nanoparticles and calcination of organic binders. Consequently, mp-TiO<sub>2</sub> films on FTO glasses with multilevel multiscale patterns on the top-surface were obtained (**Figure 2-4c**). Flat and single-level (400 nm dot, 400 nm line, and 20  $\mu$ m dot) patterned mp-TiO<sub>2</sub> electrodes were also prepared for comparisons.

The morphologies of the patterned mp-TiO<sub>2</sub> electrodes were observed by SEM analyses. **Figure 2-5a-5d** show top-view and cross-sectional SEM images of flat, 400 nm dot, 400 nm line, and 20  $\mu$ m dot patterned mp-TiO<sub>2</sub> films, respectively. The nanostructures were uniformly imprinted onto the top surface of mp-TiO<sub>2</sub>, without inducing significant changes to the overall film thicknesses (around 25  $\mu$ m), which is an important factor governing the charge collection efficiency in mesoscopic solar cells. These features of soft-molding were also observed in the case of multilevel 400 nm dot / 20



$\mu\text{m}$  dot and 400 nm line / 20  $\mu\text{m}$  dot patterned mp-TiO<sub>2</sub> films of which morphologies are visualized by SEM and displayed in **Figure 2-5e** and **Figure 2-5f**, respectively. From the high magnification images in the insets, it is clear that the periodic structures of 400 nm dots or 400 nm lines are neatly imprinted on the surface including micro-patterned regions. Also, we measured the areal dye-loading in order to examine the influences of patterning on the effective surface areas of mp-TiO<sub>2</sub>. The differences in the numbers of loaded dye molecules on flat and patterned mp-TiO<sub>2</sub> films were within 3.5% (see **Table 2-1** for details), indicating that the imprinting procedures caused negligible changes to the surface area. Moreover, viability of these patterning techniques for scaling-up, which is an important aspect for practical applications, was confirmed by preparation of single- and multilevel patterned mp-TiO<sub>2</sub> photoelectrodes with a dimension of 3 cm  $\times$  3 cm as a model size. The digital photographs of the scaled-up TiO<sub>2</sub> films before and after dye-sensitization are shown in **Figure 2-6a** and **Figure 2-8a**, respectively.

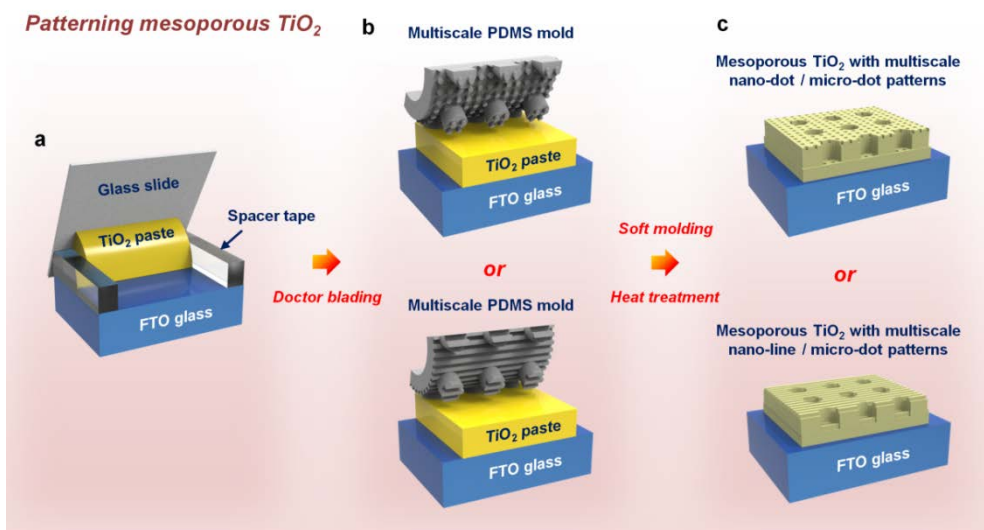


**Figure 2-4.** Schematic illustration describing the methods for preparation of patterned mp- $\text{TiO}_2$  film by soft molding technique.

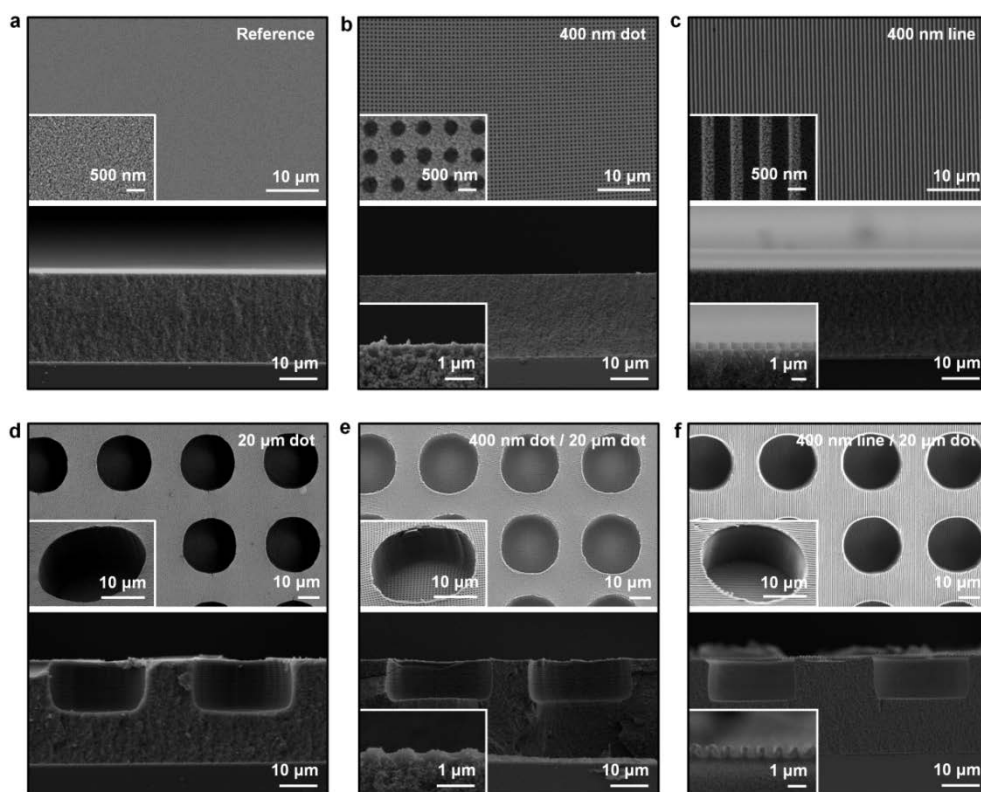


**Figure 2-5.** Top-view and cross-sectional SEM images of (a) flat, (b) 400 nm dot, (c) 400 nm line, (d) 20 μm dot, (e) 400 nm dot / 20 μm dot, and (f) 400 nm line / 20 μm dot patterned mp-TiO<sub>2</sub>.

Sample	Dye-loading ( $\times 10^{-7}$ mol/cm <sup>2</sup> )
Reference	5.35
400 nm dot	5.20
400 nm line	5.21
20 $\mu$ m dot	5.18
400 nm dot / 20 $\mu$ m dot	5.36
400 nm line / 20 $\mu$ m dot	5.29

**Table 2-1.** Loaded dye amounts on flat and patterned mp-TiO<sub>2</sub> photoelectrodes.

### 2-3-3. Super-positioned optical property of multiscale multilevel TiO<sub>2</sub> electrodes

The distinct optical characteristics of the flat, single-level, and multilevel multiscale patterned mp-TiO<sub>2</sub> films on FTO glass substrate were first observed with bare eyes. As can be seen from the photos displayed in **Figure 2-6a**, mp-TiO<sub>2</sub> with periodic 400 nm patterns exhibited iridescent colors which can be attributed to the diffraction gratings within visible light wavelength region. In contrast, light scattering in random directions were present in micropatterned mp-TiO<sub>2</sub>, which can be identified by significantly decreased transparency. Since neither of these optical behaviors are present in the flat mp-TiO<sub>2</sub> film (noted as Reference in **Figure 2-6a**), the observations in patterned TiO<sub>2</sub> are ascribable to the nano- and micro-architectures. Interestingly, both of the optical effects were observable in mp-TiO<sub>2</sub> with multilevel multiscale patterns, implying the co-existence of photonic properties induced by both 400 nm (diffraction grating) and 20  $\mu$ m (light scattering) dimensions in multiscale mp-TiO<sub>2</sub> film, wherein nano- and micro-structures are completely integrated in z-axis direction.

Then, reflectance measurements were performed in visible light wavelength region for quantitative investigations on the optical properties of multilevel multiscale architectures. **Figure 2-6b** shows the reflectance spectra of the flat and patterned mp-TiO<sub>2</sub> photoanodes, which were measured by light irradiation from the glass side considering the potential

photovoltaic applications. Compared to the flat mp-TiO<sub>2</sub>, single-level 400 nm dot and 400 nm line patterned mp-TiO<sub>2</sub> films exhibited enhanced reflectivity over the wavelength range of 350 nm to 700 nm, especially to a large extent in a relatively short wavelength region below 500 nm. On the contrary, single-level 20 μm dot patterned TiO<sub>2</sub> film exhibited increased reflectance at the wavelengths higher than 400 nm, and its magnitude beyond the wavelength of 500 nm became larger than that of 400 nm dot and 400 nm line patterned cases. As have been expected from the examinations on digital photographs in **Figure 2-6a**, the multilevel 400 nm dot / 20 μm dot and 400 nm line / 20 μm dot patterned TiO<sub>2</sub> electrodes manifested largest increments in spectral reflectance, by superpositioned optical properties of the constituent 400 nm dot or line and 20 μm dot patterns. Additionally, it was noteworthy to observe that the spectral reflectance were larger in 400 nm line pattern than 400 nm dot pattern, in both single-level and multilevel architectures.

Our experimental measurements on increased reflectance were cross-checked with full electromagnetic simulation results. **Figure 2-7** displays the spectral enhancement factors of single-level 400 nm line, 20 μm dot, and multilevel 400 nm line / 20 μm dot patterned mp-TiO<sub>2</sub> compared to the flat reference. The refractive indices of 2.258 and 1.34 were adopted for the mp-TiO<sub>2</sub> layer and the glass substrate, respectively,<sup>79, 97</sup> without considerations on absorption loss. The calculated results clearly show the enhanced

reflectance at wavelengths below 580 nm in the case of 400 nm line patterned  $\text{TiO}_2$ , which was mainly attributed to the diffraction effect by nano-lines. On the other hand, increment at wavelengths longer than 600 nm was present in 20  $\mu\text{m}$  dot patterned electrode, primarily caused by the random scattering caused by rounded edges in micro-dots (SEM images are displayed in **Figure 2-5d-5f**). Multilevel multiscale 400 nm line / 20  $\mu\text{m}$  dot patterned mp- $\text{TiO}_2$  exhibited substantial enhancement over the whole visible light range, due to the combined effects of diffraction grating and random scattering by both nano- and micro-architectures, respectively. The simulation results coincided well with the experimental observations.

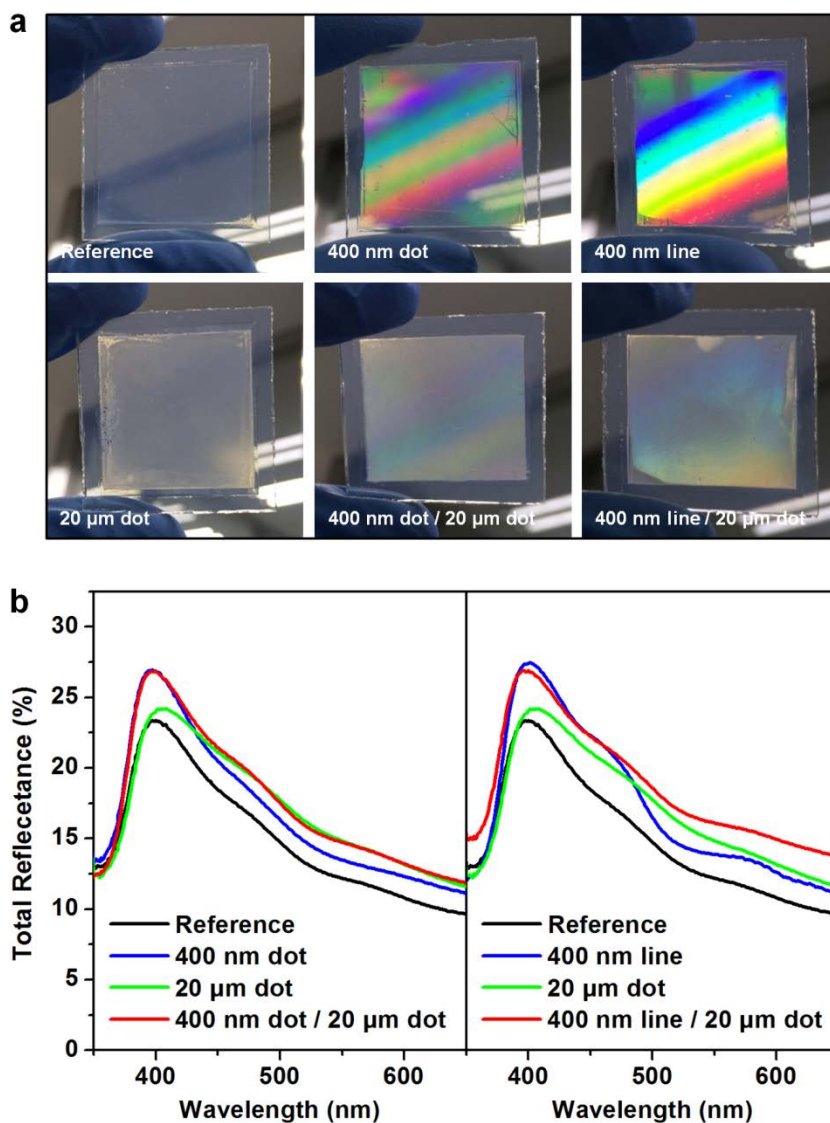


**Figure 2-6.** (a) Digital photographs of flat (noted as Reference) and patterned (detailed architectures noted at each image) mp-TiO<sub>2</sub>. (b) Reflectance spectra of flat and patterned mp-TiO<sub>2</sub>.



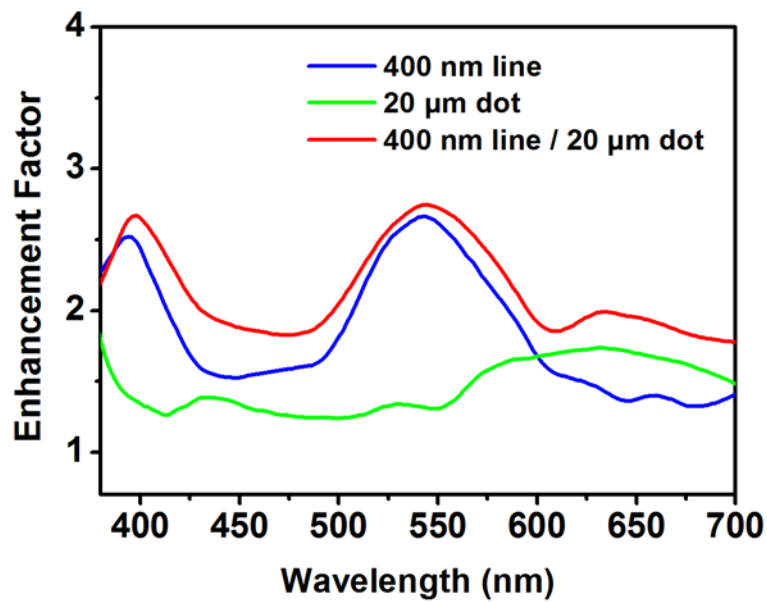


**Figure 2-7.** Calculated light reflection enhancement of patterned mp-TiO<sub>2</sub> compared to flat mp-TiO<sub>2</sub> from FDTD simulation.

### **2-3-4. Enhanced performance of multiscale architected dye-sensitized solar cell**

Then we investigated light harvesting characteristics of N719 dye-sensitized mp-TiO<sub>2</sub> films, in order to ascertain the validity of our approach in state-of-the-art photoelectrode. **Figure 2-8a** shows the digital photographs of N719-sensitized flat and patterned mp-TiO<sub>2</sub>. Although the dye loading amounts are almost the same for both flat and patterned photoelectrodes (see **Table 2-1**), presence of 400 nm patterns resulted in darker coloration, indicating that more photons are trapped in nano-patterned photoelectrodes. In case of the micro-patterned mp-TiO<sub>2</sub>, randomized light scattering were observable from the significant drop in transparency which makes the background images completely undistinguishable. For a more detailed discussion on the light harvesting properties, absorbance spectra of dye-sensitized photoelectrodes were obtained in the visible light region, and the results are displayed in **Figure 2-8b**. By comparing the cases of flat, 400 nm dot, and 400 nm line patterned TiO<sub>2</sub>, significant enhancement in light absorption properties at low wavelength regions (< 550 nm) are observable in nano-patterned oxide films. Also, superior light harvesting characteristic of 400 nm line patterns to that of 400 nm dot patterns were confirmed, as have been verified in reflectance analyses (**Figure 2-6**) and slightly different degrees of coloration after dye-sensitization (**Figure 2-8a**). In contrast, 20  $\mu$ m dot patterns induced larger

increase of absorbance in longer wavelength range compared to the mp-TiO<sub>2</sub> with 400 nm patterns. Most importantly, multilevel multiscale patterned mp-TiO<sub>2</sub> exhibited largest absorbance in whole visible light region with superpositioned optical properties of nano- (diffraction grating) and micro-scale (randomized light scattering) architectures. Meanwhile, 400 nm line / 20  $\mu$ m dot case was better than 400 nm dot / 20  $\mu$ m dot, as could have been expected by the results from single-layer patterned photoelectrodes.

For the verification of the effectiveness of multilevel multiscale patterned mp-TiO<sub>2</sub> photoelectrodes, DSSCs employing N719-sensitized TiO<sub>2</sub>, platinized FTO counter electrode, and I<sub>3</sub><sup>-</sup>/I<sup>+</sup> redox electrolyte were prepared. **Figure 2-9a** and 8b show the photocurrent density ( $J$ )-voltage ( $V$ ) characteristics of the DSSCs with various single- and multilevel patterned TiO<sub>2</sub> films, and the detailed photovoltaic parameters are summarized in **Table 2-2**. Though differences in open-circuit voltage ( $V_{oc}$ ) and fill factor ( $FF$ ) values were not significant (less than 3%), changes in short-circuit photocurrent density ( $J_{sc}$ ) were varied with strong dependence on the types of patterns imprinted on mp-TiO<sub>2</sub>.  $J_{sc}$  increased as periodic structure of 400 nm dot, 400 nm line, or 20  $\mu$ m dot was inserted on the mp-TiO<sub>2</sub>, from 13.0 mA/cm<sup>2</sup> to 13.9 mA/cm<sup>2</sup>, 14.4 mA/cm<sup>2</sup>, or 14.1 mA/cm<sup>2</sup>, respectively. The degree of increments was much larger when multilevel multiscale structures were utilized, and the  $J_{sc}$  values exceeded 15 mA/cm<sup>2</sup> in both 400 nm dot / 20  $\mu$ m dot (15.1 mA/cm<sup>2</sup>) and 400 nm line / 20  $\mu$ m dot (15.2 mA/cm<sup>2</sup>) cases.

Accordingly, the average conversion efficiencies of DSSCs with multilevel patterns were the highest, exhibiting 15.0% and 17.5% enhancements in 400 nm dot / 20  $\mu$ m dot (8.19%) and 400 nm line / 20  $\mu$ m dot (8.37%) patterned DSSCs compared to the reference (7.12%). Comparison between the efficiencies of DSSCs with single-level patterns and multilevel multiscale patterns clearly show that the multiple periodic architectures are effective strategies to enhance the overall performance of mesoscopic solar cells.

In order to confirm the origin of the enhancements in photocurrent densities and energy conversion efficiencies, IPCE measurements were performed. **Figure 2-9c** and **Figure 2-9d** show the IPCE spectra of DSSCs employing flat, single- and multilevel patterned mp-TiO<sub>2</sub> photoanodes. The spectral characteristics of IPCE values were in accordance with the absorption results discussed above (**Figure 2-8b**). The 400 nm patterns induced more efficient photon utilization at relatively shorter wavelength lights, whether the periodic 20  $\mu$ m dots exhibited enhancements in whole visible light region with comparative superiority to 400 nm in the harvesting of low energy (long wavelength) photons. From the observation of integrated improvements resulted from the constituent single-scale structures in multilevel multiscale mp-TiO<sub>2</sub> based DSSCs, we could verify the manifestation of synergistic improvements in the case of multilevel patterned DSSCs, by complementary superposition of optical responses of constituent nano- and micro-patterns.

Additionally, in order to demonstrate the general merits of our multiscale approach, we also prepared DSSCs with 800 nm dot, 800 nm line, 800 nm dot / 20  $\mu$ m dot, and 800 nm line / 20  $\mu$ m dot patterned mp-TiO<sub>2</sub> photoanodes. As can be seen from the SEM images displayed in **Figure 2-10**, the patterns were uniformly imprinted on the mp-TiO<sub>2</sub> film by soft-molding, and full projection of nano- and micro-patterns by z-axis integration were observable in multilevel multiscale mp-TiO<sub>2</sub>. When these photoelectrodes were employed in DSSCs, significantly enhanced  $J_{sc}$  and energy conversion efficiencies with the similar trends to 400 nm / 20  $\mu$ m cases were obtained, as can be seen from the  $J$ - $V$  curves in **Figure 2-11** and detailed summary in **Table 2-3**. DSSCs with 800 nm dot and 800 nm line patterned mp-TiO<sub>2</sub> photoanodes showed enhanced  $J_{sc}$  and efficiency compared to the flat reference, and further increases were obtained by integration of 800 nm patterns with periodic 20  $\mu$ m dots. Though the combination of 800 nm and 20  $\mu$ m patterns were slightly inferior to multilevel 400 nm / 20  $\mu$ m cases, general effectiveness of our multiscale z-axis integration strategy was confirmed.

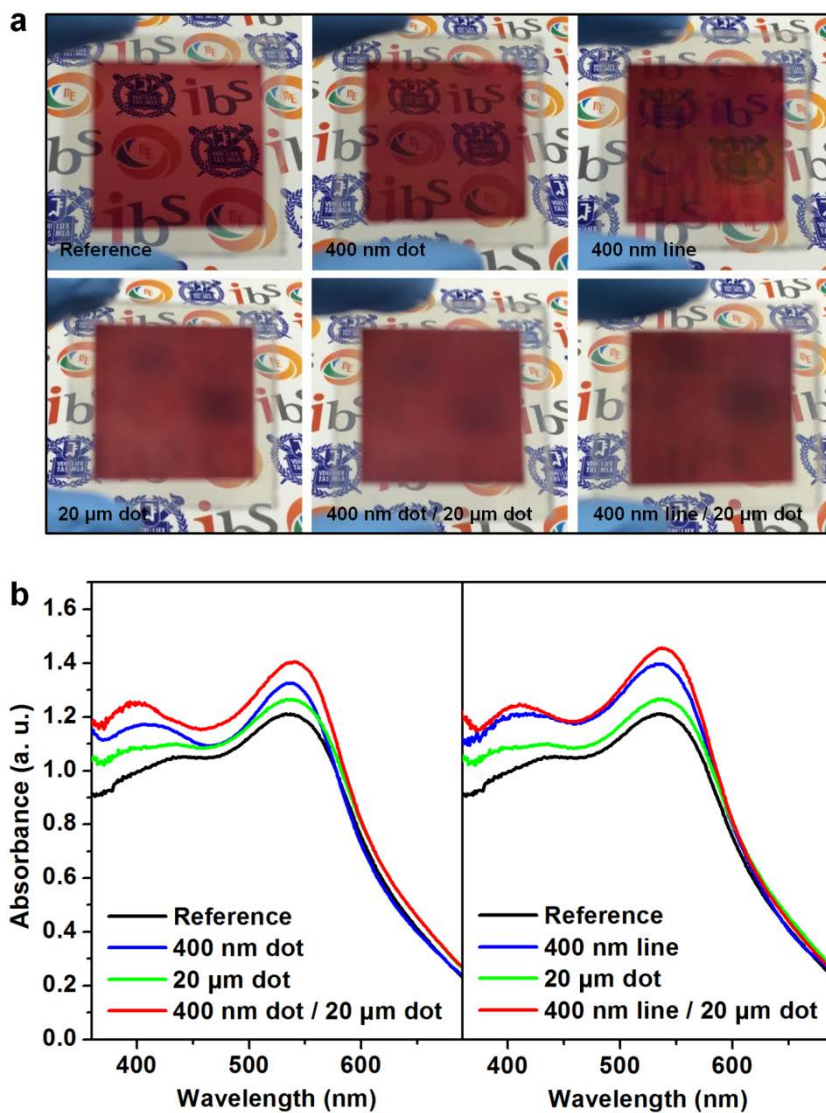


**Figure 2-8.** (a) Digital photographs of flat and patterned mp-TiO<sub>2</sub> with dye-sensitization. (b) Absorbance spectra of flat and patterned mp-TiO<sub>2</sub> with dye-sensitization.

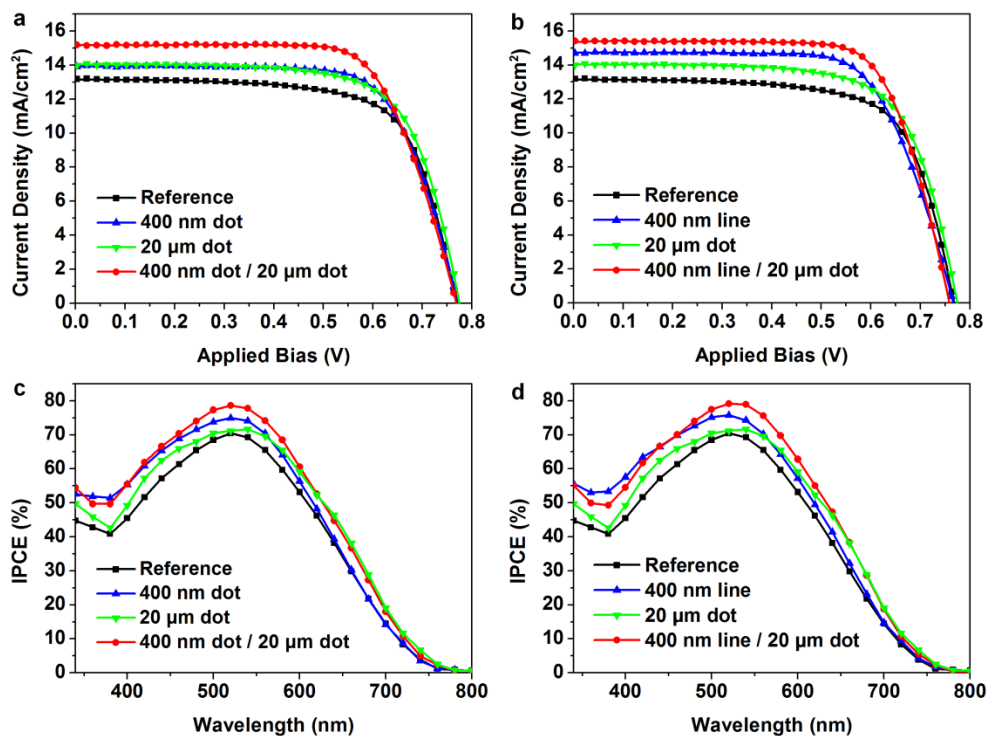


**Figure 2-9.** (a,b)  $J$ - $V$  characteristics and (c,d) IPCE spectra of DSSCs employing mp-TiO<sub>2</sub> with (a,c) flat, 400 nm dot, 20 μm dot, and 400 nm dot / 20 μm dot patterns and (b,d) flat, 400 nm line, 20 μm dot, and 400 nm line / 20 μm dot patterned structures.

Sample	$V_{oc}$ (V)	$J_{sc}$ (mA/cm <sup>2</sup> )	FF (%)	Efficiency (%)
Reference_1	0.768	13.2	69.9	7.08
Reference_2	0.762	13.3	71.8	7.28
Reference_3	0.777	12.6	71.4	7.00
400 nm dot_1	0.781	13.8	71.1	7.65
400 nm dot_2	0.765	14.0	70.5	7.53
400 nm dot_3	0.771	13.9	71.1	7.62
400 nm line_1	0.767	14.7	69.4	7.82
400 nm line_2	0.761	14.3	70.2	7.65
400 nm line_3	0.777	14.3	71.4	7.91
20 $\mu$ m dot_1	0.760	14.3	69.5	7.57
20 $\mu$ m dot_2	0.778	13.9	71.0	7.67
20 $\mu$ m dot_3	0.775	14.0	70.2	7.61
400 nm dot / 20 $\mu$ m dot_1	0.763	14.8	71.3	8.04
400 nm dot / 20 $\mu$ m dot_2	0.769	15.3	71.0	8.35
400 nm dot / 20 $\mu$ m dot_3	0.768	15.2	70.2	8.19
400 nm line / 20 $\mu$ m dot_1	0.759	15.4	72.2	8.45
400 nm line / 20 $\mu$ m dot_2	0.761	15.2	73.0	8.44
400 nm line / 20 $\mu$ m dot_3	0.759	15.1	71.6	8.21

**Table 2-2.** Detailed  $J$ - $V$  characteristics of the DSSCs employing flat or patterned mp-TiO<sub>2</sub> photoelectrodes.



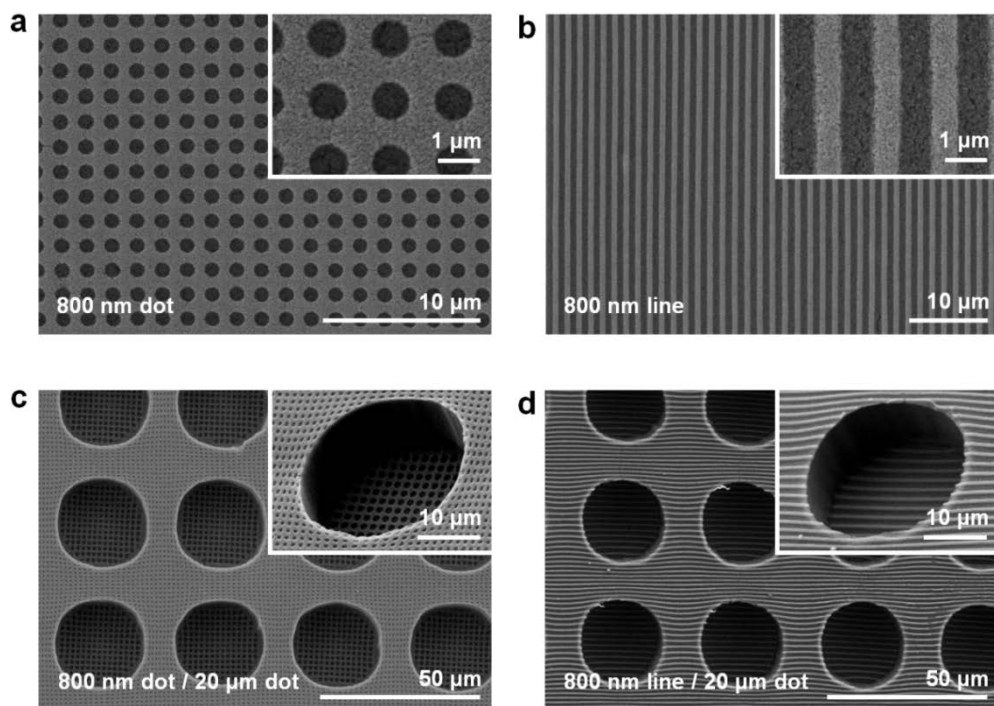


**Figure 2-10.** Top-view SEM images of (a) 800 nm dot, (b) 800 nm line, (c) 800 nm dot / 20 μm dot, and (d) 800 nm line / 20 μm dot patterned mp-TiO<sub>2</sub> films. The insets show enlarged images taken at higher magnifications.

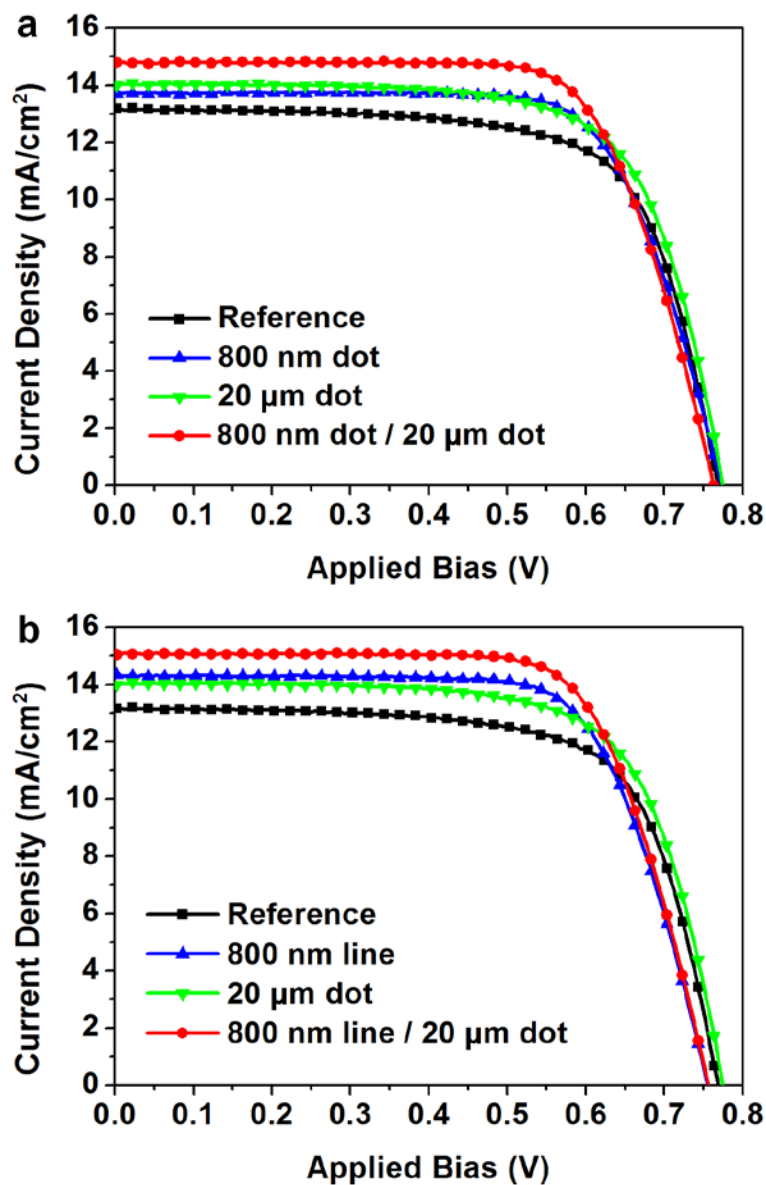


**Figure 2-11.** *J-V* characteristics of DSSCs employing (a) 800 nm dot and 800 nm dot / 20 μm dot patterned photoelectrodes and (b) 800 nm line and 800 nm line / 20 μm dot patterned mp-TiO<sub>2</sub> films. Results of flat (noted as Reference) and 20 μm dot patterned samples are displayed for comparisons.

Sample	Dye-loading ( $\times 10^{-7}$ mol/cm <sup>2</sup> )	$V_{oc}$ (V)	$J_{sc}$ (mA/cm <sup>2</sup> )	FF (%)	Efficiency (%)
800 nm dot	5.21	0.773	13.7	71.4	7.56
800 nm line	5.24	0.755	14.3	70.7	7.66
800 nm dot / 20 $\mu$ m dot	5.33	0.763	14.8	71.1	8.03
800 nm line / 20 $\mu$ m dot	5.27	0.756	15.0	71.2	8.09

**Table 2-3.** *J-V* characteristics of the DSSCs employing 800 nm dot, 800 nm line, 800 nm dot / 20  $\mu$ m dot, or 800 nm line / 20  $\mu$ m dot patterned mp-TiO<sub>2</sub> photoelectrodes.

## 2-4. Summary

In this study, we performed investigations on photonic application of multilevel multiscale patterned nano-oxide photoelectrodes for efficient light harvesting in mesoscopic solar cells. By controlling the degrees of polymerization at the surface of UV-curable PUA membrane, monolithic integration of free-standing PUA membranes with nano- and micro-scale architectures were enabled by LEGO<sup>®</sup>-like multiplex lithography. Based on this technique, multilevel multiscale patterned PDMS film was replicated, and its structure was imprinted on mesoporous TiO<sub>2</sub> film by soft-molding method. Formation of multilevel multiscale periodic structures on TiO<sub>2</sub> nanoparticle photoelectrodes were directly observed by electron microscope analyses, and characteristic optical properties of the multiscale patterned nano-oxide electrodes were verified by keen experiments and simulations. The z-axis integration of nano- and micro-patterns resulted in superposition of optical responses from nano- and micro-scale structures, enabling synergistic photon trapping within the photoelectrode by simultaneous diffraction grating and light scattering. Moreover, we confirmed the effectiveness of our approach by employing mp-TiO<sub>2</sub> with multilevel 400 nm / 20  $\mu$ m-scale patterns in DSSCs, where improved photovoltaic performances (up to 17.5% enhancement) induced by improved light harvesting were observed. Also, the validity of the multilevel multiscale patterning was cross-checked in 800 nm / 20  $\mu$ m dimension. Considering

that our approach provides a convenient, reliable, and industrially favorable (repeatable fabrication even in a large dimension) method for enhanced light harvesting in mesoscopic solar cells, our multilevel multiscale patterning strategy for superposition of optical properties is anticipated to bring substantial advances and insights to the photoelectrode designs and architectures for maximization of light harvesting.

# Chapter 3. Creep-assisted sequential imprinting method and its application to polymer electrolyte fuel cells

---

Published in ACS applied materials & interfaces, 2016, 8, 11459

## 3-1. Introduction

Multiscale hierarchical structures, the combined structures of micro- and nano-scale repeated pattern, have received great attention due to their structural advantages from individual micro- and nano-scale morphology simultaneously<sup>1-5</sup>. This synergetic effect of multiscale structures provides multifunctional properties to the raw material without any chemical treatment, which value of multiscale structures has been verified in various application fields such as microfluidics<sup>98-100</sup>, wetting and adhesion<sup>23, 101</sup>, optics<sup>102-104</sup>, electronics<sup>18-19</sup>, and energy systems<sup>20-21, 105</sup>. Therefore, many researchers have been trying to fabricate the multiscale structures covering large area in various processes. With conventional multiscale-patterning processes, however, introducing the nano-scale patterns on the top and bottom side of micro-patterns was only possible (not including the wall side of micro-pattern) and this means we could not fully utilize the multiscale structural effects so far<sup>42, 106-107</sup>. In this paper, we suggest a facile and simple multiscale patterning method called creep-assisted sequential imprinting to maximize the effects of multiscale structures. The creep behavior is the

phenomenon of a solid material to be deformed permanently even below the glass temperature under the long-term exposure to mechanical stresses<sup>108</sup>. By using this creep behavior, we sequentially imprinted nano- and micro-scale patterned-mold onto a Nafion membrane: the first step of thermal imprinting with nano patterns and the following step of creep-assisted imprinting with micro patterns. With taking advantages of thermal imprinting such as scalability and high throughput<sup>106, 109</sup>, creep-assisted imprinting technique enables multiple patterning on the same substrate, which leads to the fabrication of multiscale hierarchical structures. Using the replicating process of completed structures with soft lithography, furthermore, we showed the potential of feasible multiscale engineering without any sophisticated equipment and complex procedures.

In order to demonstrate the practical usage of our multiscale structures, we introduced a multiscale Nafion membrane to polymer electrolyte membrane fuel cells (PEMFCs) application. PEMFCs have been spotlighted as one of the leading candidate for future clean energy sources due to zero pollutant emission and high energy conversion efficiency and there have been extensive research efforts on this field during several decades<sup>110</sup>. However, there still remain several obstacles towards commercializing PEMFCs. Performance decay due to pore blocking with water at cathode catalyst layer is one of them<sup>111</sup>. Water is the product of oxygen reduction reaction in PEMFCs and this produced water needs to be

removed for maintaining the pathway of reactant oxygen<sup>112</sup>. To solving this problem, there have been several studies introducing void space in cathode catalyst layer<sup>113</sup>. With micro-patterns in multiscale patterned Nafion membrane, in this paper, regular empty space was formed in catalyst layer and showed positive effect on mass transfer in cathode side. Pt utilization has been another issue for commercialization of PEMFCs due to scarcity and high price of Pt. Therefore, various approaches for high Pt utilization such as using Pt nanoparticle supported on conducting materials<sup>114</sup>, alloying Pt with cheap metal species and modifying the catalyst layer structure in membrane electrolyte assembly (MEA)<sup>115</sup>. In this study, cathode catalyst layer was modified by using the multiscale patterned Nafion membrane. Due to the enlarged interfacial surface between catalyst layer and patterned Nafion membrane, increase of the electrochemical surface area (ESA), which is related to Pt utilization, was achieved. The combined effects of improved mass transport and increase of Pt utilization were verified by over 10 % performance enhancement of the MEA with our multiscale Nafion membrane.



## 3-2. Experimental

### *Fabrication of micro-and nano patterned molds*

The nano- and micro-sized hard polymer mold were prepared by casting and curing procedure on the 800-nm and 40- $\mu\text{m}$  hole-array-patterned silicon masters, which were fabricated by conventional photolithography, reactive ion etching (RIE) process and post-surface treatment with octafluorocyclobutane ( $\text{C}_4\text{F}_8$ ) gas. The UV-curable PUA prepolymer solution (PUA MINS 311 RM, Minuta Tech, Korea) was dropped onto the silicon master, and a 250- $\mu\text{m}$ -thick urethane-coated polyethylene terephthalate (PET) film was slightly placed on it as a supporting layer. After exposed to UV light (Fusion Cure System, Minuta Tech, Korea) for about 30 s, the resultant PUA polymer molds were detached from the silicon master<sup>116-117</sup>.

### *Preparation of the multiscale Nafion membrane and polymer mold*

The Nafion 212 membrane (Dupont, Wilmington, Delaware, United States) was sandwiched between the as-prepared nano-patterned hard PUA mold and glass substrate. Then, this assembly was hot-pressed under hydraulic pressure ( $\sim 1$  MPa) and temperature ( $\sim 120$  °C) for 5 min. After cooling down to the room temperature, the nano-patterned mold was removed. This nano-patterned Nafion membrane was placed between the micro-patterned hard polymer mold and the glass substrate again. Then,

creep-assisted imprinting was conducted under the transition temperature of Nafion ( $\sim 80\text{ }^{\circ}\text{C}$ ) with hydraulic pressure ( $\sim 3\text{ MPa}$ ) for 40 min. After cooling down, the multiscale Nafion membrane was attained by detaching the mold. Finally, the replication process of the multiscale hierarchical structure was performed by casting the PUA prepolymers onto the patterned membrane and curing with UV-light following the same procedure with repliacting the nano- and micro-patterned mold on silicon masters.

### ***MEA preparation***

The MEAs were prepared with the multiscale patterned Nafion membrane and a flat membrane without patterning. Each membrane was pre-treated by following steps. First, the membranes were boiled in 3% hydrogen peroxide solution and rinsed in deionized (DI) water. After this, they were put into 0.5 M  $\text{H}_2\text{SO}_4$  and washed again in DI water. All the steps were performed at  $80^{\circ}\text{C}$  for 1 h. The catalyst slurries were prepared by mixing 40 wt.% Pt/C (Johnson Matthey, London, United Kingdom), Nafion ionomer solution and 2-propanol (Sigma Aldrich, St. Louis, Missouri, United States) with sonication for 15 min. The prepared catalyst slurries were sprayed onto the both anode and cathode parts of the Nafion membranes with Pt loading of  $0.12\text{ mg/cm}^2$  on both sides. The Pt loadings were checked by comparing the weight difference before and after spraying Pt/C catalyst ink on the PET film. The completed catalyst-coated

membranes were dried at room temperature for 12 h and placed between the anode and cathode GDLs (SGL Carbon, Wiesbaden, Germany) without a hot press process. The active geometric areas of the MEAs were 5.0 cm<sup>2</sup>.

### ***Electrochemical characterization***

Polarization curves were measured by the current sweep method at a 10 mA cm<sup>-2</sup> s<sup>-1</sup> rate using the PEMFC Test System (CNL Korea, Seoul, Korea). Cell temperature was maintained at 80 °C during the polarization test. Fully humidified H<sub>2</sub> (150 mL/min) to the anode and Air (800mL/ min) or O<sub>2</sub> (200mL/ min) to the cathode were supplied with/without back pressure of 150 kPa. EIS (IM6, Zahner) of the MEAs was measured at 0.5V with an amplitude of 10 mV. The measurement was conducted in a frequency range from 0.1 Hz to 10 kHz and other experimental conditions such as temperature and gas humidification were applied to the same as polarization test. The ZView program (Scribner Associates, Inc.) was utilized for fitting the EIS data. CV scans were obtained at 100 mV/s rate between 0.05 V and 1.0 V to obtain the EAS of the prepared cathode catalyst layers at 30 °C cell temperature. During the CV scans, fully humidified H<sub>2</sub> (50 mL/min) and N<sub>2</sub> (200mL/ min) were supplied to the anode and cathode, respectively.

### 3-3. Results and Discussion

#### 3-3-1. Creep-assisted sequential imprinting method for constructing multiscale multilevel structures

**Figure 3-1a-1c** demonstrates the fabricating procedure of the multiscale polymer mold via creep-assisted sequential imprinting. The procedure consists of three main steps: (a) first-stamping step on the Nafion membrane with nano-patterned hard polyurethane-acrylate mold (h-PUA) through thermal imprinting (b) second-stamping step with micro-patterned h-PUA mold through creep-assisted imprinting (c) replicating step through casting and UV curing of h-PUA on the patterned Nafion membrane (See the details in experimental section). **Figure 3-1d-1f** shows digital camera images of the fabricated structures after each step. The nano-patterned film showed iridescent structural coloration due to its repeated nano-pattern array (**Figure 3-1d**) and the multiscale-patterned film showed relatively opaque area due to the micro-patterns overlaid on the nano-patterns (**Figure 3-1e**). The replicated mold showed similar optical coloration to multiscale-patterned film (**Figure 3-1f**). All the patterned figures are over 3.5 cm x 3.5 cm size. **Figure 3-2a-2b** is representative scanning electron microscope (SEM) images of the nano- and multiscale-patterned Nafion membrane, respectively. It shows the nano-sized hole array were patterned on the Nafion membrane without any defect site and these nano-patterns well

remained after the second stamping procedure using the creep behavior of Nafion. Even on the side surface of micro-sized hole-patterns, furthermore, the nano-hole patterns clearly remained. During the creep-assisted imprinting of the micropatterns, proper stamping pressure ( $\sim 3$  MPa), time ( $\sim 40$  min), and transition temperature ( $T_t$ ) of Nafion ( $\sim 80$  °C) are important parameters to get sufficient creep strain as well as high fidelity of multiscale structures. As temperature increases over  $T_t$  and approaches to glass temperature ( $T_g$ ) of Nafion ( $\sim 120$  °C), the patterned nanostructures are getting flattened because Nafion behaves as a viscous liquid on the micropatterned mold. This phenomenon was confirmed from the SEM images of multiscale patterned Nafion membrane under high temperature condition (**Figure 3-2c-2d**). With these results, we were convinced that the creep behavior is essential for multiscale patterning with the sequential imprinting method. As shown in **Figure 3-2e**, we successfully fabricated multiscale-patterned h-PUA mold with the replicating process using the resultant patterned Nafion membrane. Because h-PUA has a capability of replication of sub-100 nm pattern and a high modulus ( $> 320$  MPa), replicated PET/h-PUA mold could perfectly have inverse structures of the patterned Nafion membrane. The high modulus and flexibility of h-PUA mold enable physical patterning without using hard mold (e.g. silicon or metal) and roll-to-roll process for high-throughput production<sup>118</sup>. We found that micro-patterns in the resultant patterned film and the h-PUA mold have

cone-shaped, slanted side surface (**Figure 3-2b, 3-2e**). These morphological characteristics were derived from instantaneous creep recovery effect during the second stamping process and the relevant schematic illustrations and simulation results are shown in **Figure 3-6** for better understanding of creep response<sup>108</sup>. Additionally, we confirmed that various multiscale structures could be readily produced by multiple combinations of diverse patterns (**Figure 3-3 - 3-5**). This means that creep-assisted sequential imprinting is a user-friendly and powerful method to get the multiscale structures.

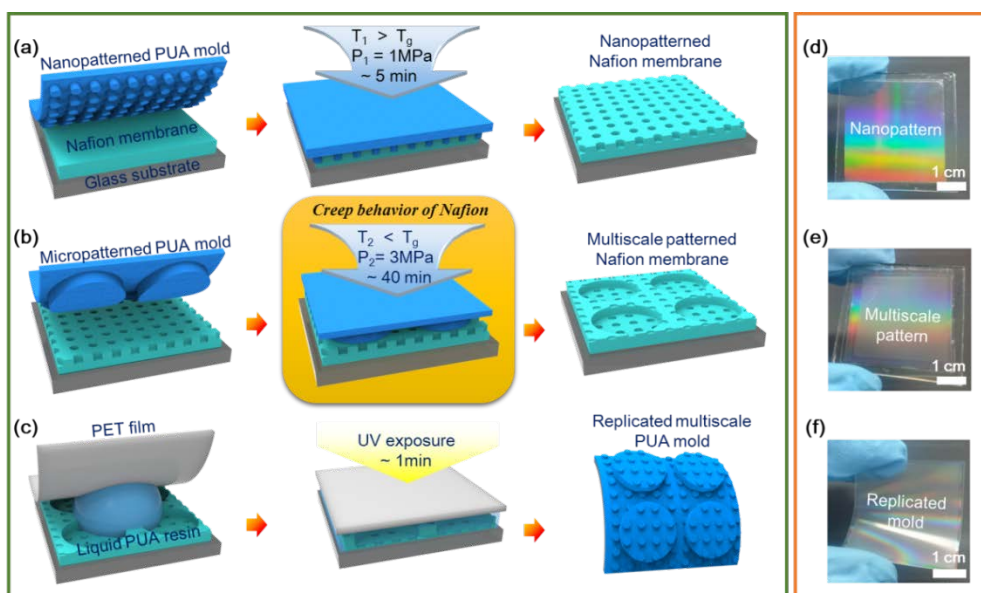


**Figure 3-1.** Schematic illustration for fabrication process of multiscale Nafion membrane with sequential imprinting. (a) Imprinting nano-patterns on bare Nafion membrane under the above glass temperature condition ( $T_g$ ). (b) Sequential-imprinting micro-patterns on nano-patterned Nafion membrane under the below glass temperature condition ( $T_g$ ). (c) Replicating the multiscale-patterns with PUA from the multiscale Nafion membrane. (d-f) The corresponding digital camera images for nano-patterned Nafion membrane (d), multiscale Nafion membrane (e), and replicated multiscale PUA mold (f).

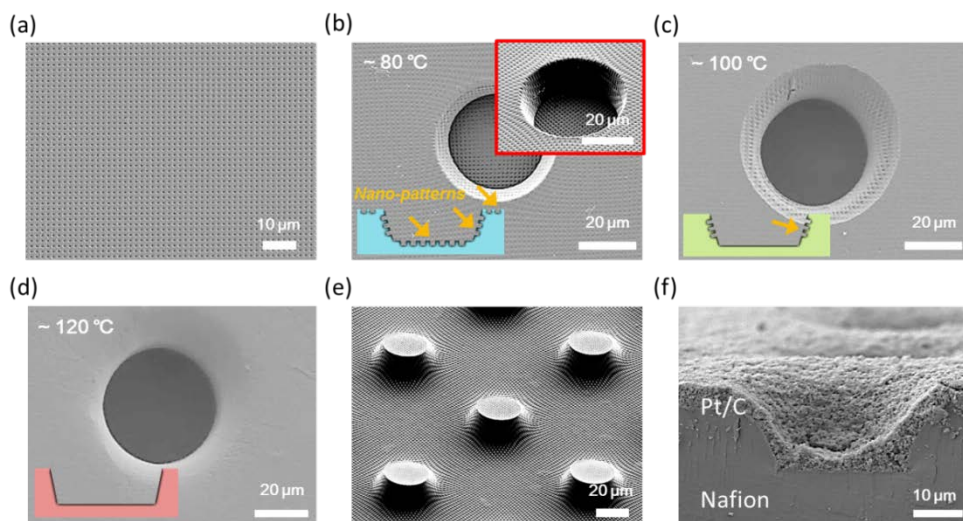
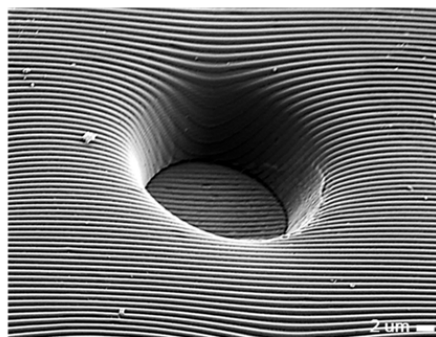
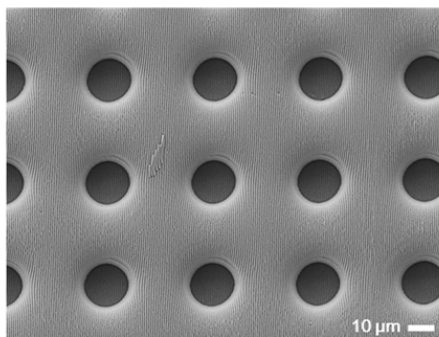


**Figure 3-2.** (a) The SEM image for nano-patterned Nafion membrane. (b-d) The SEM images for the obtained structures after sequential-imprinting with the stamping temperature variation of second imprinting process. (b)  $\sim 80^\circ\text{C}$ , (c)  $\sim 100^\circ\text{C}$ , and (d)  $\sim 120^\circ\text{C}$ . (e) The SEM image for replicated multiscale PUA mold. (f) The cross-sectional SEM image for the catalyst layer on multiscale Nafion membrane.



(-) Nafion



(+) PUA 311 mold

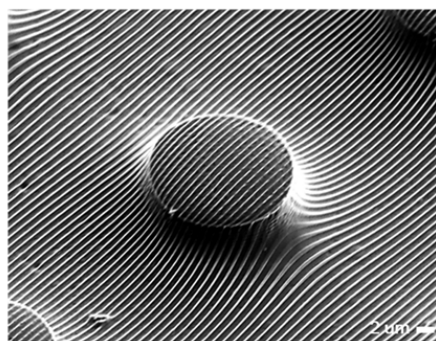
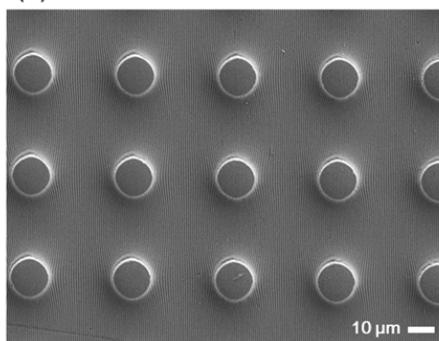
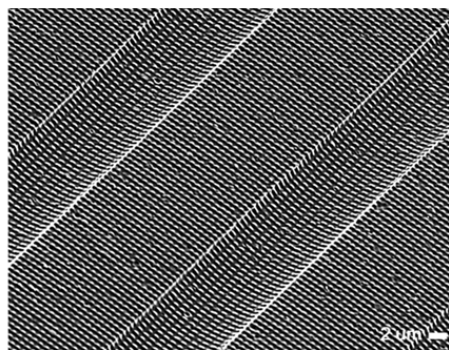
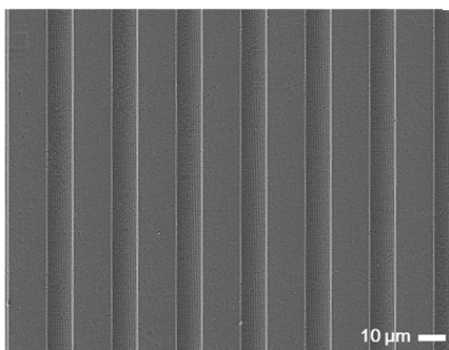


**Figure 3-3.** Fabricated multiscale Nafion membrane and PUA 311 mold with combination of the micro pillar-patterns and the nano line-patterns

(-) Nafion



(+) PUA 311 mold

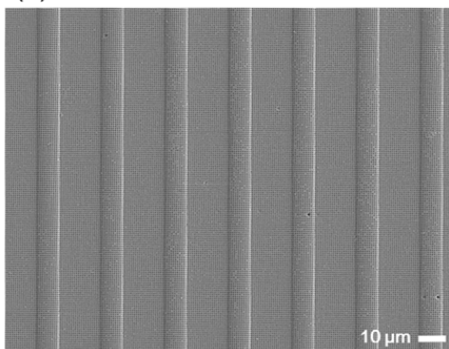
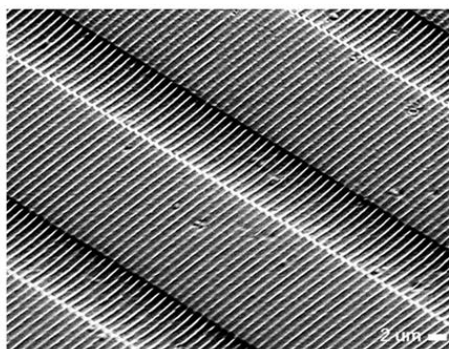
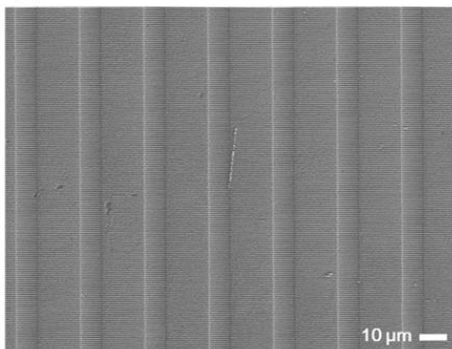


**Figure 3-4.** Fabricated multiscale Nafion membrane and PUA 311 mold with combination of the micro line-patterns and the nano dot-patterns

(-) Nafion



(+) PUA 311 mold

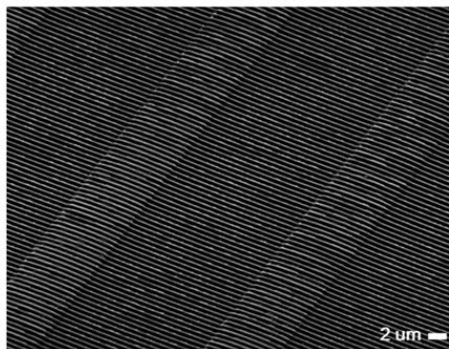
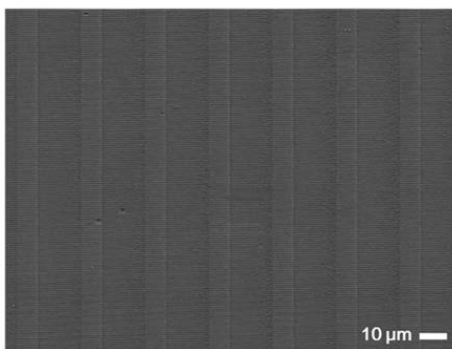


**Figure 3-5.** Fabricated multiscale Nafion membrane and PUA 311 mold with combination of the micro line-patterns and the nano line-patterns

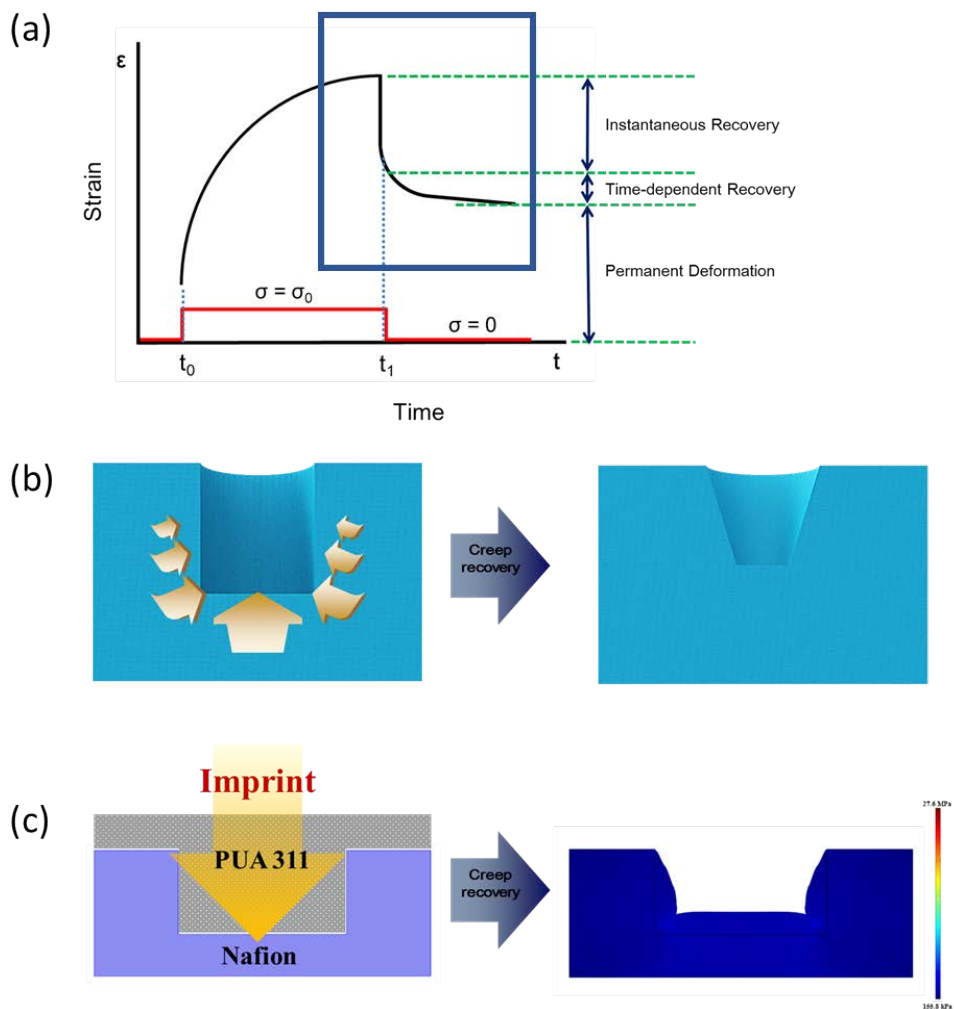


**Figure 3-6.** Schematic illustrations for creep response of Nafion membrane (a), instantaneous creep recovery effect during the stamping process (b) and the corresponding simulation results (c)

### **3-3-2. Enhanced performance of polymer electrolyte fuel cell with Multiscale multilevel designed membrane**

For an evaluation of the advantages from creep-assisted multiscale engineering in PEMFCs, multiscale patterned Nafion membrane was incorporated in MEA as the polymer electrolyte membrane. A catalyst layer with commercial Pt/C catalyst was spray-coated on both anode and cathode side (Pt loading:  $0.12 \text{ mg cm}^{-2}$ ). The multiscale-patterned side used as cathode because most of the performance degradation occurred at cathode due to slow oxygen reduction reaction (ORR)<sup>119-120</sup> and water flooding during operation<sup>111</sup>. The active geometric area of MEA was set to  $5 \text{ cm}^2$  and the catalyst layer was formed with following the patterned membrane surface as shown in the cross-sectional image of the catalyst layer (**Figure 3-2f**). **Figure 3-7a-7b** shows polarization curves (I-V) of the single cell performance of the conventional MEA and the MEA with the multiscale Nafion membrane in a fully humidified condition of  $\text{H}_2/\text{air}$  and  $\text{H}_2/\text{O}_2$  under ambient pressure, respectively. The MEA with multiscale-patterned membrane exhibited ~10.7 % and ~8.8 % improved cell performance in maximum power density compared to a conventional one. And the MEA with the multiscale membrane showed higher performance than that of the MEA with micro/nano single-patterned membranes (**Figure 3-8**). When following the MEA test condition of the US Department of Energy ( $\text{H}_2/\text{air}$ ,  $80^\circ\text{C}$ , 150 kPa outlet pressure)<sup>121</sup>, the MEA with the multiscale membrane

yielded the maximum power density of  $1.04 \text{ W cm}^{-2}$  (**Figure 3-7c**). In order to compare the actual efficiency loss in condition of reduced oxygen partial pressure, oxygen gain was calculated by the following equation<sup>122</sup>,

$$\text{oxygen gain}(\Delta V) = V(H_2/O_2) - V(H_2/\text{air}) \quad (1)$$

The oxygen gain value of MEA with patterned Nafion membrane was smaller than that of MEA with un-patterned one and the difference was getting bigger as the current density increased (**Figure 3-7d**). This indicates the MEA with patterned membrane enhanced mass transport compared to conventional one.

To elucidate the origin of the improved performance, electrochemical impedance spectroscopy (EIS) analysis was conducted<sup>123</sup>. As shown in **Figure 3-9b** of Nyquist plot measured at 0.5 V, the mass transport resistance of MEA with the multiscale membrane was significantly decreased. To quantitatively explain this, the EIS data were fitted based on the equivalent circuit of **Figure 3-9a** and MEA with the multiscale membrane showed ~50.8 % lower value in Warburg impedance, which represents the mass transport was improved compared to the conventional one. This results corresponded with aforementioned the lower oxygen gain values of MEA with the multiscale membrane in **Figure 3-7d**, which means the effective mass transfer in the cathode side<sup>122</sup>. For the theoretical analysis

of this mass transport issue, we propose a simple theoretical model here. The catalyst layer surface has micro-sized cone-shaped morphology, which was resulted from instantaneous creep recovery effect during the creep-assisted micro-patterning process as shown in **Figure 3-2f**. In order to estimate the direction of net force to water droplet within the patterned catalyst layer, we hypothesize the competing forces of Laplace pressure onto a water droplet; lower-side pressure difference  $\Delta P_1$  and upper-side pressure difference  $\Delta P_2$  at each interface between water droplet and air (**Figure 3-9c**). The  $\Delta P_1$  and  $\Delta P_2$  can be calculated from the following Laplace-Young equation<sup>124-125</sup>.

$$\Delta P = P_{\text{inside}} - P_{\text{outside}} = \frac{2\gamma}{R} \quad (2)$$

In above equation,  $\gamma$  is the surface tension and  $R_1$ ,  $R_2$  are the radii of curvature of lower-side and upper-side of the water droplet, respectively. Here, both  $R_1$  and  $R_2$  have positive values because the surface of Pt/C catalyst is hydrophobic (**Figure 3-10**) and  $R_1$  is smaller than  $R_2$  due to the cone-shaped morphology of catalyst layer (**Figure 3-9c**). Therefore, the driving-force direction of the water droplet is upward ( $\Delta P_1 > \Delta P_2$ )<sup>4, 125</sup>, which means generated water is effectively removed from the catalyst layer. This result is in accordance with enhanced mass transport in the MEA with the multiscale membrane.

In addition, cyclic voltammetry (CV) analysis was conducted to verify the effect of extended interfacial area between the patterned membrane and the catalyst layer<sup>126-127</sup>. **Figure 3-11a** shows CV curves for cathode part in single cell of the conventional MEA and MEA with multiscale membrane. From the hydrogen adsorption/desorption area in each CV curve, the ESA were calculated by following equation.

$$ESA (m^2 g^{-1}) = \frac{q_{Pt}}{\Gamma \cdot L} \quad (3)$$

In above equation,  $q_{Pt}$  is hydrogen absorption (or desorption) charge density, which can be obtained from the CV curves, and  $\Gamma$  is the charge required to reduce a monolayer of protons on Pt ( $\Gamma=210 \mu C cm^{-2}$ ).  $L$  is the Pt loading in the electrode, which was  $0.12 mg_{Pt} cm^{-2}$  in this study<sup>19</sup>. The ESA of MEA with multiscale membrane was calculated to be  $68.07 m^2/g$ , which is  $\sim 7.38\%$  larger than that of the conventional one ( $63.39 m^2/g$ ), indicating that the MEA with the patterned membrane has higher Pt utilization and has more available active sites compared to the reference MEA. This enhancement came from the enlarged interfacial surface area between multiscale patterned membrane and electrocatalyst layer in MEA. **Figure 3-11b** shows the increase of surface area due to each patterning compared to un-patterned membrane. The calculated surface area of multiscale membrane is about  $\sim 1.7$  fold than that of the flat membrane. However, the increase of ESA was



only 7.38%. This discrepancy might be attributed to the fact that most of the ESA came from the Nafion binder/Pt particle interface in porous catalyst layer.

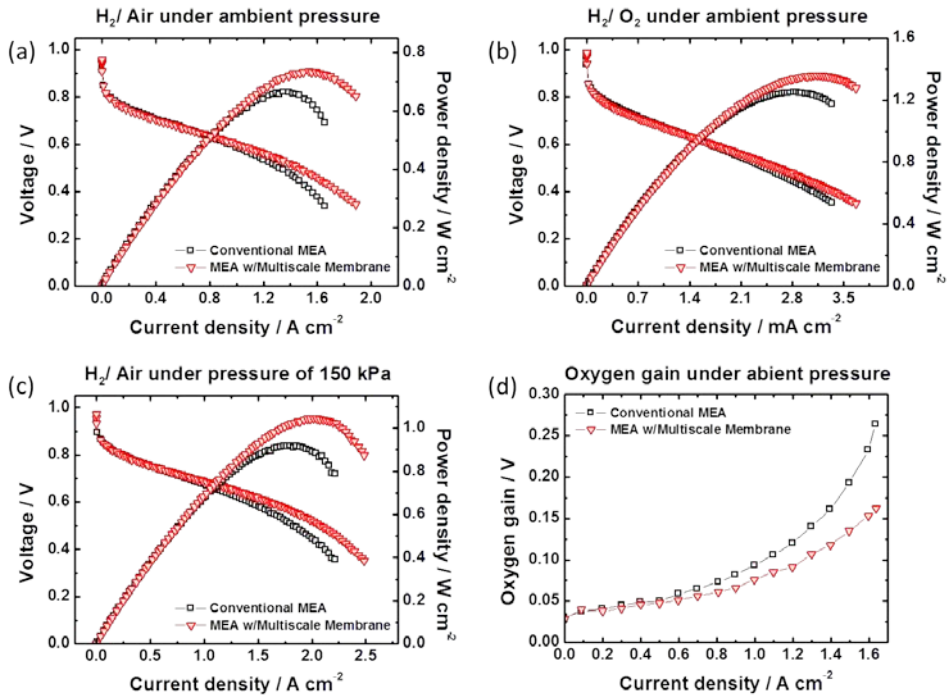


**Figure 3-7.** Polarization curves of conventional membrane electrode assembly (MEA) and the MEA with the multiscale Nafion membrane under the conditions of H<sub>2</sub>/Air (a) H<sub>2</sub>/O<sub>2</sub> (b) under ambient pressure and H<sub>2</sub>/Air under pressure of 150 kPa (c). (d) The oxygen gain obtained under ambient pressure.

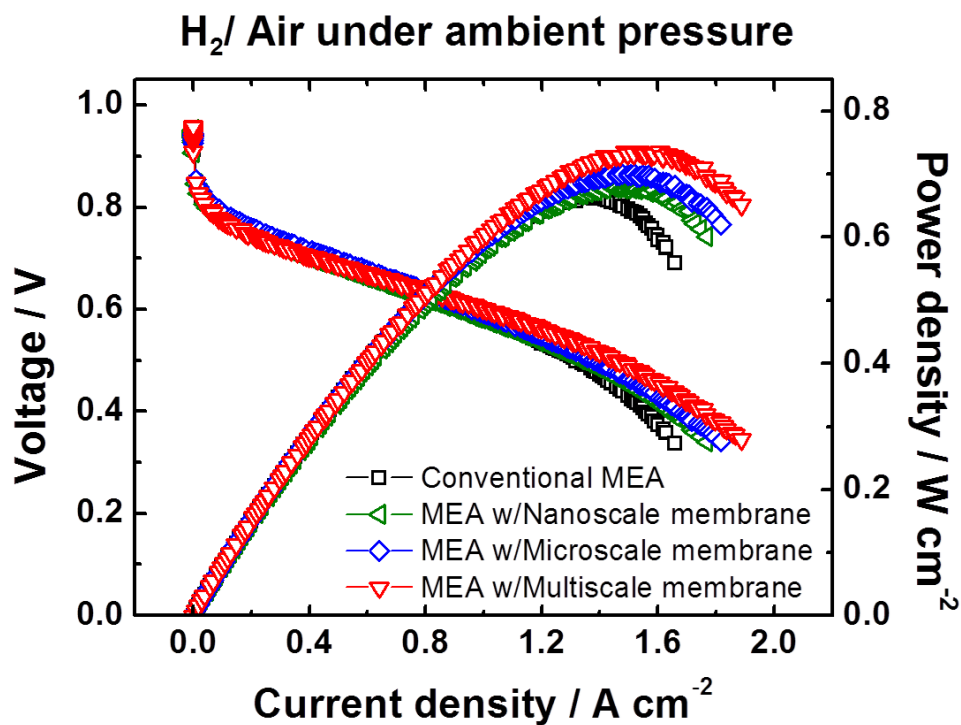


**Figure 3-8.** Single-cell performance of the MEAs with various pattern dimensions in the conditions of H<sub>2</sub>/Air under ambient pressure

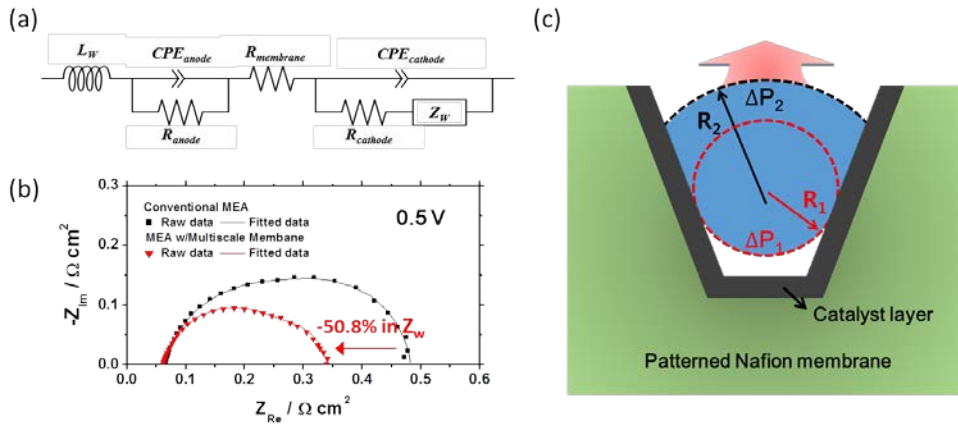


**Figure 3-9.** (a) Equivalent circuit of the PEMFC single cell ( $L_W$  = inductance of the electric wire,  $R_{membrane}$  = internal membrane resistance,  $R_{cathode (anode)}$  = charge transfer resistance of the cathode (anode),  $CPE_{cathode (anode)}$  = constant phase element of the cathode (anode) and  $Z_W$  = Warburg impedance). (b) Electrochemical impedance spectroscopy (EIS) of a conventional MEA and MEA with the multiscale Nafion membrane at 0.5 V. (c) Schematic illustration for the force balancing of a water droplet at a cone-shaped void space in a catalyst layer.

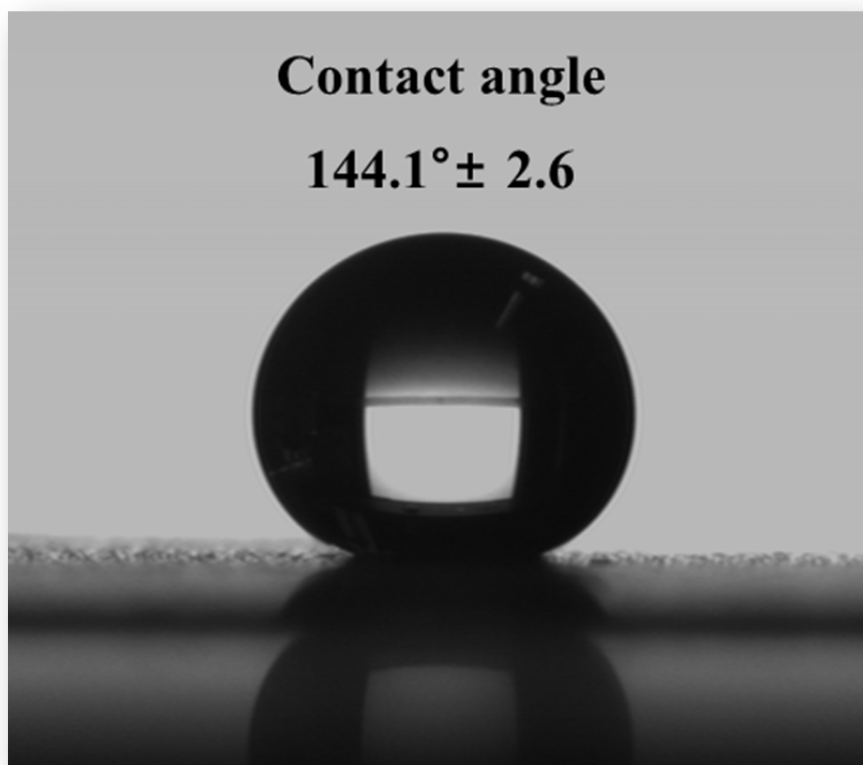


**Figure 3-10.** The contact angle of a DI water droplet on the cathode catalyst layer

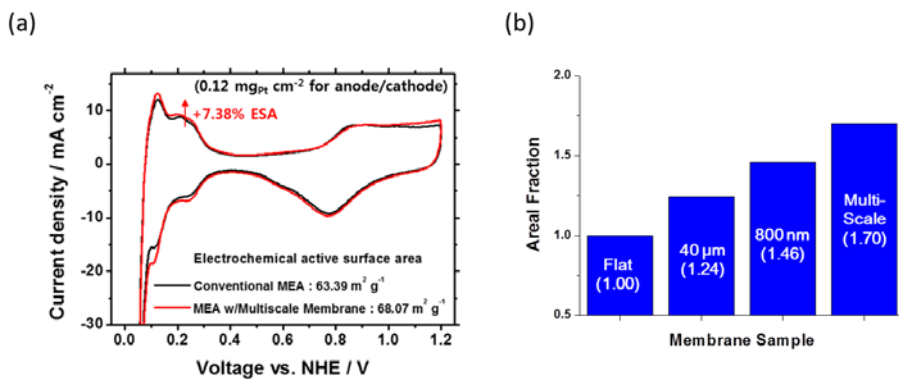


**Figure 3-11.** (a) Cyclic voltammogram (CV) of the cathode catalyst layers of a conventional MEA and MEA with the multiscale Nafion membrane. (b) Increased surface area ratio compared to flat surface with various patterned surfaces.

### **3-4. Summary**

We reported a facile and simple multiscale patterning method, creep assisted sequential imprinting. We successfully fabricated the patterned Nafion membrane using our novel method and verified the multiscale patterns covering the whole surface without defects. With this patterned Nafion, the MEA showed over 10% improved performance. We confirmed this improvement originated from the combined effect of the improved water removal from the cone-shaped void space between the catalyst layer and the GDL and the increase of ESA from extended interfacial surface area between the Nafion membrane and the catalyst layer. We believe that the technique reported in this study will provide a practically feasible route to fabricate multiscale structures over large areas and can be employed in optimization of various types of electrochemical devices such as capacitors, batteries, and water-splitting devices.

## Chapter 4. Interface engineering for high-performance direct methanol fuel Cells

---

Published in Nano energy, 2017, 43, 149-158

### 4-1. Introduction

The direct methanol fuel cell (DMFC) has received significant attention as an ideal power source that could satisfy the increasing demand for portable electronics owing to its high energy density, environmental friendliness, as well as the ease of handling methanol<sup>128-131</sup>. Nonetheless, to commercialize DMFCs, some obstacles, such as high catalyst loadings and large system volumes, need to be overcome<sup>132-133</sup>. Among DMFC components, the membrane electrode assembly (MEA) is the most important. As a core component of fuel cells, the MEA generates electricity by electrochemical oxidation of methanol and reduction of oxygen at the anode and the cathode, respectively. Since the design of the fuel container and number of stacks are determined by the power and energy generated from the MEA, the fabrication of high-performance MEAs is a key to reducing the volume of DMFCs and the catalyst loading amounts<sup>132</sup>.

In DMFCs, performance loss mainly results from two factors: (a) formation of a mixed potential at the cathode due to methanol crossover through an electrolyte membrane<sup>133-134</sup> and (b) slow kinetics of methanol



oxidation at the anode<sup>133, 135-136</sup>. To resolve the issue of methanol crossover, many approaches have been adopted, such as developing organic/inorganic composite membranes<sup>37-38</sup> and embedding a methanol barrier layer into the membrane surface<sup>39-40</sup>. However, achieving low methanol crossover and high proton conductivity simultaneously has been challenging owing to methanol permeation resulting from the electro-osmotic drag caused by hydrated protons and diffusion. To resolve other issues, namely low Pt utilization and the slow kinetic behavior of the MEA, many studies have examined the incorporation of a patterned membrane into fuel cell devices using a simple one-dimensional pattern<sup>137-138</sup>. However, an enlarged interfacial area between the anode and the electrolyte membrane results in higher methanol crossover<sup>132</sup>, which implies that a trade-off would exist between low methanol crossover and high interfacial area. To solve both these problems simultaneously and thus obtain a high-performance DMFC, we fabricated a MEA with a multiscale patterned membrane and incorporated a guided gold cracked layer into the MEA. Using the creep-assisted sequential imprinting method<sup>33</sup>, we easily fabricated a multiscale hierarchical-structured membrane with a high surface area. The MEA with the multiscale patterned membrane showed improved performance compared with that of the reference because mass transport was enhanced by the thinned electrode and the effective utilization of catalytic active sites. Moreover, the electrochemically inactive thin gold layer was expected to act

as a physical barrier for methanol crossover, with cracks introduced to provide multiple proton pathways. In addition to reduced methanol crossover, the multiscale MEA with guided gold cracked layer achieved an ohmic resistance comparable to that of the reference MEA, and the device performance was significantly enhanced by 30.5% compared with that of the reference.

## 4-2. Experimental

### *Fabrication of the prism and nano-patterned polymer molds*

The prism array master mold with a 10  $\mu\text{m}$  pitch size (P-10) was prepared through mechanical machining. First, a nickel electroplated stainless steel sample was mechanically machined with a diamond-cutting tool with a specific angle ( $\sim 45^\circ$ )<sup>34</sup>. The height of the carved patterns was determined by the cutting depth of the diamond tool. Then, a UV-curable prepolymer resin (PUA MINS 311 RM, Minuta Tech) was poured on the prepared master, and a 300  $\mu\text{m}$  thick polyethylene terephthalate (PET) film was placed onto it as a supporting backbone. After exposed to UV light (Fusion Cure System, Minuta Tech) for about 30 s, the resultant PUA polymer molds were detached from the prism mold. In addition, a polymeric pillar mold with a diameter of 800 nm was fabricated using an 800 nm hole-array-patterned silicon master mold and the same UV curing method. Finally, the polymer molds were subjected to post-surface treatment with octafluorocyclobutane ( $\text{C}_4\text{F}_8$ ) gas to reduce the surface energy of the pattern and achieve high chemical stability.

### *Preparation of the multiscale prism mold*

The multiscale prism mold was fabricated by the creep-assisted sequential imprinting method<sup>33</sup>. First, a Nafion 115 membrane (DuPont) was

placed between the as-prepared 800 nm pillar (+)-patterned PUA mold and the glass substrate. Next, this assembly was hot-pressed under constant pressure ( $\sim 0.8$  MPa) at the glass temperature of Nafion ( $\sim 130$  °C) for 10 min. After cooling to ambient temperature, the 800 nm pillar (+)-patterned PUA mold was detached from the Nafion membrane. The resulting 800 nm hole (-)-patterned Nafion membrane was placed between the as-prepared P-10-patterned PUA mold and the glass substrate again. Then, this assembly was hot-pressed at the transition temperature of Nafion ( $\sim 85$  °C) under constant pressure ( $\sim 4$  MPa) for 1 h. Under these conditions, Nafion showed viscoelastic creep behavior. Following the two imprinting processes, the multiscale prism-patterned mold with a 10  $\mu\text{m}$  pitch and an 800 nm pillar (MP-10) was fabricated by casting and curing polydimethylsiloxane (Sylgard 184) on top of the sequentially imprinted membrane.

### **Preparation of the multiscale patterned membrane and guided metal cracked layer**

The Nafion 115 membrane was uniformly placed between the as-prepared PUA mold (P-10 or MP-10) and the glass substrate. Then, the assembly was imprinted under hydraulic pressure ( $\sim 1.5$  MPa) at a temperature of  $\sim 130$  °C for 10 min. After cooling to room temperature, the patterned Nafion 115 membrane was peeled off the PUA mold. Next, the membrane was cleaned with a 3 wt.% hydrogen peroxide solution and reprotonated using a 0.5 M sulfuric acid solution for 1 h at 80 °C. Then, a

gold film with a thickness of ~40 nm was deposited on the prepared membrane using a vacuum thermal evaporator (Selcos, South). Next, the membrane with the thin gold film was stretched in the direction perpendicular to the prism using a universal material testing machine (3342 UTM, Instron Corp.) by applying a strain of about 0.25.

### ***MEA preparation***

MEAs with an active area of 5 cm<sup>2</sup> were fabricated by the catalyst-coated membrane (CCM) method. PtRu black (HiSPEC 6000, Johnson Matthey Corp.) and Pt black (HiSPEC 1000, Johnson Matthey Corp.) were used as the anode and cathode catalysts, respectively. Homogeneous catalyst inks were prepared by dispersing each catalyst over Nafion ionomer (5 wt.% Nafion solution, DuPont) in an aqueous solution of isopropyl alcohol (IPA, Sigma Aldrich) (volumetric ratio of distilled water:IPA = 10:50), followed by ultrasonic treatment more than 10 min. The prepared catalyst inks were directly sprayed onto the prepared or bare Nafion membranes to fabricate CCMs. The catalyst loadings for the anode and the cathode were fixed at 2.0 mg cm<sup>-2</sup> and 1.0 mg cm<sup>-2</sup>, respectively. These CCMs were dried at ~30 °C for more than 12 h. Then, the CCMs were sandwiched between the anode gas diffusion layer (TGP-H-060, Toray) and cathode gas diffusion layer (JNT30-A3, JNTG) without a hot-pressing process.

### ***Physical characterization***

Surface images of various samples used in this study were obtained using field emission scanning electron microscopy (FE-SEM, AURIGA, Carl Zeiss) and cross-sectional images were investigated utilizing focused ion beam-assisted SEM (FIB-SEM, AURIGA, Carl Zeiss), which uses an energy-selective backscattered detector to distinguish each layer more clearly. In addition, the topography of each sample was examined using atomic force microscopy (AFM, NX-10, Park Systems) in noncontact mode with a silicon tip.

### ***Electrochemical characterization***

The prepared MEA was inserted between two graphite plates with a one-channel, serpentine-type flow field. The single cell was assembled by applying torque to each screw of the single cell ( $\sim 6.4$  N m) and then connected to a DMFC station (CNL Energy). Before measuring the DMFC performance of the prepared MEA, the single cell was operated under hydrogen fuel cell conditions. Fully humidified hydrogen and oxygen without back pressure were fed to the anode and the cathode at flow rates of  $300 \text{ mL min}^{-1}$  and  $200 \text{ mL min}^{-1}$ , respectively. The temperature of the cell was maintained at  $70^\circ\text{C}$ . The single cell was operated under these conditions until a stabilized cell voltage was achieved at the correspondent discharging current with a scan rate of  $36 \text{ mA s}^{-1}$ . To estimate the DMFC

performance of the prepared MEA, methanol solutions with different concentrations (1.5 M and 3.0 M) were fed to the anode at a flow rate of 1.5 mmol min<sup>-1</sup>. Nonhumidified air was supplied to the cathode at a flow rate of 200 mL min<sup>-1</sup>. The single cell polarization curve was measured at a cell temperature of 70 °C by the current sweep method at a scan rate of 18 mA s<sup>-1</sup>. Electrochemical impedance spectroscopy (EIS, Zennium, Zahner) was conducted at 0.4 V with an amplitude of 10 mV over the frequency range of 0.1 Hz to 100 kHz to characterize the electrochemical properties of the MEA. EIS was conducted under the same conditions as those for the single cell operation. To demonstrate the effect of membrane patterning on the anode performance, an anode polarization test was performed at 70 °C by supplying fully humidified hydrogen to the cathode at a flow rate of 200 mL min<sup>-1</sup> instead of non-humidified air. The cathode with hydrogen flowing around it could be considered a dynamic hydrogen electrode (DHE); therefore, anode polarization curves and EIS measurements for the cell were obtained using the cathode as the reference electrode (RE) and the counter electrode (CE)<sup>139</sup> and the anode as the working electrode (WE). To analyze the relative amount of methanol crossover, linear sweep voltammetry (LSV) was conducted at 70 °C by supplying a methanol solution (1.5 M or 3.0 M) and fully humidified nitrogen gas to the anode and the cathode, respectively. Under these conditions, the cathode was used as the WE and the anode was used as the CE. The discharge potential range was 0.00–0.75 V vs. the

anode at a scan rate of  $2 \text{ mV s}^{-1}$ . Cyclic voltammetry (CV) was carried out to analyze the effect of membrane patterning on the electrochemical active surface area (ECSA) of the anode catalyst layer. Fully humidified hydrogen was fed to the cathode (Pt black electrode), serving as the RE and the CE, and fully humidified nitrogen was supplied to the anode (PtRu black electrode), serving as the WE. This measurement was conducted at a cell temperature of  $30 \text{ }^{\circ}\text{C}$  and the voltage sweep range was  $0.05\text{--}1.20 \text{ V}$  at a scan rate of  $100 \text{ mV s}^{-1}$ .



## 4-3. Results and Discussion

### 4-3-1. Fabrication of multiscale patterned membranes

**Figure 4-1** shows a schematic illustration of the fabrication process for the multiscale prism-patterned Nafion membrane. The multiscale prism mold was fabricated based on the creep-assisted sequential imprinting method<sup>33</sup>, which our group has previously developed for constructing multiscale structures. The method consists of successive thermal imprinting processes using thermo-plastic films with varying imprint conditions. In this process, the first imprinting step was performed above the glass temperature ( $T_g$ ) of the polymer film. When the imprint temperature is higher than the  $T_g$  of the polymer, the polymer behaves as a viscous liquid and can easily flow into the openings of the mold<sup>109</sup>. The second imprinting step was then carried out based on the viscoelastic creep behavior of the polymer below the  $T_g$ . This creep phenomenon denotes a permanent deformation of the polymer material, even below the  $T_g$ , when the material is exposed to long-term mechanical stresses (details are provided in section 2.2)<sup>33</sup>. Using this creep-assisted sequential imprinting method, we could easily fabricate multiscale hierarchical structures with the advantages of scalability and high throughput. SEM images of the fabricated multiscale prism mold are shown in **Figure 4-2**. Next, using the as-prepared P-10 and MP-10 molds, we fabricated patterned Nafion membranes by the thermal imprinting method.

**Figure 4-3** shows the SEM images of the pristine, P-10-, and MP-10-patterned Nafion 115 membranes, respectively. Repeated valleys and ridges are clearly seen in both the P10-patterned and MP-10 patterned membranes. In particular, in the MP-10-patterned membrane, additional nano-patterns are carved on the side prism surfaces.

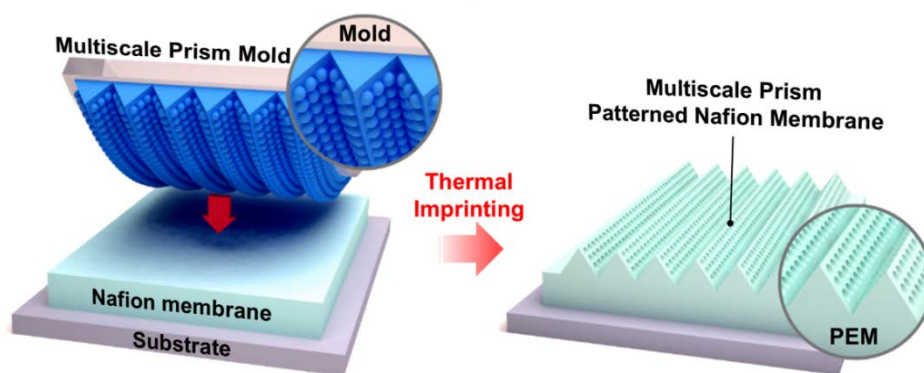
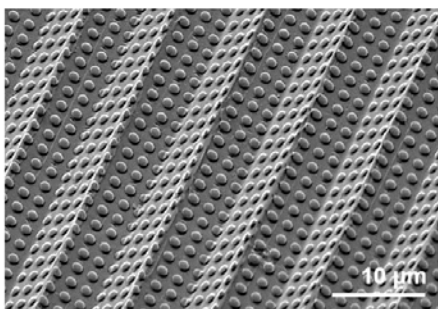


**Figure 4-1.** Schematic for the fabrication of the multiscala prism-patterned membrane by thermal imprinting.

**(a) Multi-scale Prism Mold**



**(b) Multi-scale Prism Mold**

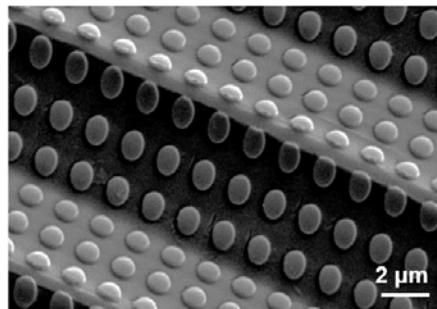


**Figure 4-2.** SEM images of the surface of the multiscale prism-patterned mold

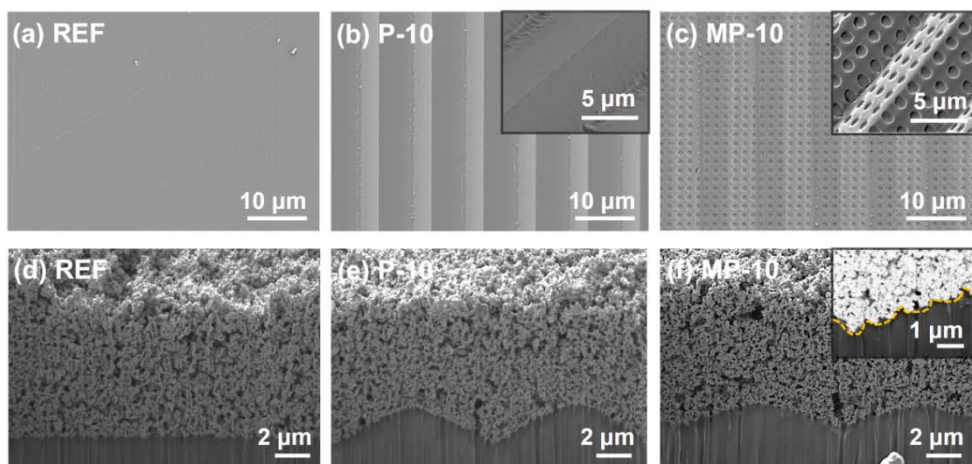


**Figure 4-3.** SEM images of the surfaces of the (a) flat reference, (b) prism-patterned (P-10), and (c) multiscale prism-patterned (MP-10) membranes; FIB-assisted cross-sectional SEM images of the anode catalyst layers of the prepared CCMs with a (d) flat surface, (e) prism pattern (P-10), and (f) multiscale prism pattern (MP-10).

### **4-3-2. Enhanced cell performance of direct methanol fuel cells with multiscale patterned membranes**

To evaluate the advantages of the multiscale patterned membrane in DMFCs, pristine, P-10-patterned, and MP-10-patterned membranes were incorporated into MEAs. The patterned side of the membranes was utilized for the anode catalyst layer to improve the reaction kinetics of methanol oxidation in the DMFCs. Commercial PtRu black (atomic ratio of Pt:Ru = 1:1) catalyst was spray-coated onto the patterned side of the membranes. To compare the morphological characteristics of the anode catalyst layers of the three different MEA samples, cross-sectional FIB-assisted SEM images (**Figure 4-3d-3f**) were obtained. The catalyst layers were well formed, conforming to the patterned membrane surface. Although the amount of loaded catalyst was the same in all cases, the average thickness varied for each anode catalyst layer:  $\sim 8.0\ \mu\text{m}$  for the reference MEA,  $\sim 7.2\ \mu\text{m}$  for the P-10 MEA, and  $\sim 6.9\ \mu\text{m}$  for the MP-10 MEA. The difference in the anode catalyst layer thickness arose from the enlarged surface area of the patterned membranes, as the catalyst layer thickness was inversely proportional to the surface area of each membrane. The increase in the real surface area was calculated based on the FIB-assisted SEM and AFM images. The surface areas of the P-10-patterned and MP-10-patterned membranes showed increases of  $\sim 15\%$  and  $27\%$ , respectively relative to that of the flat membrane (**Figure 4-4 and Figure 4-5**)

**Figure 4-6a-6b** shows single cell polarization curves for the MEAs

with pristine, P-10-patterned, and MP-10-patterned membranes when fed with methanol solutions with concentrations of 1.5 M and 3.0 M. Both the P-10 and MP-10 MEAs exhibited enhanced performance when compared with the reference MEA under all experimental conditions. The P-10 and MP-10 MEAs showed maximum power densities of 167 (128) mW cm<sup>-2</sup> and 177 (134) mW cm<sup>-2</sup>, respectively, in 1.5 (3.0) M methanol solution. The performance enhancement relative to the reference MEA was about 10.5% (15.3%) and 17.2% (20.7%) for the P-10 and MP-10 MEAs, respectively, in 1.5 (3.0) M methanol solution (**Table 4-1**). This enhanced performance would be ascribed to both the enlarged membrane–electrode interface contact area and the reduced catalyst layer thickness owing to the use of patterned membranes. The membrane–electrode interface generally contains the greatest number of active sites, where the electrochemical reaction occurs most effectively<sup>140</sup>. Moreover, a thinned anode catalyst layer facilitates mass transport of methanol, resulting in more methanol being easily accessible to the catalytic active sites<sup>137</sup>. Therefore, among the three different MEAs, the MP-10 MEA showed the highest single cell performance owing to the multiscale micro-/nanopatterned membrane. To investigate the effect of the patterned membrane on the overall resistance, EIS was conducted in methanol solutions with concentrations of 1.5 M and 3.0 M (**Figure 4-6c-6d**). The charge transfer resistance ( $R_{ct}$ ), which is affected by the electrochemical reaction in the DMFC, was calculated from

the diameter of the semicircle in the EIS spectra at the middle- and low-frequency ranges. A comparison of the  $R_{ct}$  values for the three MEAs with and without patterned membranes showed that the  $R_{ct}$  value decreased as the surface area of the membrane–electrode interface increased under both conditions (different methanol concentrations). Thus, the reduced  $R_{ct}$  was responsible for the improved performance of the multiscale patterned MEA.

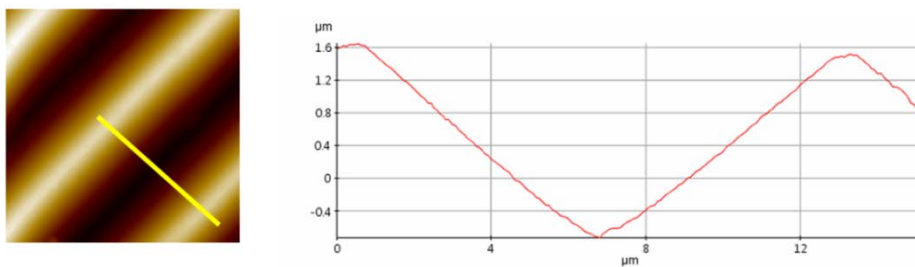
To investigate the enhanced cell performance of the patterned MEAs resulting from improved anode performance, anode polarization curves and EIS spectra were obtained for the three different MEAs using 3.0 M methanol solution utilizing the cathode with hydrogen instead of air as a DHE (**Figure 4-7**). The anodic overpotential of the three MEAs at the same current density followed the order: reference > P-10 > MP-10, which is the same trend as that observed for the single cell polarization curves. Moreover, the anode  $R_{ct}$ , which is affected by methanol oxidation at the anode, decreased as the surface area of the membrane–electrode interface increased. In addition, as shown in **Figure 4-8**, the single cell polarization curves of all the MEAs, including the reference MEA, MEAs with patterned membranes (P-10 and MP-10), and MEAs with patterned membranes containing a gold layer with guided cracks (P-10-Au and MP-10-Au), were almost identical when hydrogen was fed to the anode instead of methanol. This result indicates that all the cathodes in the MEAs had the same morphological features because the performance of the MEAs was mainly affected by the



oxygen reduction reaction at the cathode under hydrogen/oxygen operating conditions.

To investigate the effect of the enlarged membrane–electrode interface on the ECSA of the anode catalyst layer of the MEAs, CV was conducted (**Figure 4-9a**). To evaluate the catalytic properties of the anode catalyst layer, the hydrogen desorption peak was used to calculate the ECSA. As displayed in the magnified plots (**Figure 4-9b**), the intensity of the hydrogen desorption peak gradually increased with increasing membrane surface area. The ECSA of MP-10 MEA was calculated to be  $27.10 \text{ m}^2/\text{g}$ , which is  $\sim 4.3\%$  larger than that of the reference MEA ( $25.98 \text{ m}^2/\text{g}$ ), indicating that the MEA with the multiscale patterned membrane showed higher Pt utilization than the reference MEA. This enhancement resulted from the enlarged interfacial area between the membrane and the catalyst layer owing to the multiscale patterning<sup>41, 137-138</sup>. However, the increase in the ECSA (4.3%) was not sufficiently large to completely account for the enhanced performance (17.2%) of the MEA with the multiscale patterned membrane<sup>137, 141</sup>. Therefore, to better understand the origin of the performance enhancement, we should consider the comprehensive effects of the MEA with the multiscale patterned membrane, including enhanced mass transport and effective utilization of active sites.

**(a) AFM (P-10 patterned membrane)**



**(b) AFM (MP-10 Patterned membrane)**

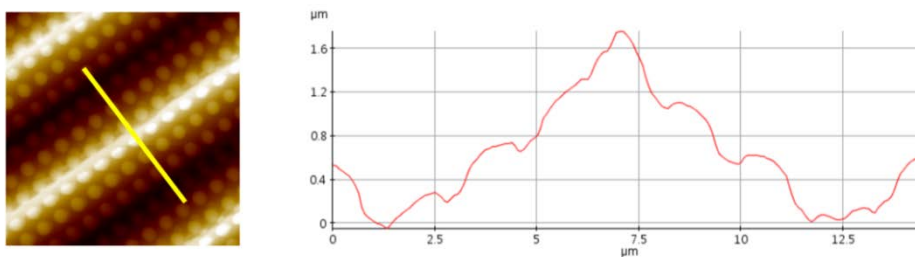


**Figure 4-4.** AFM images of the surface of the prism-patterned (P-10) and multiscale prism-patterned (MP-10) membranes.

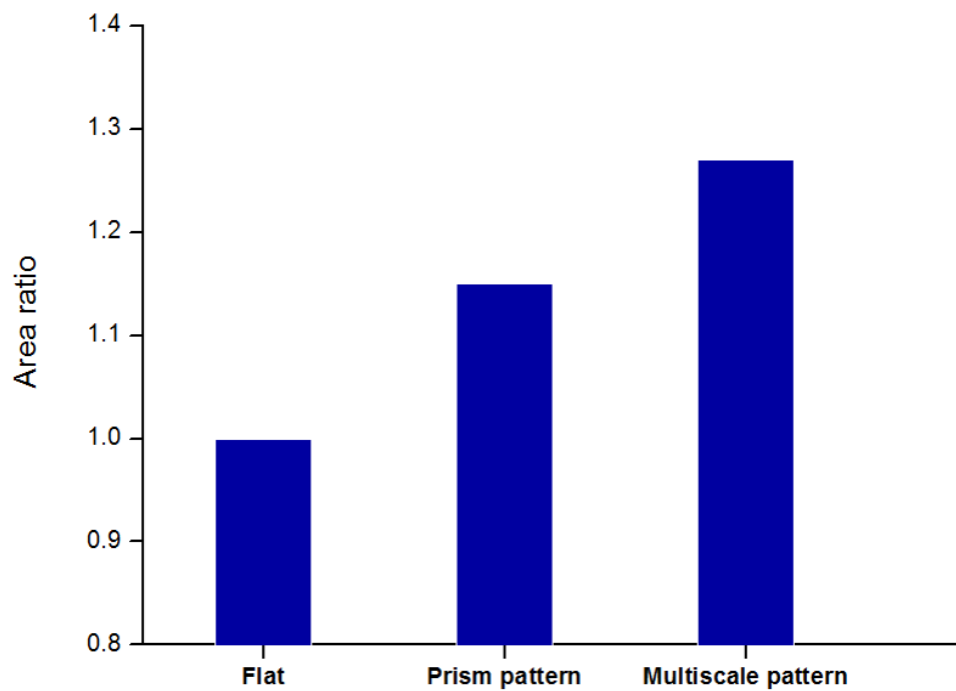


**Figure 4-5.** Relative membrane-electrode interface area of the flat reference, prism-patterned (P-10) and multiscale-patterned (MP-10) membrane.

MEA and methanol concentration	Open voltage [V]	circuit Current density at 0.4 V [A cm <sup>-2</sup> ]	Maximum density power [W cm <sup>-2</sup> ]
1.5 M methanol solution			
Reference	0.775	0.193	0.151 (+00.0%)
P-10	0.778	0.262	0.167 (+10.5%)
MP-10	0.796	0.298	0.177 (+17.2%)
P-10-Au	0.808	0.316	0.186 (+23.2%)
MP-10-Au	0.811	0.349	0.197 (+30.5%)
3.0 M methanol solution			
Reference	0.717	0.087	0.111 (+00.0%)
P-10	0.733	0.136	0.128 (+15.3%)
MP-10	0.736	0.158	0.134 (+20.7%)
P-10-Au	0.766	0.215	0.148 (+33.3%)
MP-10-Au	0.762	0.237	0.158 (+42.3%)

**Table 4-1.** Open circuit voltage, current density at 0.4 V, and maximum power density of prepared MEAs at two different methanol concentrations (1.5 M and 3.0 M)

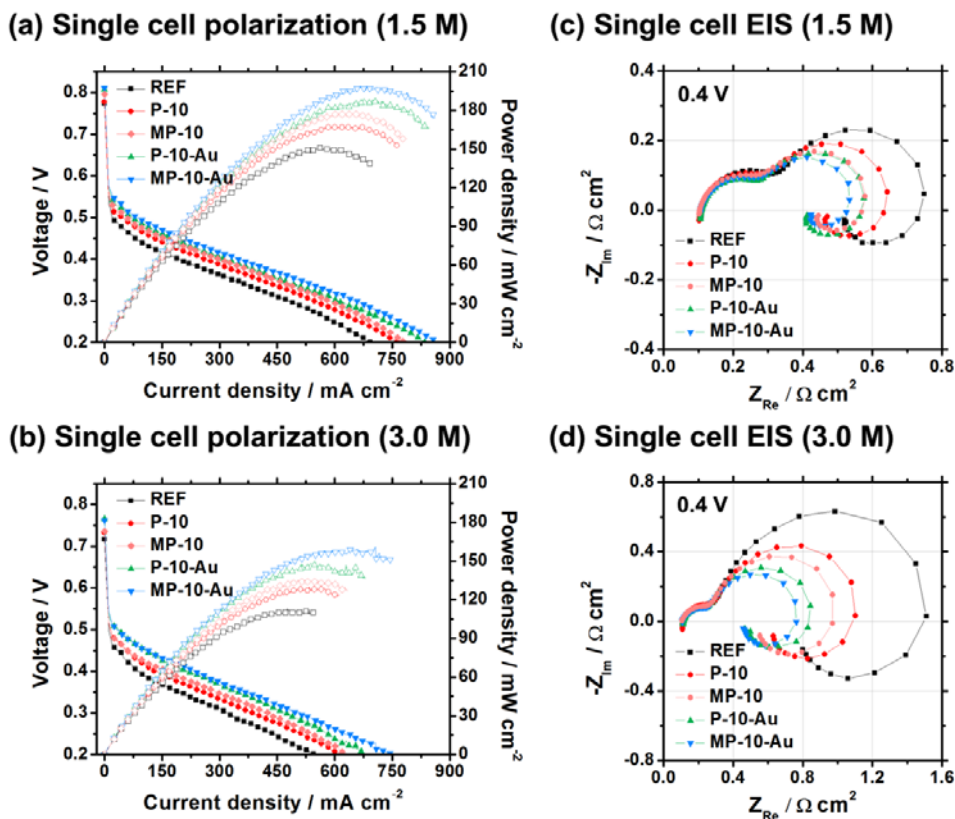
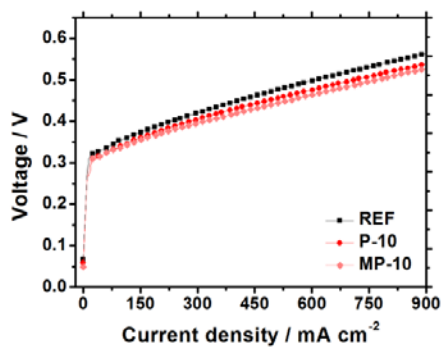


**Figure 4-6.** (a–b) Single cell polarization curves and (c–d) EIS spectra of the reference MEA, MEAs with patterned membranes (P-10 and MP-10), and MEAs with patterned membranes containing a Au layer with guided cracks (P-10-Au and MP-10-Au).

**(a) Anode polarization (3.0 M)**



**(b) Anode EIS (3.0 M)**

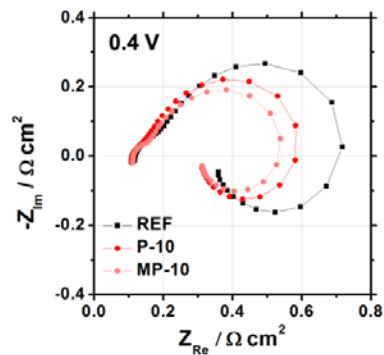


**Figure 4-7.** (a) Anode polarization curves and (b) anode EIS spectra of the reference MEA and MEAs with prism- (P-10) and multiscale prism-patterned (MP-10) membranes.

## Single cell polarization ( $\text{H}_2\text{-O}_2$ )

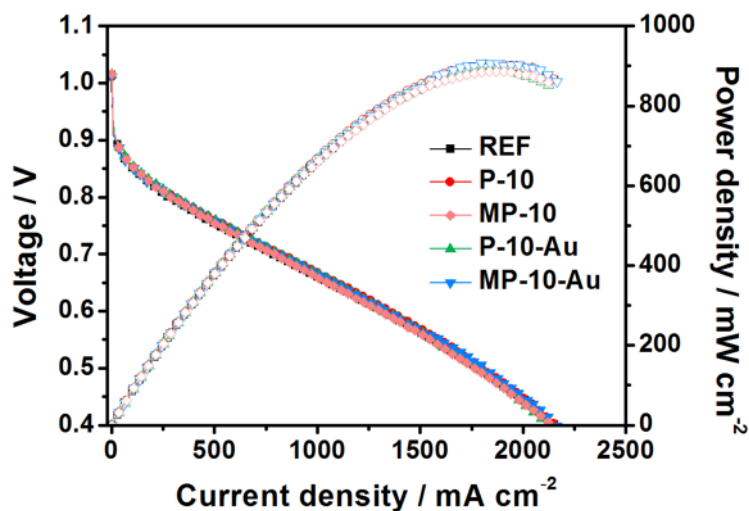


**Figure 4-8.** Single cell polarization curves under hydrogen-oxygen operation of all the MEAs including MEAs with patterned-membranes (P-10 and MP-10) and MEAs with patterned-membranes containing a Au layer with guided cracks (P-10-Au and MP-10-Au).

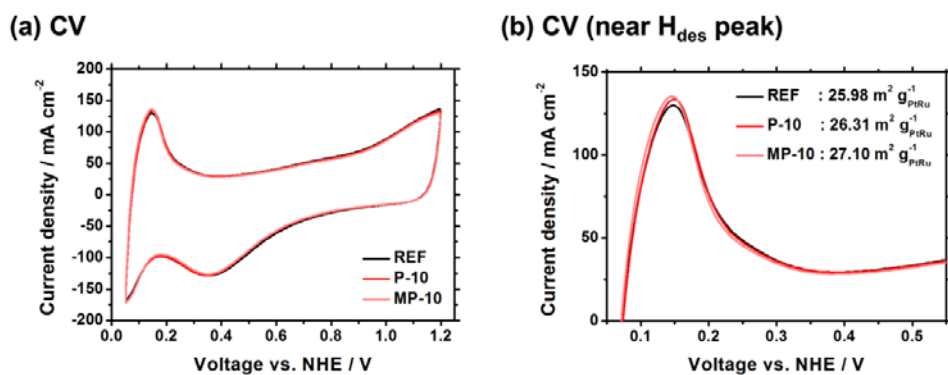


**Figure 4-9.** Cyclic voltammograms of the anode catalyst layers of the reference MEA and MEAs with prism- (P-10) and multiscale prism-patterned (MP-10) membranes.



### 4-3-3. Further enhanced cell performance with guided metal cracked barriers

To further enhance the performance of the DMFCs by reducing methanol crossover, a thin gold layer with guided cracks was incorporated into the multiscale patterned membrane. The methanol-inactive thin gold layer was expected to act as a physical barrier for methanol crossover and the cracks were expected to provide multiple proton pathways. **Figure 4-10a** shows a schematic illustration of the process for generating a gold layer with guided cracks on the multiscale patterned membrane. The thin gold layer (~40 nm) was deposited onto the patterned membrane surface (P-10 and MP-10) using a thermal evaporator. Then, the gold deposited patterned membrane was stretched with a strain of ~0.25 in the direction perpendicular to the prism pattern. After the stretching process, cracks were well formed, especially in the valleys of the prism pattern, owing to elastic modulus mismatch and confinement of the stresses in the valleys of the prism pattern<sup>142-144</sup>. **Figure 4-10b** shows the SEM images of the surface morphologies of the gold deposited patterned membranes with guided cracks (P-10-Au and MP-10-Au). The images show that the cracks are well controlled parallel to the prism direction in both cases, with widths-of under 100 nm. By using the stress-concentrated morphology of the patterned membrane, we can control and design the generation of cracks. These controllable cracks have several advantages over randomly formed cracks,

as (1) the same crack morphology can be reproduced easily, and (2) parametric studies on the effect of crack gap size and areal fraction of the cracks are possible. To confirm the effect of the gold layer with guided cracks on methanol permeation in the cathode, we measured the limiting current densities from the LSV curves for methanol oxidation at the cathode<sup>145</sup>. As seen in **Figure 4-11a-11b**, both the P-10-Au and MP-10-Au MEAs containing gold layers with guided cracks showed lower limiting current densities than the reference MEA and the patterned MEAs without the gold layers. The limiting current densities of the MEAs with the patterned membranes were slightly higher owing to the enlarged membrane–electrode interface and thinned anode catalyst layer<sup>132</sup>. These results show that while the MEAs with patterned membranes did not reduce the methanol crossover rate, the incorporation of gold layer with guided cracks has a critical effect on reducing methanol crossover.

The single cell polarization curves for the MEAs with guided gold cracked layers were also presented in **Figure 4-6a-6b**, when fed with 1.5 M and 3.0 M methanol solutions (**Table 4-1**). In the polarization curves, both P-10-Au and MP-10-Au MEAs with guided gold cracked layers exhibited significantly enhanced performance compared with the reference MEA and patterned MEAs without gold layers. The P-10-Au and MP-10-Au MEAs with guided gold cracked layers showed maximum power densities of 186 mW cm<sup>-2</sup> and 197 mW cm<sup>-2</sup>, respectively, in 1.5 M methanol solution,

denoting performance enhancements of about 23.2% and 30.5%, respectively, relative to that of the reference MEA. EIS measurements for the MEAs with guided metal cracks were conducted to figure out the effect of guided metal cracks (**Figure 4-6c-6d**). A comparison of the spectra for all the samples shows that the MEAs with guided gold cracked layers have much lower  $R_{ct}$  values than the reference MEA while maintaining a comparable ohmic resistance. The  $R_{ct}$  value of the MP-10-Au MEA is  $\sim 0.654 \Omega \text{ cm}^2$ , which is 2.1 times lower than that of the reference MEA ( $\sim 1.396 \Omega \text{ cm}^2$ ) in 3.0 M methanol. This finding implies that the effect of the guided metal cracked barrier is more prominent at higher methanol concentrations. Furthermore, CV experiments showed comparable ECSA values for the patterned MEAs with and without cracked gold layers (**Figure 4-12**), which meant that the incorporation of a cracked metal barrier into the MEAs does not affect Pt utilization and the number of available active sites. Therefore, further performance enhancement of the MEAs with a patterned membrane was successfully achieved by incorporating a gold layer with guided cracks, which can be attributed to two factors. First, the multiscale patterned membrane can significantly increase the interfacial area between the membrane and the catalyst layer. Therefore, in the MEA, we can effectively utilize the enlarged interfacial area, where electrochemical reactions are the most effective. Moreover, a thinned catalyst layer increases mass transport of the fuel, resulting in more methanol being easily

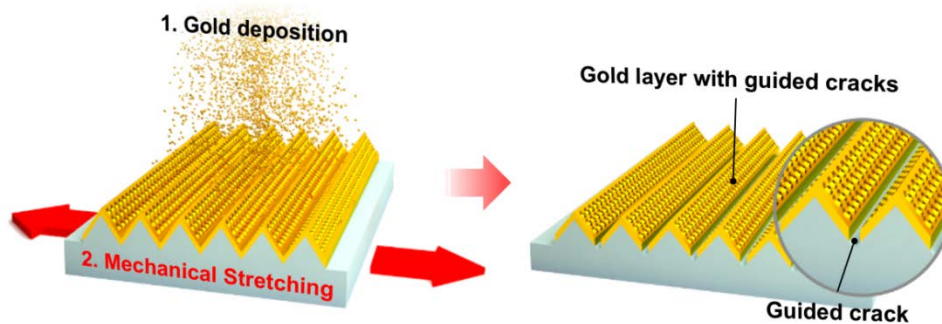
accessible to the catalytic active sites. Second, the gold layer with guided cracks plays a significant role in reducing the methanol crossover rate while maintaining a comparable proton transport ability because of the multiple cracks. Therefore, among the five different MEAs, the MP-10-Au MEA showed the highest cell performance owing to a synergistic effect between the enlarged membrane–electrode interface of the patterned membrane and the reduced methanol crossover rate of the gold layer with guided cracks. These effects are briefly summarized in **Figure 4-13**. Surprisingly, the device performance of the MP-10-Au MEA with a guided gold cracked layer was similar to that of the reference MEA operated in the presence of O<sub>2</sub> instead of air (**Figure 4-14**). Considering the thermodynamic potential of a DMFC, which can be calculated using the Nernst equation<sup>146</sup>,

$$V_{DMFC,thermo} = E_0 + \frac{RT}{6F} \ln \left\{ \frac{a_{CH_3OH} * (a_{O_2})^{1.5}}{a_{CO_2} * (a_{H_2O})^2} \right\}$$

where  $E_0$  is the standard potential,  $R$  is the gas constant,  $F$  is the Faraday's constant, and  $a_{CH_3OH}$ ,  $a_{O_2}$ ,  $a_{CO_2}$ , and  $a_{H_2O}$  are the chemical activity of methanol, oxygen, carbon dioxide, and water, respectively, the thermodynamic potential should be lower for the MP-10-Au MEA in air feeding conditions ( $a_{O_2} \sim 0.21$ ) than for the reference MEA in O<sub>2</sub> feeding conditions ( $a_{O_2} \sim 1$ ). Therefore, the comparable performances of the MP-10-Au MEA under air and the reference MEA under O<sub>2</sub> indicate that an

interface-engineered MEA with a multiscale patterned membrane and guided gold cracked layer can significantly improve DMFC performance. Furthermore, to confirm the effectiveness of a guided gold cracked layer in terms of proton conductivity and methanol crossover, single cell polarization curves and EIS spectra for randomly cracked gold layer ( $S \sim 0.25$ ) and non-cracked gold layer were measured. The MEA with non-cracked gold layer shows reduced performance about 41.1% and increased ohmic resistance about 70.2% than those of reference (**Figure 4-15**). This result indicates that the non-cracked gold layer works as a good methanol barrier, but it also prevents proton bonded with water molecules to permeate through the electrolyte membrane due to the absence of proton pathways. Interestingly, the MEA with the randomly cracked gold layer shows higher performance ( $164 \text{ mW cm}^{-2}$ ) than that of reference ( $151 \text{ mW cm}^{-2}$ ) but still exhibits lower performance and larger ohmic resistance than those of MEAs with guided gold layer. When same stress applied to the gold coated-flat membrane (strain  $\sim 0.25$ ), the stress was widely distributed on the surface of gold coated-flat membrane, and the cracks were not fully formed on the whole surface of the gold layer. However, in the case of the P-10-Au and MP-10-Au MEAs, the well-ordered cracks could be formed over the entire surface owing to the existence of the valleys of prism, where the stress could be concentrated. The difference is clearly confirmed by comparing the morphological surface features (**Figure 4-10b** and **Figure 4-16**)

**(a) Generation of thin Au layer with well-guided cracks**



**(b) SEM (Membrane surface)**

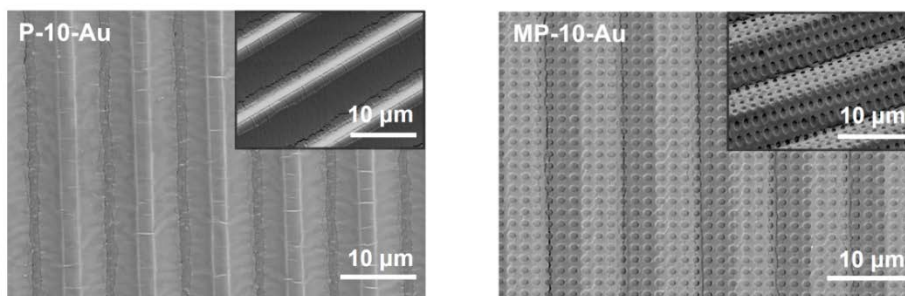
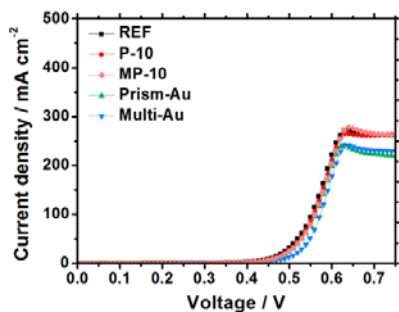


**Figure 4-10.** (a) Schematic for generating guided Au cracks by simple mechanical stretching (strain of  $\sim 0.25$ ) and (b) SEM images of the surfaces of prism-patterned (P-10-Au) and multiscale prism-patterned (MP-10-Au) membranes with guided Au cracks.

(a) LSV for MOR in cathode (1.5 M)



(b) LSV for MOR in cathode (3.0 M)

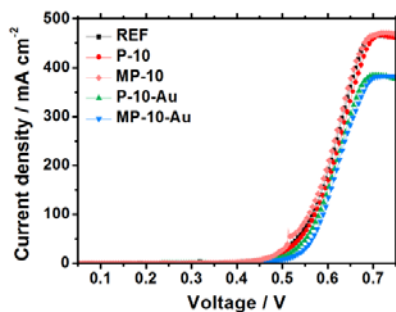


**Figure 4-11.** Limiting current density measurements for the reference MEA, MEAs with patterned membranes (P-10 and MP-10), and MEAs with patterned membranes and a guided Au cracked layer (P-10-Au and MP-10-Au).

### CV (near $H_{\text{des}}$ peak)

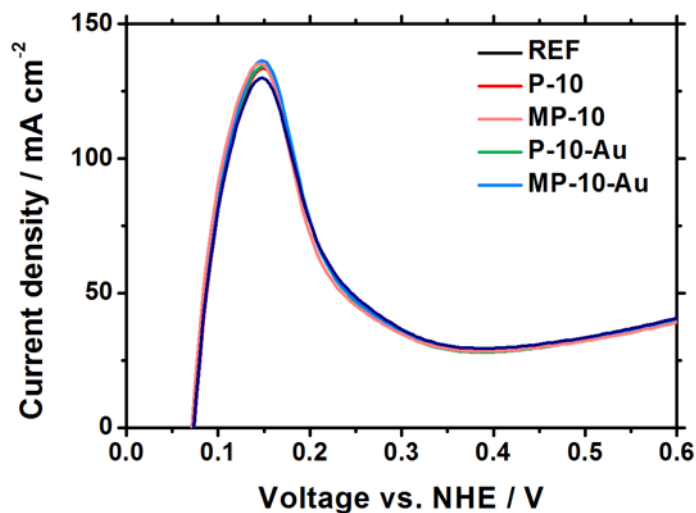


**Figure 4-12.** Cyclic voltammogram (CV) of the anode catalyst layers of all the MEAs including MEAs with patterned-membranes (P-10 and MP-10) and MEAs with patterned-membranes containing a Au layer with guided cracks (P-10-Au and MP-10-Au).



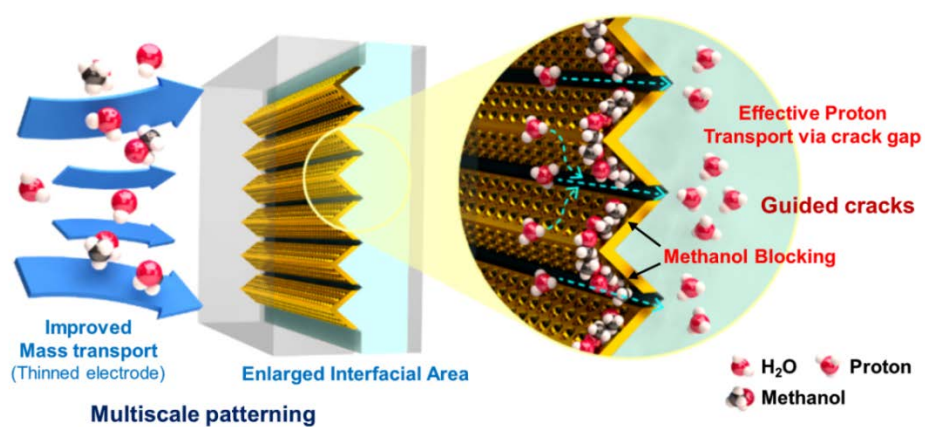


**Figure 4-13.** Schematic illustration of the effects of the enlarged interfacial area and the guided Au cracked barrier.

### Single cell Polarization (1.5 M)

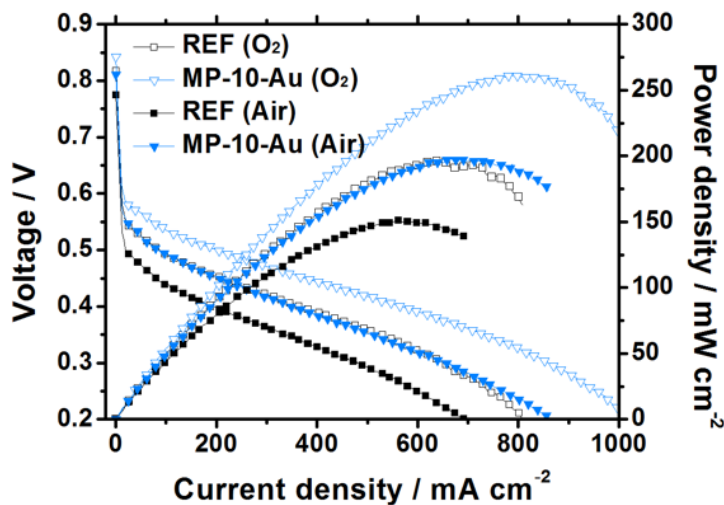
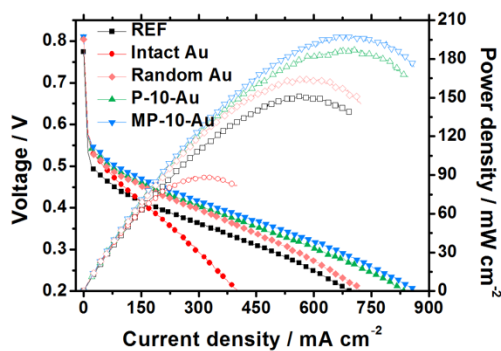


**Figure 4-14.** Single cell polarization curves under the 1.5 M methanol-oxygen (or air) operation of reference MEA and multiscale patterned MEA with Au layer with guided cracks (MP-10-Au). The flow rate of oxygen and air were identical ( $200 \text{ ml min}^{-1}$ ).

(a) Single cell polarization (1.5 M)



(b) Single cell EIS (1.5 M)

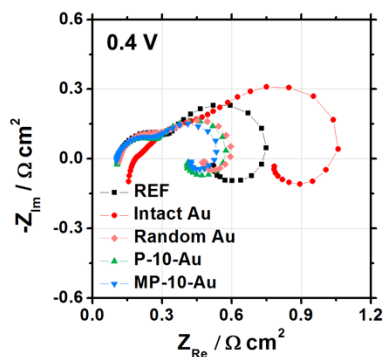
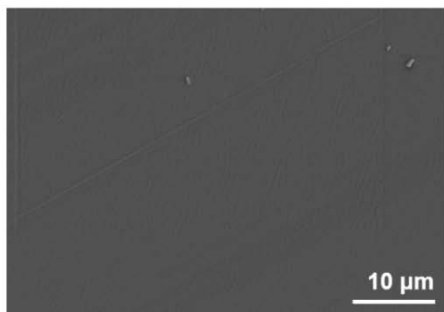


**Figure 4-15.** (a) Single cell polarization curves and (c) EIS spectra of the MEAs including reference MEA, MEA with intact Au layer (Intact Au), MEA with randomly cracked Au layer (Random Au) and MEAs with patterned membranes containing a Au layer with guided cracks (P-10-Au and MP-10-Au).

**(a) Intact Au**



**(b) Randomly Cracked Au**

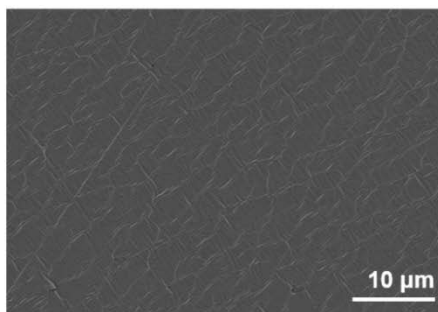


**Figure 4-16.** SEM images of the surfaces of the intact Au layer and randomly cracked Au layer on flat membrane.

#### **4-4. Summary**

We report herein a high-performance DMFC based on interface engineering between the membrane and the catalyst layer by using multiscale patterned membrane and guided metal cracked layer. The multiscale patterned membrane enhanced performance by improving mass transport, active site utilization, and Pt utilization. Based on this multiscale patterned membrane, we additionally incorporated a guided gold cracked layer. This guided thin gold cracked layer effectively reduced the methanol crossover rate while maintaining the proton transport ability owing to the existence of multiple cracks. The MEA with the multiscale patterned membrane and a guided gold cracked layer showed a performance improvement of over 30.5% relative to that of the reference MEA with a flat membrane. The effects of crack gap size and areal fraction of the cracks on reducing methanol crossover and maintaining proton conductivity are currently under investigation. We believe that the interface engineering reported in this study provides a practical and feasible route to fabricate high-performance fuel cells and holds a potential for application to other energy devices.

## References

1. Feng, L.; Li, S.; Li, Y.; Li, H.; Zhang, L.; Zhai, J.; Song, Y.; Liu, B.; Jiang, L.; Zhu, D., Super-hydrophobic surfaces: from natural to artificial. *Advanced materials* **2002**, *14* (24), 1857-1860.
2. Autumn, K.; Liang, Y. A.; Hsieh, S. T.; Zesch, W., Adhesive force of a single gecko foot-hair. *Nature* **2000**, *405* (6787), 681.
3. Gao, X.; Yan, X.; Yao, X.; Xu, L.; Zhang, K.; Zhang, J.; Yang, B.; Jiang, L., The dry-style antifogging properties of mosquito compound eyes and artificial analogues prepared by soft lithography. *Advanced Materials* **2007**, *19* (17), 2213-2217.
4. Zheng, Y.; Bai, H.; Huang, Z.; Tian, X.; Nie, F.-Q.; Zhao, Y.; Zhai, J.; Jiang, L., Directional water collection on wetted spider silk. *Nature* **2010**, *463* (7281), 640.
5. Chen, P.-Y.; Lin, A. Y.-M.; McKittrick, J.; Meyers, M. A., Structure and mechanical properties of crab exoskeletons. *Acta biomaterialia* **2008**, *4* (3), 587-596.
6. Bae, W. G.; Kim, H. N.; Kim, D.; Park, S. H.; Jeong, H. E.; Suh, K. Y., 25th anniversary article: scalable multiscale patterned structures inspired by nature: the role of hierarchy. *Advanced Materials* **2014**, *26* (5), 675-700.
7. Zhou, Y.; Tang, Y.; Zhu, J.; Deng, Q.; Yang, Y.; Zhao, L.; Hu, S., Characterization of micro structure through hybrid interference and phase determination in broadband light interferometry. *Applied Optics* **2017**, *56* (8), 2301-2306.
8. Sun, C.-C.; Tsai, S.-Y.; Lee, T.-X., Enhancement of angular flux utilization based on implanted micro pyramid array and lens encapsulation in GaN LEDs. *Journal of Display Technology* **2011**, *7* (5), 289-294.
9. Li, R.; Huang, Z., A new CHF model for enhanced pool boiling heat transfer on surfaces with micro-scale roughness. *International Journal of Heat and Mass Transfer* **2017**, *109*, 1084-1093.
10. Ferry, V. E.; Sweatlock, L. A.; Pacifici, D.; Atwater, H. A., Plasmonic nanostructure design for efficient light coupling into solar cells. *Nano letters* **2008**, *8* (12), 4391-4397.
11. Qian, F.; Li, Y.; Gradečák, S.; Park, H.-G.; Dong, Y.; Ding, Y.; Wang, Z. L.; Lieber, C. M., Multi-quantum-well nanowire heterostructures for wavelength-controlled lasers. *Nature materials* **2008**, *7* (9), 701-706.
12. Kang, S. M.; Jang, S.; Lee, J. K.; Yoon, J.; Yoo, D. E.; Lee, J. W.; Choi, M.; Park, N. G., Moth-Eye TiO<sub>2</sub> Layer for Improving Light Harvesting Efficiency in Perovskite Solar

Cells. *Small* **2016**, *12* (18), 2443-2449.

13. Jiang, S. P., Nanoscale and nano-structured electrodes of solid oxide fuel cells by infiltration: advances and challenges. *International journal of hydrogen energy* **2012**, *37* (1), 449-470.
14. Anta, J. A., Electron transport in nanostructured metal-oxide semiconductors. *Current opinion in colloid & interface science* **2012**, *17* (3), 124-131.
15. Brodoceanu, D.; Bauer, C.; Kroner, E.; Arzt, E.; Kraus, T., Hierarchical bioinspired adhesive surfaces—a review. *Bioinspiration & biomimetics* **2016**, *11* (5), 051001.
16. Chung, K.; Yu, S.; Heo, C. J.; Shim, J. W.; Yang, S. M.; Han, M. G.; Lee, H. S.; Jin, Y.; Lee, S. Y.; Park, N., Flexible, Angle-Independent, Structural Color Reflectors Inspired by Morpho Butterfly Wings. *Advanced Materials* **2012**, *24* (18), 2375-2379.
17. Yang, W.; Chen, I. H.; Gludovatz, B.; Zimmermann, E. A.; Ritchie, R. O.; Meyers, M. A., Natural flexible dermal armor. *Advanced Materials* **2013**, *25* (1), 31-48.
18. Joo, Y.; Byun, J.; Seong, N.; Ha, J.; Kim, H.; Kim, S.; Kim, T.; Im, H.; Kim, D.; Hong, Y., Silver nanowire-embedded PDMS with a multiscale structure for a highly sensitive and robust flexible pressure sensor. *Nanoscale* **2015**, *7* (14), 6208-6215.
19. Leem, Y. C.; Park, J. S.; Kim, J. H.; Myoung, N.; Yim, S. Y.; Jeong, S.; Lim, W.; Kim, S. T.; Park, S. J., Light-Emitting Diodes with Hierarchical and Multifunctional Surface Structures for High Light Extraction and an Antifouling Effect. *small* **2016**, *12* (2), 161-168.
20. Tamang, A.; Hongsingthong, A.; Sichanugrist, P.; Jovanov, V.; Konagai, M.; Knipp, D., Light-trapping and interface morphologies of amorphous silicon solar cells on multiscale surface textured substrates. *IEEE Journal of Photovoltaics* **2014**, *4* (1), 16-21.
21. Raut, H. K.; Dinachali, S. S.; Loke, Y. C.; Ganesan, R.; Ansah-Antwi, K. K.; Gora, A.; Khoo, E. H.; Ganesh, V. A.; Saifullah, M. S.; Ramakrishna, S., Multiscale ommatidial arrays with broadband and omnidirectional antireflection and antifogging properties by sacrificial layer mediated nanoimprinting. *ACS nano* **2015**, *9* (2), 1305-1314.
22. Greiner, C.; Arzt, E.; Del Campo, A., Hierarchical Gecko-Like Adhesives. *Advanced Materials* **2009**, *21* (4), 479-482.
23. Jeong, H. E.; Lee, J.-K.; Kim, H. N.; Moon, S. H.; Suh, K. Y., A nontransferring dry adhesive with hierarchical polymer nanohairs. *Proceedings of the National Academy of Sciences* **2009**, *106* (14), 5639-5644.
24. Ho, A. Y. Y.; Yeo, L. P.; Lam, Y. C.; Rodríguez, I., Fabrication and analysis of gecko-inspired hierarchical polymer nanosetae. *ACS nano* **2011**, *5* (3), 1897-1906.

25. Lewis, N. S.; Nocera, D. G., Powering the planet: Chemical challenges in solar energy utilization. *Proceedings of the National Academy of Sciences* **2006**, *103* (43), 15729-15735.
26. O'regan, B.; Grätzel, M., A low-cost, high-efficiency solar cell based on dye-sensitized colloidal TiO<sub>2</sub> films. *nature* **1991**, *353* (6346), 737-740.
27. Grätzel, M., Recent advances in sensitized mesoscopic solar cells. *Accounts of chemical research* **2009**, *42* (11), 1788-1798.
28. Kim, H.-S.; Lee, C.-R.; Im, J.-H.; Lee, K.-B.; Moehl, T.; Marchioro, A.; Moon, S.-J.; Humphry-Baker, R.; Yum, J.-H.; Moser, J. E., Lead iodide perovskite sensitized all-solid-state submicron thin film mesoscopic solar cell with efficiency exceeding 9%. *Scientific reports* **2012**, *2*.
29. Grätzel, M., Conversion of sunlight to electric power by nanocrystalline dye-sensitized solar cells. *Journal of Photochemistry and Photobiology A: Chemistry* **2004**, *164* (1), 3-14.
30. Jiang, W.; Liu, H.; Yin, L.; Ding, Y., Fabrication of well-arrayed plasmonic mesoporous TiO<sub>2</sub>/Ag films for dye-sensitized solar cells by multiple-step nanoimprint lithography. *Journal of Materials Chemistry A* **2013**, *1* (21), 6433-6440.
31. Lee, J.; Lee, M., Diffraction-grating-embedded dye-sensitized solar cells with good light harvesting. *Advanced Energy Materials* **2014**, *4* (4).
32. Na, J.; Kim, Y.; Park, C.; Kim, E., Multi-layering of a nanopatterned TiO<sub>2</sub> layer for highly efficient solid-state solar cells. *NPG Asia Materials* **2015**, *7*, e217.
33. Jang, S.; Kim, M.; Kang, Y. S.; Choi, Y. W.; Kim, S. M.; Sung, Y.-E.; Choi, M., Facile Multiscale Patterning by Creep-Assisted Sequential Imprinting and Fuel Cell Application. *ACS applied materials & interfaces* **2016**, *8* (18), 11459-11465.
34. Kim, S. M.; Kang, Y. S.; Ahn, C.; Jang, S.; Kim, M.; Sung, Y.-E.; Yoo, S. J.; Choi, M., Prism-patterned Nafion membrane for enhanced water transport in polymer electrolyte membrane fuel cell. *Journal of Power Sources* **2016**, *317*, 19-24.
35. Kim, S.; Jang, S.; Kim, S. M.; Ahn, C.-Y.; Hwang, W.; Cho, Y.-H.; Sung, Y.-E.; Choi, M., Reduction of methanol crossover by thin cracked metal barriers at the interface between membrane and electrode in direct methanol fuel cells. *Journal of Power Sources* **2017**, *363*, 153-160.
36. Houchins, C.; Kleen, G. J.; Spendelow, J. S.; Kopasz, J.; Peterson, D.; Garland, N. L.; Ho, D. L.; Marcinkoski, J.; Martin, K. E.; Tyler, R., US DOE progress towards developing low-cost, high performance, durable polymer electrolyte membranes for fuel cell applications. *Membranes* **2012**, *2* (4), 855-878.



37. Yen, C.-Y.; Lee, C.-H.; Lin, Y.-F.; Lin, H.-L.; Hsiao, Y.-H.; Liao, S.-H.; Chuang, C.-Y.; Ma, C.-C. M., Sol-gel derived sulfonated-silica/Nafion® composite membrane for direct methanol fuel cell. *Journal of power sources* **2007**, *173* (1), 36-44.
38. Jung, D.; Cho, S.; Peck, D.; Shin, D.; Kim, J., Preparation and performance of a Nafion®/montmorillonite nanocomposite membrane for direct methanol fuel cell. *Journal of Power Sources* **2003**, *118* (1), 205-211.
39. Casalegno, A.; Bresciani, F.; Di Noto, V.; Casari, C.; Bassi, A. L.; Negro, E.; Marchesi, R.; Di Fonzo, F., Nanostructured Pd barrier for low methanol crossover DMFC. *international journal of hydrogen energy* **2014**, *39* (6), 2801-2811.
40. Yoon, S.; Hwang, G.; Cho, W.; Oh, I.-H.; Hong, S.-A.; Ha, H., Modification of polymer electrolyte membranes for DMFCs using Pd films formed by sputtering. *Journal of Power Sources* **2002**, *106* (1), 215-223.
41. Jeon, Y.; Kim, D. J.; Koh, J. K.; Ji, Y.; Kim, J. H.; Shul, Y.-G., Interface-designed membranes with shape-controlled patterns for high-performance polymer electrolyte membrane fuel cells. *Scientific reports* **2015**, *5*, 16394.
42. Cho, H.; Kim, S. M.; Kang, Y. S.; Kim, J.; Jang, S.; Kim, M.; Park, H.; Bang, J. W.; Seo, S.; Suh, K.-Y., Multiplex lithography for multilevel multiscale architectures and its application to polymer electrolyte membrane fuel cell. *Nature communications* **2015**, *6*, 8484.
43. Lee, M.-S.; Chen, T.; Lee, W.; Lin, B.; Lau, B.; Tsai, P.; Wang, G., From microstructure to the development of water and major reaction sites inside the catalyst layer of the cathode of a proton exchange membrane fuel cell. *Journal of Power Sources* **2011**, *196* (18), 7411-7419.
44. Lewis, N. S., Research opportunities to advance solar energy utilization. *Science* **2016**, *351* (6271), aad1920.
45. Gratzel, M., Photoelectrochemical cells. *nature* **2001**, *414* (6861), 338.
46. Hagfeldt, A.; Boschloo, G.; Sun, L.; Kloo, L.; Pettersson, H., Dye-sensitized solar cells. *Chemical reviews* **2010**, *110* (11), 6595-6663.
47. Kakiage, K.; Aoyama, Y.; Yano, T.; Oya, K.; Fujisawa, J.-i.; Hanaya, M., Highly-efficient dye-sensitized solar cells with collaborative sensitization by silyl-anchor and carboxy-anchor dyes. *Chemical Communications* **2015**, *51* (88), 15894-15897.
48. Kojima, A.; Teshima, K.; Shirai, Y.; Miyasaka, T., Organometal halide perovskites as visible-light sensitizers for photovoltaic cells. *Journal of the American Chemical Society* **2009**, *131* (17), 6050-6051.
49. Lee, M. M.; Teuscher, J.; Miyasaka, T.; Murakami, T. N.; Snaith, H. J., Efficient

hybrid solar cells based on meso-superstructured organometal halide perovskites. *Science* **2012**, 338 (6107), 643-647.

50. Burschka, J.; Pellet, N.; Moon, S.-J.; Humphry-Baker, R.; Gao, P.; Nazeeruddin, M. K.; Grätzel, M., Sequential deposition as a route to high-performance perovskite-sensitized solar cells. *Nature* **2013**, 499 (7458), 316.

51. Li, X.; Dar, M. I.; Yi, C.; Luo, J.; Tschumi, M.; Zakeeruddin, S. M.; Nazeeruddin, M. K.; Han, H.; Grätzel, M., Improved performance and stability of perovskite solar cells by crystal crosslinking with alkylphosphonic acid  $\omega$ -ammonium chlorides. *Nature chemistry* **2015**, 7 (9), 703-711.

52. Yang, W. S.; Noh, J. H.; Jeon, N. J.; Kim, Y. C.; Ryu, S.; Seo, J.; Seok, S. I., High-performance photovoltaic perovskite layers fabricated through intramolecular exchange. *Science* **2015**, 348 (6240), 1234-1237.

53. Bach, U., Perovskite solar cells: Brighter pieces of the puzzle. *Nature chemistry* **2015**, 7 (8), 616-617.

54. Law, M.; Greene, L. E.; Johnson, J. C.; Saykally, R.; Yang, P., Nanowire dye-sensitized solar cells. *Nature materials* **2005**, 4 (6), 455-459.

55. Mor, G. K.; Shankar, K.; Paulose, M.; Varghese, O. K.; Grimes, C. A., Use of highly-ordered TiO<sub>2</sub> nanotube arrays in dye-sensitized solar cells. *Nano letters* **2006**, 6 (2), 215-218.

56. Zhu, K.; Neale, N. R.; Miedaner, A.; Frank, A. J., Enhanced charge-collection efficiencies and light scattering in dye-sensitized solar cells using oriented TiO<sub>2</sub> nanotubes arrays. *Nano letters* **2007**, 7 (1), 69-74.

57. Kang, S. H.; Choi, S. H.; Kang, M. S.; Kim, J. Y.; Kim, H. S.; Hyeon, T.; Sung, Y. E., Nanorod-based dye-sensitized solar cells with improved charge collection efficiency. *Advanced Materials* **2008**, 20 (1), 54-58.

58. Varghese, O. K.; Paulose, M.; Grimes, C. A., Long vertically aligned titania nanotubes on transparent conducting oxide for highly efficient solar cells. *Nature nanotechnology* **2009**, 4 (9), 592-597.

59. Kim, H.-S.; Lee, J.-W.; Yantara, N.; Boix, P. P.; Kulkarni, S. A.; Mhaisalkar, S.; Grätzel, M.; Park, N.-G., High efficiency solid-state sensitized solar cell-based on submicrometer rutile TiO<sub>2</sub> nanorod and CH<sub>3</sub>NH<sub>3</sub>PbI<sub>3</sub> perovskite sensitizer. *Nano letters* **2013**, 13 (6), 2412-2417.

60. So, S.; Hwang, I.; Schmuki, P., Hierarchical DSSC structures based on “single walled” TiO<sub>2</sub> nanotube arrays reach a back-side illumination solar light conversion efficiency of 8%. *Energy & Environmental Science* **2015**, 8 (3), 849-854.

61. Im, J.-H.; Luo, J.; Franckevičius, M.; Pellet, N.; Gao, P.; Moehl, T.; Zakeeruddin, S. M.; Nazeeruddin, M. K.; Grätzel, M.; Park, N.-G., Nanowire perovskite solar cell. *Nano letters* **2015**, *15* (3), 2120-2126.
62. Zhang, Q.; Myers, D.; Lan, J.; Jenekhe, S. A.; Cao, G., Applications of light scattering in dye-sensitized solar cells. *Physical Chemistry Chemical Physics* **2012**, *14* (43), 14982-14998.
63. Deepak, T.; Anjusree, G.; Thomas, S.; Arun, T.; Nair, S. V.; Nair, A. S., A review on materials for light scattering in dye-sensitized solar cells. *RSC Advances* **2014**, *4* (34), 17615-17638.
64. Usami, A., Theoretical study of application of multiple scattering of light to a dye-sensitized nanocrystalline photoelectrochemical cell. *Chemical Physics Letters* **1997**, *277* (1-3), 105-108.
65. Wang, Z.-S.; Kawauchi, H.; Kashima, T.; Arakawa, H., Significant influence of TiO<sub>2</sub> photoelectrode morphology on the energy conversion efficiency of N719 dye-sensitized solar cell. *Coordination chemistry reviews* **2004**, *248* (13), 1381-1389.
66. Koo, H. J.; Kim, Y. J.; Lee, Y. H.; Lee, W. I.; Kim, K.; Park, N. G., Nano-embossed hollow spherical TiO<sub>2</sub> as bifunctional material for high-efficiency dye-sensitized solar cells. *Advanced Materials* **2008**, *20* (1), 195-199.
67. Kim, J.; Lee, H.; Kim, D. Y.; Seo, Y., Resonant Multiple Light Scattering for Enhanced Photon Harvesting in Dye-Sensitized Solar Cells. *Advanced Materials* **2014**, *26* (30), 5192-5197.
68. Halaoui, L. I.; Abrams, N. M.; Mallouk, T. E., Increasing the conversion efficiency of dye-sensitized TiO<sub>2</sub> photoelectrochemical cells by coupling to photonic crystals. *The Journal of Physical Chemistry B* **2005**, *109* (13), 6334-6342.
69. Colodrero, S.; Mihi, A.; Häggman, L.; Ocaña, M.; Boschloo, G.; Hagfeldt, A.; Míguez, H., Porous One-Dimensional Photonic Crystals Improve the Power-Conversion Efficiency of Dye-Sensitized Solar Cells. *Advanced Materials* **2009**, *21* (7), 764-770.
70. Guldin, S.; Huttner, S.; Kolle, M.; Welland, M. E.; Muller-Buschbaum, P.; Friend, R. H.; Steiner, U.; Tétreault, N., Dye-sensitized solar cell based on a three-dimensional photonic crystal. *Nano letters* **2010**, *10* (7), 2303-2309.
71. Mihi, A.; Zhang, C.; Braun, P. V., Transfer of Preformed Three-Dimensional Photonic Crystals onto Dye-Sensitized Solar Cells. *Angewandte Chemie* **2011**, *123* (25), 5830-5833.
72. Seo, Y. G.; Woo, K.; Kim, J.; Lee, H.; Lee, W., Rapid fabrication of an inverse opal TiO<sub>2</sub> photoelectrode for DSSC using a binary mixture of TiO<sub>2</sub> nanoparticles and

polymer microspheres. *Advanced Functional Materials* **2011**, *21* (16), 3094-3103.

73. Zhang, W.; Anaya, M.; Lozano, G.; Calvo, M. E.; Johnston, M. B.; Míguez, H. n.; Snaith, H. J., Highly efficient perovskite solar cells with tunable structural color. *Nano letters* **2015**, *15* (3), 1698-1702.

74. Hägglund, C.; Zäch, M.; Kasemo, B., Enhanced charge carrier generation in dye sensitized solar cells by nanoparticle plasmons. *Applied Physics Letters* **2008**, *92* (1), 013113.

75. Brown, M. D.; Suteewong, T.; Kumar, R. S. S.; D'Innocenzo, V.; Petrozza, A.; Lee, M. M.; Wiesner, U.; Snaith, H. J., Plasmonic dye-sensitized solar cells using core-shell metal-insulator nanoparticles. *Nano letters* **2010**, *11* (2), 438-445.

76. Ding, I.; Zhu, J.; Cai, W.; Moon, S. J.; Cai, N.; Wang, P.; Zakeeruddin, S. M.; Grätzel, M.; Brongersma, M. L.; Cui, Y., Plasmonic dye-sensitized solar cells. *Advanced Energy Materials* **2011**, *1* (1), 52-57.

77. Choi, H.; Chen, W. T.; Kamat, P. V., Know thy nano neighbor. Plasmonic versus electron charging effects of metal nanoparticles in dye-sensitized solar cells. *ACS nano* **2012**, *6* (5), 4418-4427.

78. Choi, J.-W.; Kang, H.; Lee, M.; Kang, J. S.; Kyeong, S.; Yang, J.-K.; Kim, J.; Jeong, D. H.; Lee, Y.-S.; Sung, Y.-E., Plasmon-enhanced dye-sensitized solar cells using SiO<sub>2</sub> spheres decorated with tightly assembled silver nanoparticles. *RSC Advances* **2014**, *4* (38), 19851-19855.

79. Kim, J.; Koh, J. K.; Kim, B.; Kim, J. H.; Kim, E., Nanopatterning of Mesoporous Inorganic Oxide Films for Efficient Light Harvesting of Dye-Sensitized Solar Cells. *Angewandte Chemie* **2012**, *124* (28), 6970-6975.

80. Wooh, S.; Yoon, H.; Jung, J. H.; Lee, Y. G.; Koh, J. H.; Lee, B.; Kang, Y. S.; Char, K., Efficient Light Harvesting with Micropatterned 3D Pyramidal Photoanodes in Dye-Sensitized Solar Cells. *Advanced Materials* **2013**, *25* (22), 3111-3116.

81. Ok, M.-R.; Ghosh, R.; Brennaman, M. K.; Lopez, R.; Meyer, T. J.; Samulski, E. T., Surface patterning of mesoporous niobium oxide films for solar energy conversion. *ACS applied materials & interfaces* **2013**, *5* (8), 3469-3474.

82. Heo, S. Y.; Koh, J. K.; Kang, G.; Ahn, S. H.; Chi, W. S.; Kim, K.; Kim, J. H., Bifunctional Moth-Eye Nanopatterned Dye-Sensitized Solar Cells: Light-Harvesting and Self-Cleaning Effects. *Advanced Energy Materials* **2014**, *4* (3).

83. López-López, C.; Colodrero, S.; Jiménez-Solano, A.; Lozano, G.; Ortiz, R.; Calvo, M. E.; Míguez, H., Multidirectional light-harvesting enhancement in dye solar cells by surface patterning. *Advanced Optical Materials* **2014**, *2* (9), 879-884.

84. Zhang, X.; Liu, H.; Huang, X.; Jiang, H., One-step femtosecond laser patterning of light-trapping structure on dye-sensitized solar cell photoelectrodes. *Journal of Materials Chemistry C* **2015**, *3* (14), 3336-3341.
85. Choi, S.-J.; Yoo, P. J.; Baek, S. J.; Kim, T. W.; Lee, H. H., An ultraviolet-curable mold for sub-100-nm lithography. *Journal of the American Chemical Society* **2004**, *126* (25), 7744-7745.
86. Kim, Y.; Suh, K.; Lee, H. H., Fabrication of three-dimensional microstructures by soft molding. *Applied Physics Letters* **2001**, *79* (14), 2285-2287.
87. Na, S.-I.; Kim, S.-S.; Kwon, S.-S.; Jo, J.; Kim, J.; Lee, T.; Kim, D.-Y., Surface relief gratings on poly (3-hexylthiophene) and fullerene blends for efficient organic solar cells. *Applied Physics Letters* **2007**, *91* (17), 173509.
88. Na, S. I.; Kim, S. S.; Jo, J.; Oh, S. H.; Kim, J.; Kim, D. Y., Efficient polymer solar cells with surface relief gratings fabricated by simple soft lithography. *Advanced Functional Materials* **2008**, *18* (24), 3956-3963.
89. Zhu, J.; Hsu, C.-M.; Yu, Z.; Fan, S.; Cui, Y., Nanodome solar cells with efficient light management and self-cleaning. *Nano letters* **2009**, *10* (6), 1979-1984.
90. Xie, C.; Zhang, X.; Ruan, K.; Shao, Z.; Dhaliwal, S. S.; Wang, L.; Zhang, Q.; Zhang, X.; Jie, J., High-efficiency, air stable graphene/Si micro-hole array Schottky junction solar cells. *Journal of Materials Chemistry A* **2013**, *1* (48), 15348-15354.
91. Tan, H.; Psomadaki, E.; Isabella, O.; Fischer, M.; Babal, P.; Vasudevan, R.; Zeman, M.; Smets, A. H., Micro-textures for efficient light trapping and improved electrical performance in thin-film nanocrystalline silicon solar cells. *Applied Physics Letters* **2013**, *103* (17), 173905.
92. Sommeling, P.; O'regan, B.; Haswell, R.; Smit, H.; Bakker, N.; Smits, J.; Kroon, J.; Van Roosmalen, J., Influence of a TiCl<sub>4</sub> post-treatment on nanocrystalline TiO<sub>2</sub> films in dye-sensitized solar cells. *The Journal of Physical Chemistry B* **2006**, *110* (39), 19191-19197.
93. O'Regan, B. C.; Durrant, J. R.; Sommeling, P. M.; Bakker, N. J., Influence of the TiCl<sub>4</sub> treatment on nanocrystalline TiO<sub>2</sub> films in dye-sensitized solar cells. 2. Charge density, band edge shifts, and quantification of recombination losses at short circuit. *The Journal of Physical Chemistry C* **2007**, *111* (37), 14001-14010.
94. Merkel, T.; Bondar, V.; Nagai, K.; Freeman, B.; Pinnau, I., Gas sorption, diffusion, and permeation in poly (dimethylsiloxane). *Journal of Polymer Science Part B: Polymer Physics* **2000**, *38* (3), 415-434.
95. Decker, C.; Viet, T. N. T.; Decker, D.; Weber-Koehl, E., UV-radiation curing of

acrylate/epoxide systems. *Polymer* **2001**, *42* (13), 5531-5541.

96. Cho, H.; Kim, J.; Park, H.; Bang, J. W.; Hyun, M. S.; Bae, Y.; Ha, L.; Kang, S. M.; Park, T. J.; Seo, S., Replication of flexible polymer membranes with geometry-controllable nano-apertures via a hierarchical mould-based dewetting. *Nature communications* **2014**, *5*, 3137.

97. Díaz-Parralejo, A.; Caruso, R.; Ortiz, A.; Guiberteau, F., Densification and porosity evaluation of ZrO<sub>2</sub>-3 mol.% Y<sub>2</sub>O<sub>3</sub> sol-gel thin films. *Thin Solid Films* **2004**, *458* (1), 92-97.

98. Han, J.; Craighead, H. G., Separation of long DNA molecules in a microfabricated entropic trap array. *Science* **2000**, *288* (5468), 1026-1029.

99. Cho, H.; Kim, J.; Suga, K.; Ishigami, T.; Park, H.; Bang, J. W.; Seo, S.; Choi, M.; Chang, P.-S.; Umakoshi, H., Microfluidic platforms with monolithically integrated hierarchical apertures for the facile and rapid formation of cargo-carrying vesicles. *Lab on a Chip* **2015**, *15* (2), 373-377.

100. Retterer, S. T.; Siuti, P.; Choi, C.-K.; Thomas, D. K.; Doktycz, M. J., Development and fabrication of nanoporous silicon-based bioreactors within a microfluidic chip. *Lab on a Chip* **2010**, *10* (9), 1174-1181.

101. Jeong, H. E.; Lee, S. H.; Kim, J. K.; Suh, K. Y., Nanoengineered multiscale hierarchical structures with tailored wetting properties. *Langmuir* **2006**, *22* (4), 1640-1645.

102. Gopinath, A.; Boriskina, S. V.; Premasiri, W. R.; Ziegler, L.; Reinhard, B. r. M.; Dal Negro, L., Plasmonic nanogalaxies: multiscale aperiodic arrays for surface-enhanced Raman sensing. *Nano letters* **2009**, *9* (11), 3922-3929.

103. Kim, J. B.; Kim, P.; Pégard, N. C.; Oh, S. J.; Kagan, C. R.; Fleischer, J. W.; Stone, H. A.; Loo, Y.-L., Wrinkles and deep folds as photonic structures in photovoltaics. *Nature Photonics* **2012**, *6* (5), 327-332.

104. Shallcross, R. C.; Chawla, G. S.; Marikkar, F. S.; Tolbert, S.; Pyun, J.; Armstrong, N. R., Efficient CdSe nanocrystal diffraction gratings prepared by microcontact molding. *ACS nano* **2009**, *3* (11), 3629-3637.

105. Yoo, S.; Kim, J.-H.; Shin, M.; Park, H.; Kim, J.-H.; Lee, S.-Y.; Park, S., Hierarchical multiscale hyperporous block copolymer membranes via tunable dual-phase separation. *Science advances* **2015**, *1* (6), e1500101.

106. Zhang, F.; Chan, J.; Low, H. Y., Biomimetic, hierarchical structures on polymer surfaces by sequential imprinting. *Applied Surface Science* **2008**, *254* (10), 2975-2979.

107. del Campo, A.; Arzt, E., Fabrication approaches for generating complex micro- and nanopatterns on polymeric surfaces. *Chemical reviews* **2008**, *108* (3), 911-945.

108. Alavijeh, A. S.; Khorasany, R. M.; Habisch, A.; Wang, G. G.; Kjeang, E., Creep properties of catalyst coated membranes for polymer electrolyte fuel cells. *Journal of Power Sources* **2015**, 285, 16-28.
109. Chou, S. Y.; Krauss, P. R.; Renstrom, P. J., Imprint lithography with 25-nanometer resolution. *Science* **1996**, 272 (5258), 85.
110. Zhang, H.; Shen, P. K., Advances in the high performance polymer electrolyte membranes for fuel cells. *Chemical Society Reviews* **2012**, 41 (6), 2382-2394.
111. Jung, N.; Kim, S. M.; Kang, D. H.; Chung, D. Y.; Kang, Y. S.; Chung, Y.-H.; Choi, Y. W.; Pang, C.; Suh, K.-Y.; Sung, Y.-E., High-performance hybrid catalyst with selectively functionalized carbon by temperature-directed switchable polymer. *Chemistry of Materials* **2013**, 25 (9), 1526-1532.
112. O'hayre, R.; Cha, S.-W.; Prinz, F. B.; Colella, W., *Fuel cell fundamentals*. John Wiley & Sons: 2016.
113. Cho, Y.-H.; Jung, N.; Kang, Y. S.; Chung, D. Y.; Lim, J. W.; Choe, H.; Cho, Y.-H.; Sung, Y.-E., Improved mass transfer using a pore former in cathode catalyst layer in the direct methanol fuel cell. *international journal of hydrogen energy* **2012**, 37 (16), 11969-11974.
114. Costamagna, P.; Srinivasan, S., Quantum jumps in the PEMFC science and technology from the 1960s to the year 2000: Part II. Engineering, technology development and application aspects. *Journal of power sources* **2001**, 102 (1), 253-269.
115. Jung, N.; Chung, D. Y.; Ryu, J.; Yoo, S. J.; Sung, Y.-E., Pt-based nanoarchitecture and catalyst design for fuel cell applications. *Nano Today* **2014**, 9 (4), 433-456.
116. Pang, C.; Kim, T. i.; Bae, W. G.; Kang, D.; Kim, S. M.; Suh, K. Y., Bioinspired Reversible Interlocker Using Regularly Arrayed High Aspect-Ratio Polymer Fibers. *Advanced Materials* **2012**, 24 (4), 475-479.
117. Lee, C.; Kim, S. M.; Kim, Y. J.; Choi, Y. W.; Suh, K.-Y.; Pang, C.; Choi, M., Robust microzip fastener: repeatable interlocking using polymeric rectangular parallelepiped arrays. *ACS applied materials & interfaces* **2015**, 7 (4), 2561-2568.
118. Choi, S.-J.; Kim, H. N.; Bae, W. G.; Suh, K.-Y., Modulus-and surface energy-tunable ultraviolet-curable polyurethane acrylate: properties and applications. *Journal of Materials Chemistry* **2011**, 21 (38), 14325-14335.
119. Perez-Alonso, F. J.; McCarthy, D. N.; Nierhoff, A.; Hernandez-Fernandez, P.; Strebel, C.; Stephens, I. E.; Nielsen, J. H.; Chorkendorff, I., The Effect of Size on the Oxygen Electroreduction Activity of Mass-Selected Platinum Nanoparticles. *Angewandte Chemie International Edition* **2012**, 51 (19), 4641-4643.

120. Alia, S. M.; Zhang, G.; Kisailus, D.; Li, D.; Gu, S.; Jensen, K.; Yan, Y., Porous platinum nanotubes for oxygen reduction and methanol oxidation reactions. *Advanced Functional Materials* **2010**, *20* (21), 3742-3746.
121. Kim, O.-H.; Cho, Y.-H.; Kang, S. H.; Park, H.-Y.; Kim, M.; Lim, J. W.; Chung, D. Y.; Lee, M. J.; Choe, H.; Sung, Y.-E., Ordered macroporous platinum electrode and enhanced mass transfer in fuel cells using inverse opal structure. *Nature communications* **2013**, *4*, 2473.
122. Prasanna, M.; Ha, H.; Cho, E.; Hong, S.-A.; Oh, I.-H., Investigation of oxygen gain in polymer electrolyte membrane fuel cells. *Journal of power sources* **2004**, *137* (1), 1-8.
123. Yuan, X.; Wang, H.; Sun, J. C.; Zhang, J., AC impedance technique in PEM fuel cell diagnosis—A review. *International Journal of Hydrogen Energy* **2007**, *32* (17), 4365-4380.
124. Walker, G. M.; Beebe, D. J., A passive pumping method for microfluidic devices. *Lab on a Chip* **2002**, *2* (3), 131-134.
125. Prakash, M.; Quéré, D.; Bush, J. W., Surface tension transport of prey by feeding shorebirds: the capillary ratchet. *science* **2008**, *320* (5878), 931-934.
126. Gouws, S., Voltammetric Characterization Methods for the PEM Evaluation of Catalysts. In *Electrolysis*, InTech: 2012.
127. Pozio, A.; De Francesco, M.; Cemmi, A.; Cardellini, F.; Giorgi, L., Comparison of high surface Pt/C catalysts by cyclic voltammetry. *Journal of power sources* **2002**, *105* (1), 13-19.
128. Kamarudin, S. K.; Achmad, F.; Daud, W. R. W., Overview on the application of direct methanol fuel cell (DMFC) for portable electronic devices. *International Journal of hydrogen energy* **2009**, *34* (16), 6902-6916.
129. Zhao, T.; Xu, C.; Chen, R.; Yang, W., Mass transport phenomena in direct methanol fuel cells. *Progress in energy and Combustion Science* **2009**, *35* (3), 275-292.
130. Tiwari, J. N.; Tiwari, R. N.; Singh, G.; Kim, K. S., Recent progress in the development of anode and cathode catalysts for direct methanol fuel cells. *Nano Energy* **2013**, *2* (5), 553-578.
131. Xie, J.; Zhang, Q.; Gu, L.; Xu, S.; Wang, P.; Liu, J.; Ding, Y.; Yao, Y. F.; Nan, C.; Zhao, M., Ruthenium-platinum core-shell nanocatalysts with substantially enhanced activity and durability towards methanol oxidation. *Nano Energy* **2016**, *21*, 247-257.
132. Kim, H.-T.; Reshentenko, T. V.; Kweon, H.-J., Microstructured membrane electrode assembly for direct methanol fuel cell. *Journal of The Electrochemical Society*



**2007**, 154 (10), B1034-B1040.

133. Omosebi, A.; Besser, R. S., Electron beam patterned Nafion membranes for DMFC applications. *Journal of Power Sources* **2013**, 228, 151-158.

134. Sebastian, D.; Serov, A.; Matanovic, I.; Artyushkova, K.; Atanassov, P.; Arico, A.; Baglio, V., Insights on the extraordinary tolerance to alcohols of Fe-NC cathode catalysts in highly performing direct alcohol fuel cells. *Nano Energy* **2017**, 34, 195-204.

135. Ahmed, M.; Dincer, I., A review on methanol crossover in direct methanol fuel cells: challenges and achievements. *International Journal of Energy Research* **2011**, 35 (14), 1213-1228.

136. Wu, S.; Liu, J.; Liang, D.; Sun, H.; Ye, Y.; Tian, Z.; Liang, C., Photo-excited in situ loading of Pt clusters onto rGO immobilized SnO<sub>2</sub> with excellent catalytic performance toward methanol oxidation. *Nano Energy* **2016**, 26, 699-707.

137. Pu, L.; Jiang, J.; Yuan, T.; Chai, J.; Zhang, H.; Zou, Z.; Li, X.-M.; Yang, H., Performance improvement of passive direct methanol fuel cells with surface-patterned Nafion® membranes. *Applied Surface Science* **2015**, 327, 205-212.

138. Cho, Y.-H.; Bae, J. W.; Kim, O.-H.; Jho, J. Y.; Jung, N.; Shin, K.; Choi, H.; Choe, H.; Cho, Y.-H.; Sung, Y.-E., High performance direct methanol fuel cells with micro/nano-patterned polymer electrolyte membrane. *Journal of Membrane Science* **2014**, 467, 36-40.

139. Müller, J. T.; Urban, P. M.; Hölderich, W. F., Impedance studies on direct methanol fuel cell anodes. *Journal of Power Sources* **1999**, 84 (2), 157-160.

140. Aizawa, M.; Gyoten, H.; Salah, A.; Liu, X., Pillar structured membranes for suppressing cathodic concentration overvoltage in PEMFCs at elevated temperature/low relative humidity. *Journal of The Electrochemical Society* **2010**, 157 (12), B1844-B1851.

141. Bae, J. W.; Cho, Y.-H.; Sung, Y.-E.; Shin, K.; Jho, J. Y., Performance enhancement of polymer electrolyte membrane fuel cell by employing line-patterned Nafion membrane. *Journal of Industrial and Engineering Chemistry* **2012**, 18 (3), 876-879.

142. Kang, D.; Pikhitsa, P. V.; Choi, Y. W.; Lee, C.; Shin, S. S.; Piao, L.; Park, B.; Suh, K.-Y.; Kim, T.-i.; Choi, M., Ultrasensitive mechanical crack-based sensor inspired by the spider sensory system. *Nature* **2014**, 516 (7530), 222-226.

143. Kim, S. M.; Ahn, C.-Y.; Cho, Y.-H.; Kim, S.; Hwang, W.; Jang, S.; Shin, S.; Lee, G.; Sung, Y.-E.; Choi, M., High-performance Fuel Cell with Stretched Catalyst-Coated Membrane: One-step Formation of Cracked Electrode. *Scientific reports* **2016**, 6, 26503.

144. Kim, B. C.; Matsuoka, T.; Moraes, C.; Huang, J.; Thouless, M.; Takayama, S., Guided fracture of films on soft substrates to create micro/nano-feature arrays with controlled periodicity. *Scientific reports* **2013**, 3.

145. Prabhuram, J.; Zhao, T.; Yang, H., Methanol adsorbates on the DMFC cathode and their effect on the cell performance. *Journal of electroanalytical chemistry* **2005**, 578 (1), 105-112.
146. Mann, R. F.; Amphlett, J. C.; Hooper, M. A.; Jensen, H. M.; Peppley, B. A.; Roberge, P. R., Development and application of a generalised steady-state electrochemical model for a PEM fuel cell. *Journal of power sources* **2000**, 86 (1), 173-180.

## 국 문 초 록

본 학위 논문에서는 산소에 의한 자외선 경화 고분자의 부분경화 현상 및 점탄성 특성을 나타내는 고분자 물질의 크리프 거동을 이용하여 다차원, 다층 구조물을 제작하기 위한 새롭고 용이한 공정을 제시하고 있다. 또한, 이렇게 제작된 다차원, 다층 구조물을 염료감응형 태양전지에 적용하여, 마이크로/나노 구조물의 광학적 특성이 증첩된 효과를 구현하였으며, 고분자 전해질 막 연료전지와 직접 메탄올 연료전지 시스템에 적용하여 성능을 향상시킨 결과를 제시하였다.

먼저, 멀티플렉스 리소그래피를 사용하여 LEGO<sup>®</sup>와 유사한 다차원, 다층 구조물 ( $z$  축 방향으로 통합) 제작 방법과 이를 이용한 효율적인 광자 수집에 대한 새로운 전략을 소개하였다. 산소에 의한 광중합 지연효과를 기반으로 한 멀티플렉스 리소그래피를 이용하여, 나노 또는 마이크로 관통홀을 가지고 있는 폴리우레탄 아크릴레이트(PUA) 막을 적층하고, 추가로 나노패턴을 형성하였다. 하부와 상부 표면 사이의 PUA 막의 경화 정도가 다름에 따라, 부분적으로 경화된 PUA 막의 바닥면은 접착층으로 사용되었고, 상대적으로 경화정도가 더 낮은 상부표면은 추가적인 나노 패터닝을 위해 사용되었다. 그 다음으로, 앞서 적층된 막으로부터 PDMS 를 이용하여 형상을 복제하였고, PDMS 몰드를 이용하여 다차원, 다층구조를 지닌  $\text{TiO}_2$  층을 제작하였다. 다양한 스펙트럼 분석 및 시뮬레이션을 통해, 다차원, 다층구조를 지닌  $\text{TiO}_2$  층에서 나노 및 마이크로 구조물의 광학적 효과가 증첩되어 나타난다는 사실을 검증하였다.

우리는 다차원, 다층구조를 이용한 광수집 효과의 유효성을 확인하기 위해, 염료 감응형 태양 전지에 이를 적용하였고 최대 17.5%의 효율증가(다차원, 다층 400nm 라인 / 20 $\mu$ m 도트 구조에 의한)를 관찰하였다. 마지막으로, 측정된 외부 양자 효율은 나노 구조 및 마이크로 구조에 의해 유도된 회절 격자 및 무작위 산란의 결합 효과로부터 향상된 광수집 효과를 명확하게 보여주었다.

다음으로, 우리는 쉽고 간단한 다차원 패터닝 방법인 크리프 거동을 이용한 순차 임프린팅 방법을 제안하였고, 이를 고분자 전해질 막 연료전지에 적용하였다. 점탄성 폴리머(예)Nafion<sup>®</sup>의 크리프 거동을 기반으로 우리는 먼저 폴리머 필름의 유리 전이 온도 ( $T_g$ )보다 높은 온도에서 열 임프린트 기법을 사용하여 나노 패터닝을 수행 하였다. 다음으로,  $T_g$  미만의 온도에서 기계적 응력을 비교적 장기간 가했을 때, 영구적 변형이 생기는 폴리머의 크리프 특성을 이용하여, 마이크로 구조를 한번 더 임프린트 하였다. 제작된 다차원 구조물들은 넓은 영역 (> 3.5cm x 3.5cm)에서 우수한 패턴 균일 성을 보였고, 먼저 형성된 나노 패턴의 경우, 마이크로 패터닝 이후에도 전 영역에 걸쳐 (마이크로 구조물의 측면에도) 남아 있는 것을 확인할 수 있었다. 크리프 거동 기반의 다차원 패터닝 방법의 효용성을 검증하기 위해, 다차원 구조물이 새겨진 Nafion<sup>®</sup> 전해질 막을 고분자 전해질 막 연료전지에 적용하였고, 기존 시스템보다 10% 이상의 성능 향상을 관찰하였다. 성능향상의 이유로는 첫째, 크리프 회복에 의한 고유한 원뿔형상의 구조는 생성된 물방울의 상단부와 하단부 사이에 라플라스 압력 차를 발생시키고, 이로 인한 향상된 물 제거 효과는 시스템의 물질 전달 저항의 감소효과를 가져오게

되었다. 둘째로는, 표면 거칠기가 큰 다차원 패턴의 막의 사용은 Nafion<sup>®</sup> 막과 전기 촉매 층 사이의 계면 표면적을 확대시키고, 이는 전기 화학적 표면적 및 Pt 활용도를 증가 시키게 되었다.

마지막으로, 직접메탄올 연료전지의 성능향상을 위해, 전해질 막과 촉매층 사이의 계면을 새롭게 디자인하는 방법을 제시하였다. 직접메탄올 연료전지에서 성능 손실은 크게 애노드에서의 느린 메탄올 산화반응 속도와 메탄올의 전해질 막 투과로 인한 캐소드에서의 혼성전위 형성에서 나타난다. 우리는 크리프거동 기반의 순차 임프린팅 방법과 간단한 연신 기술을 이용하여, 다차원 구조가 형성된 전해질 막을 제작하였고 촉매층과 전해질 막 사이에 잘 정렬된 크랙을 지닌 금속박막을 삽입하였다. 다차원 구조물을 지닌 막의 사용은 얇아진 전극층에 의한 물질 전달의 향상과 전기화학적 활성이 높은 지역의 효과적인 활용 및 향상된 Pt 활용도를 가져왔다. 또한, 잘 정렬된 크랙을 지니고 전기화학적으로 안정한 금 박막의 삽입은 메탄올 투과에 대한 물리적 장벽으로 작용했으며, 유도 된 크랙은 양성자의 이동에 있어서 다중 경로를 제공하였다. 결과적으로, 직접메탄올 연료전지의 전해질막과 촉매층사이의 계면을 다차원적으로 디자인함으로써, 기존 시스템 대비 42.3 % 이상의 성능향상을 이루었다.

**주요어:** 멀티스케일 패터닝; 광수집; 크리프 거동; 크랙; 메탄올 투과; 연료전지

**학번:** 2013-22499